

Horizon 2020

Space Call - Earth Observation: EO-3-2016: Evolution of Copernicus services

Grant Agreement No. 730008

ECoLaSS

Evolution of Copernicus Land Services based on Sentinel data



D6.1

"D31.1 - Methods Compendium: Sentinel-1/2/3 Integration Strategies"

Issue/Rev.: 1.0

Date Issued: 23.03.2018

submitted by:



in collaboration with the consortium partners:



submitted to:



European Commission – Research Executive Agency

This project has received funding from the European Union's Horizon 2020 Research and Innovation Programme, under Grant Agreement No. 730008.

CONSORTIUM PARTNERS

No.	PARTICIPANT ORGANISATION NAME	SHORT NAME	CITY, COUNTRY
1	GAF AG	GAF	Munich, Germany
2	Systèmes d'Information à Référence Spatiale SAS	SIRS	Villeneuve d'Ascq, France
3	JOANNEUM RESEARCH Forschungsgesellschaft mbH	JR	Graz, Austria
4	Université catholique de Louvain, Earth and Life Institute (ELI)	UCL	Louvain-la-Neuve, Belgium
5	German Aerospace Center (DLR), German Remote Sensing Data Center (DFD), Wessling	DLR	Wessling, Germany

CONTACT:

GAF AG
Arnulfstr. 199 – D-80634 München – Germany
Phone: ++49 (0)89 121528 0 – FAX: ++49 (0)89 121528 79
E-mail: copernicus@gaf.de – Internet: www.gaf.de

DISCLAIMER:

The contents of this document are the copyright of GAF AG and Partners. It is released by GAF AG on the condition that it will not be copied in whole, in section or otherwise reproduced (whether by photographic, reprographic or any other method) and that the contents thereof shall not be divulged to any other person other than of the addressed (save to the other authorised officers of their organisation having a need to know such contents, for the purpose of which disclosure is made by GAF AG) without prior consent of GAF AG and Partners.

DOCUMENT RELEASE SHEET

	NAME, FUNCTION	DATE	SIGNATURE
Author(s):	Annekatrin Metz-Marconcini (DLR) Igor Klein (DLR) Soner Üreyen (DLR) Inès Moreau (UCL) Sophie Villerot (SIRS) Grégory Jacquet (SIRS)	09.03.2018	<i>A. Metz-Marconcini</i>
Review:	Annekatrin Metz-Marconcini (DLR) Baudouin Desclee (SIRS) Katharina Schwab (GAF)	22.03.2018	<i>A. Metz-Marconcini</i>
Approval:	Linda Moser (GAF)	23.03.2018	<i>Linda Moser</i>
Acceptance:	Massimo Ciscato (REA)		
Distribution:	Public		

DISSEMINATION LEVEL

DISSEMINATION LEVEL		
PU	Public	X
CO	Confidential: only for members of the consortium (including the Commission Services)	

DOCUMENT STATUS SHEET

ISSUE/REV	DATE	PAGE(S)	DESCRIPTION / CHANGES
1.0	22.03.2018	71	First issue of the Methods Compendium: Sentinel-1/2/3 Integration Strategies

EXECUTIVE SUMMARY

The Horizon 2020 (H2020) project, “Evolution of Copernicus Land Services based on Sentinel data” (ECoLaSS) addresses the H2020 Work Programme 5 iii. Leadership in Enabling and Industrial technologies - Space, specifically the Topic EO-3-2016: Evolution of Copernicus services. ECoLaSS will be conducted from 2017–2019 and aims at developing and prototypically demonstrating selected innovative products and methods for future next-generation operational Copernicus Land Monitoring Service (CLMS) products of the pan-European and Global Components. This will contribute to demonstrating operational readiness of the finally selected products, and shall allow the key CLMS stakeholders (i.e. mainly the Entrusted European Entities (EEE) EEA and JRC) to take informed decisions on potential procurement of the next generation of Copernicus Land services from 2020 onwards. To achieve this goal, ECoLaSS will make full use of dense time series of Sentinel-2 and Sentinel-3 optical data as well as Sentinel-1 Synthetic Aperture Radar (SAR) data. Rapidly evolving scientific as well as user requirements will be analysed in support of a future pan-European roll-out of new/improved CLMS products, and the transfer to global applications.

This report constitutes a methods compendium of the investigated Sentinel-1/-2/-3 (S-1/-2/-3) integration strategies aiming at developing and testing integration strategies for S-1, S-2 and S-3 data to allow benefitting from their complementary multi-resolution, multi-temporal and multi-sensor characteristics. The objective of WP 31 is to investigate the possibilities of combining S-1, S-2 and S-3 data with regards to the envisaged evolution of Copernicus Land Services addressed in ECoLaSS. Within this WP, a feasibility analysis for a better characterisation of the HRLs by means of two types of integration/fusion strategies will be pursued: the integration of S-1 and S-2 data as well as the fusion of S-2 and S-3 data. With the combination of S-1 and S-2 data, the integration of complementary information is established, resulting from different physical interactions with the land surface, describing primarily different characteristics of the Land Cover/Land Use objects. With a fusion/integration of time series data from S-2 and S-3 corresponding sets of spectral bands are analysed, sensible for the same biophysical properties with nine overlapping spectral bands in the visible and NIR spectral regions of both sensors, but lower spatial resolution (S-3). The additional data-takes and denser time series derived from S-3 offer high potential generating a fusion product of both satellite sensors using interpolation methods.

The ECoLaSS project follows a two-phased approach of two times 18 months duration. This deliverable comprises the first issue, which primarily focused on identifying suitable approaches for the integration of S-1/-2/-3. Therefore, current state-of-the-art methods have been investigated to define fusion approaches integrating data with different spectral and/or spatial resolutions from two or more sensors in order to exploit both their high spectral and temporal resolution properties and to target the challenges of missing data in a time series. Furthermore, candidate approaches for a fusion/integration of S-1/S-2 and S-2/S-3 have been identified and benchmarked. Preliminary results are presented. In the second 18-month project cycle, a second issue of this deliverable will be published, containing all relevant updates concerning the benchmarking of S-1/S-2 as well as S-2/S-3 integration and fusion methods with support of the outcomes of WP33, WP34, and WP35.

Table of Contents

1	INTRODUCTION	1
1.1	PURPOSE AND OBJECTIVES.....	1
1.2	OUTLINE.....	2
2	REMOTE SENSING FOR LC/LU ANALYSIS.....	3
2.1	OPTICAL TIME SERIES DATA AND ITS LIMITATIONS.....	3
2.2	RADAR TIME SERIES DATA AND ITS LIMITATIONS.....	3
2.3	ADVANTAGES OF INTEGRATION OF OPTICAL AND SAR IMAGERY	4
2.4	ADVANTAGES OF SPATIAL - TEMPORAL FUSION OF OPTICAL IMAGERY	4
3	STATE-OF-THE ART.....	5
3.1	PRE-PROCESSING STEPS ENABLING COMPLEMENTARY INFORMATION INTEGRATION AND FUSION.....	6
3.2	INTEGRATION OF S-1/S-2 COMPLEMENTARY INFORMATION.....	6
3.2.1	SAR data as alternative input to close gap from optical imagery.....	6
3.2.2	SAR data as complementary information to S-2	7
3.2.3	Preliminary conclusions.....	12
3.3	INTEGRATION OF S-2/S-3 (FUSION)	12
3.3.1	Spectral, spatial, temporal interpolation and/or fusion approaches	12
3.3.2	Spectral and textural time series metrics/variables	19
3.4	CANDIDATE INTERPOLATION AND FUSION APPROACHES FOR BENCHMARKING	37
3.4.1	Candidate approaches for integration of S-1/S-2 complementary information	37
3.4.2	Candidate approaches for spectral, spatial, temporal interpolation and/or fusion approaches	37
3.4.3	Candidate approaches for spectral time series metrics/variables	38
4	TESTING AND BENCHMARKING OF CANDIDATE METHODS.....	41
4.1	DESCRIPTION OF CANDIDATE METHODS.....	41
4.1.1	Candidate approaches for integration of S-1/S-2 complementary information	41
4.1.2	Candidate approaches for spectral, spatial, temporal interpolation and/or fusion approaches	42
4.1.3	Candidate approaches for spectral time series metrics/variables	43

4.2	TESTING CRITERIA.....	45
4.3	IMPLEMENTATION OF TESTING	47
4.3.1	Candidate approaches for integration of S-1/S-2 complementary information	47
4.3.2	Candidate approaches for spectral, spatial, temporal interpolation and/or fusion approaches	51
4.3.3	Candidate approaches for spectral and textural time series metrics/variables.....	51
5	CONCLUSIONS AND OUTLOOK.....	62
6	REFERENCES	64

List of Figures

Figure 4-1: S-2 Mean RGB for 2017 for area West of Toulouse.....	48
Figure 4-2: S-1 VV Desc Mean for Area West of Toulouse.....	48
Figure 4-3: S-2 false colour composite of bands R: NIR MEAN, G: RED MEAN and B: GREEN MEAN for Mean of 2017 for area West of Toulouse.....	49
Figure 4-4: S-2 false colour composite of R: NDBI MEAN, G: NDVI MEAN and B: MNDWI MEAN for 2017 for area West of Toulouse.....	49
Figure 4-5: False colour composite of bands R: S-1 VV MEAN, G: S-2 MNDWI MEAN and B: S-2 NDBI MEAN for Mean of 2017 for area West of Toulouse.....	50
Figure 4-6: False colour composite of bands R: S-1 VV MEAN, G: S-2 NDMIR MEAN and B: S-2 NDBI MEAN for Mean of 2017 for area West of Toulouse.....	50
Figure 4-7: Computed maximal NDVI values per pixel: the dark green zones indicate the presence of vegetation, while lighter zones characterize urban areas and water bodies.	52
Figure 4-8: Computed NDVI median over 19 images for the year 2016, on the whole 31UFS tile. Negative values (minimum at -1) are represented in white and positive values (maximum at +1) in dark green....	52
Figure 4-9: Computed minimal NDVI values per pixel: the lowest values highlight the presence of water bodies and urban areas.	53
Figure 4-10: Computed standard deviation NDVI values per pixel: the highest values indicate areas where the NDVI varies the most – here, where vegetation is the densest.....	53
Figure 4-11: Computed maximal NDBI values per pixel: the black (positive values near +1) values delineate the water bodies with high suspended matter that reflects MIR wavelengths stronger than the NIR.	54
Figure 4-12: Computed median NDBI values per pixel: the highest values (in dark grey) are found over urban areas as expected.....	54
Figure 4-13: Computed minimal NDBI values per pixel: the highest values (in dark grey) over urban areas are even more highlighted than with the maximal values.....	55
Figure 4-14: Computed standard deviation NDBI values per pixel: areas where the NDBI varies the most are vegetated, as expected due to the seasonality.....	55
Figure 4-16: Computed median values for the green band (4) per pixel: the blackest values indicate the least reflective zones, while the yellowest are the brightest, as seen in this band.....	56
Figure 4-15: Computed median values for the red band (3) per pixel: the blackest values indicate the least reflective zones, while the yellowest are the brightest, as seen in this band.....	56
Figure 4-17: Computed median values for the narrow red edge band (7) per pixel: the blackest values indicate the least reflective zones, while the yellowest are the brightest, as seen in this band.....	57

Figure 4-18: Computed median values for the wide red edge band (8) per pixel: the blackest values indicate the least reflective zones, while the yellowest are the brightest, as seen in this band..... 57

Figure 4-19: Computed median values for the first SWIR band (11) per pixel: the blackest values indicate the least reflective zones, while the yellowest are the brightest, as seen in this band..... 58

List of Tables

Table 3-1: List of spectral indices and their use for the creation of time series	20
Table 3-2: List of textural indices and their use in the creation of time series.....	32
Table 3-3: List of potential candidate indices for the creation of time series.....	39
Table 4-1: List of proposed spectral indices (source: Esch et al. (2018)).	41
Table 4-2: Euclidian distance of LC discrimination using NDBI statistical signatures.....	58
Table 4-3: Jeffries-Matusita distance of LC discrimination using NDBI statistical signatures.....	59
Table 4-4: Euclidian distance of LC discrimination using NDVI statistical signatures.	59
Table 4-5: Jeffries-Matusita distance of LC discrimination using NDVI statistical signatures.....	59
Table 4-6: Euclidian distance of LC discrimination using NDBI/NDVI statistical signatures.....	60
Table 4-7: Jeffries-Matusita distance of LC discrimination using NDBI/NDVI statistical signatures.	60
Table 4-8: Euclidian distance of LC discrimination using bands 3-4-8-7-11 statistical signatures.	60
Table 4-9: Jeffries-Matusita distance of LC discrimination using bands 3-4-8-7-11 statistical signatures. 60	

Abbreviations

2D	Two dimension
AOI	Area Of Interest
ANN	Artificial Neural Network
ARVI	Atmospherically Resistant Vegetation Index
ATPRK	Area-to-point Regression Kriging
AVIRIS	Airborne Visible Infrared Imaging Spectrometer
AVNIR-2	Advanced Visible and Near Infrared Radiometer type 2
BAP	Best-available pixel
BASI	Built-up Areas Saliency Index
BDF	Bayesian Data Fusion
BOA	Bottom of Atmosphere
BRDF	bidirectional reflectance distribution functions
BT	Bovery Transform
BUI	Built-Up Index
CART	Classification And Regression Tree
CLC	CORINE Land Cover
CS	Component Substitution
DEM	Digital Elevation Model
DFA	Discriminant Function Analysis
DIC	digital image correlation
DSM	Digital Soil Mapping
DST	Dempster-Shafer Theory
DTW	Dynamic Time Warping
DVI	Difference Vegetation Index
DWH	Data WareHouse
EAP	Extended Attribute Profile
EBBI	Enhanced Built-Up and Barenness Index
ERS	European Remote-Sensing Satellite
ESTARFM	Enhanced Spatial and Temporal Adaptive Reflectance Fusion Model
EVI	Enhanced Vegetation Index <i>OR</i> Environment Vegetation Index
fAPAR	Fraction of Absorbed Photosynthetically Active Radiation
FCover	Fractional Cover
FLAASH	Fast Line-of-Sight Atmospheric Analysis of Spectral Hypercubes
FOTO	FOurier-based Textural Ordination
FT	Fourier Transform
GEMI	Global Environment Monitoring Index
GLCM	Gray-Level Co-occurrence Matrix
GLCH	Gray-Level Co-occurrence Histogram
GLDV	Grey-Level Difference Vector
HDRF	hemispherical directional reflectance factor
HH	Horizontal transmit/Horizontal receive (polarization)
HIS	Intensity Hue Saturation
HLAC	Higher-order local autocorrelation
HLS	Harmonized Landsat-Sentinel-2
HRL	High Resolution Layer
HV	Horizontal transmit/Vertical receive (polarization)
IBI	Index-based Built-Up Index
IHS	Intensity–Hue–Saturation

LAI	Leaf Area Index
LC	Land Cover
LC/LU	Land Cover/Land Use
LCLUC	Land Cover/Land Use Change
LU	Land Use
MACCS	Multi-sensor Atmospheric Correction and Cloud Screening prototype
MBA	Modulation-Based Approaches
MERIS	Medium Resolution Imaging Spectrometer
MLC	Maximum Likelihood Classifier
MNDWI	Modified Normalized Difference Water Index
MODIS	Moderate Resolution Imaging Spectroradiometer
MRA	Multi-Resolution Approaches
MS	Multi-Spectral
MSAVI	Modified Soil-Adjusted Vegetation Index
MSI	Multi-Spectral Instrument OR Moisture Stress Index
MUCHLAC	MULTi-Channel extension HLAC
NBAR	Nadir BRDF-Adjusted Reflectance
NBI	New Built-up Index
NBR	Normalized Burn Ratio
NBUI	New Built-Up Index
NDBI	Normalized Difference Built-up Indices
NDFI	Normalized Difference Flood Index
NDMI	Normalized Difference Mud Index
NDSI	Normalized Difference Snow Index
NDVI	Normalized Difference Vegetation Index
NDWI	Normalized Difference Water Index
NIR	Near-InfraRed
NN	Neural Networks
NSA	Numerical and Statistical Approaches
OLCI	Ocean and Land Color Instrument
OLI	Operational Land Imager
PAN	Panchromatic
PanTex	Presence index by ANisotropic Rotation-invariant TEXTural measure
PAR	Photosynthetically Active Radiation
PCA	Principal Component Analysis
PCS	Principal Component Substitution
PROBA-V	PRoject for On-Board Autonomy–Vegetation
PVI	Perpendicular Vegetation Index
RE	RapidEye
RGRI	Red Green Ration Index
RS-2	RADARSAT-2
RVI	Ratio Vegetation Index
S-1	Sentinel-1
S-2	Sentinel-2
S-3	Sentinel-3
SAR	Synthetic Aperture Radar
SAVI	Soil-Adjusted Vegetation Index
SG	Savitzky–Golay
SLC	Single Look Complex
SLSTR	Sea and Land Surface Temperature Radiometer
SRTM	Shuttle Radar Topographic Mission
STAARCH	Spatial and Temporal Adaptive Algorithm for mapping Reflectance CHange

STARFM	Spatial and Temporal Adaptive Reflectance Fusion Model
SVM	Support Vector Machine
SWIR	Short-Wave InfraRed
TIR	Thermal InfraRed
TDVI	Temperature Vegetation Dryness Index
TOPSAR	Topographic Synthetic Aperture Radar
TSAVI	Transformed Soil-Adjusted Vegetation Index
TS-X	TerraSAR-X
UI	Urban Index
VH	Vertical transmit/Horizontal receive (polarization)
VIR	Visible InfraRed
VV	Vertical transmit/Vertical receive (polarization)
WP	Work Package
WT	Wavelet Transform

1 Introduction

The Horizon 2020 (H2020) project, “Evolution of Copernicus Land Services based on Sentinel data” (ECoLaSS) addresses the H2020 Work Programme 5 iii. Leadership in Enabling and Industrial technologies - Space, specifically the Topic EO-3-2016: Evolution of Copernicus services. ECoLaSS will be implemented from 2017–2019 and aims at developing innovative methods, algorithms and prototypes to improve and invent future next-generation operational Copernicus Land services from 2020 onwards, for the pan-European and Global Components. ECoLaSS will make full use of dense Sentinel time series of optical (S-2, S-3) and Synthetic Aperture Radar (SAR) data (S-1). Rapidly evolving scientific as well as user requirements will be analysed in support of a future pan-European roll-out of new/improved Copernicus Land Monitoring services, and the transfer to global applications.

This report constitutes a methods compendium of the investigated Sentinel-1/-2/-3 integration strategies aiming at developing and testing integration strategies for S-1, S-2 and S-3 data to allow benefitting from their complementary multi-resolution, multi-temporal and multi-sensor characteristics. The objective of WP 31 is to investigate the possibilities of combining S-1, S-2 and S-3 data with regards to the envisaged evolution of Copernicus Land Services addressed in ECoLaSS.

1.1 Purpose and objectives

With the combination of S-1 and S-2 data, the integration of complementary information is established, resulting from different physical interactions with the land surface, describing primarily different characteristics of the Land Cover/Land Use (LC/LU) objects. The combination of SAR and optical data can improve the differentiation of vegetation classes and therefore increase classification accuracies. This can be achieved by combining S-1-derived information of the plants structure and the seasonal development of these classes (together with the changing situation of water content, both in the plant canopies and the soil) with information, extracted from optical time series (e.g. S-2) along the year, which indicates the change fraction of green (photosynthetically active) vegetation as a main feature.

Another kind of integration is addressed concerning time series of S-2 and S-3. These sensors deliver a corresponding set of spectral bands, sensible for the same biophysical properties with nine overlapping spectral bands in the visible and NIR spectral regions of both sensors, but lower spatial resolution (S-3). The additional data-takes and denser time series derived from S-3 offer high potential generating a fusion product of both satellite sensors using interpolation methods.

The objectives of the WP are

- to identify adequate pre-processing steps enabling complementary information integration and fusion;
- to identify and explore suitable time series indicators from optical data (S-2): e.g. LAI, FCover, indicators including Red Edge and SWIR bands, wetness sensitive indicators;
- to identify and explore suitable time series indicators from SAR data (S-1): e.g. Sigma Nought backscatter coefficient in Co-Pol, Cross-Pol bands, polarisation ratios, textural parameters, indicators representing changes in water content, etc.;
- to explore SAR and optical based indicator approaches as parallel inputs in classification /post-classification schemes;
- to assess the potential of improving S-2 time series by fusion with S-3 information for mapping LC (cloud compensation);
- to define and develop interpolation and fusion tools of S-2 and S-3 data.

The ECoLaSS project follows a two-phased approach of two times 18 months duration. This deliverable comprises the first issue. In the second 18-month project cycle, a second issue of this deliverable will be

published, containing all relevant updates concerning the benchmarking of S-1/S-2 as well as S-2/S-3 integration and fusion methods.

1.2 Outline

Chapter 1 of this document is the Introduction. Chapter 2 gives background information on remote sensing for land use / land cover analysis. It outlines the limitation of using optical or SAR times series data solely and the advantages of integrating or fusing them for different classification applications. Chapter 3 describes the state of the art of fusion and integration methods for the fusion of S-1 and S-2 as well as S-2 and S-3 and identifies candidate methods for a possible application within ECoLaSS, while chapter 4 describes the testing and benchmarking of these identified candidate methods. Finally, chapter Section 5 gives conclusions and an outlook.

2 Remote Sensing for LC/LU Analysis

One of the major challenges of past pan-European high resolution optical satellite image coverages (e.g. 2006, 2009 and 2012) has been data gaps due to high frequency cloud cover and low sun incidence angles. This has a large impact on LC/LU derivation. In the past, this caused several problems with respect to a) product completeness (data gaps due to cloud cover in the final products), b) decreased thematic accuracy in specific regions (e.g. image acquisition not suitable with relation to phenology), c) inconsistency between planned reference year (e.g. image data 2012 +/- 1 year) and actual implementation (partly 2012+2 years for gap filling), d) homogeneity of the product (EO data situation different between most regions of EEA-39), and e) delays in the production of the Copernicus High Resolution Layers (HRL). The need to improve this situation was already expressed by EEA, who is implementing the Copernicus Land Services on pan-European and local level. It is expected, that the availability of Sentinel-2 satellite(s) will significantly improve the data situation. Nevertheless, due to heavy cloud cover over specific regions which coincide with important points in time (phenology wise), the usage of alternative image data sources such as SAR (here Sentinel-1) has been expressed (Dufourmont, 2015) and require new strategies how to combine and integrate both data sets and to improve the completeness and homogeneity of full coverage high resolution information products on Land Cover/Land Use Change (LCLUC).

Therefore, the usage of alternative image data and how to combine and integrate SAR (S-1) and optical (S-2/S-3) will be addressed and methods will be developed and tested how to use S-1 SAR data a) as alternative input to close data gaps from optical image sources and b) as complementary information (to S-2) to increase thematic classification accuracies of specific classes or c) to derive information, which can be used in the post-processing.

2.1 Optical time series data and its limitations

Optical remote sensing data is usually provided as multi-spectral imagery, including visible to infrared wavelength. Compared to SAR, optical sensors offer more comprehensible images to derive information about LC/CU. For this purpose, the spectral reflectance as well as further features such as spectral indices describing i.e. the condition of vegetation can be employed. Optical data is available for over four decades (i.e. Landsat archive) and, hence, enables the analysis of dense time series to address e.g., change detection of LC/LU. However, cloud coverage is one of the main obstacles and constrains the use of optical imagery (Joshi et al., 2016). The occurrence of clouds may significantly reduce the density of the optical time series. A further drawback of multi-spectral data (depending on the spectral and spatial resolution) may be the similarities of spectral characteristics of different land cover types, such as between bare soil and built-up areas or considering the discrimination of crop types (Joshi et al., 2016). This may lead to high uncertainties in the resulting LC/LU maps. Furthermore, optical systems deliver the spectral reflectance of the topmost surface and depending on the field of application this might be a disadvantage (Joshi et al., 2016).

2.2 Radar time series data and its limitations

Radar data provide limited spectral space (one wavelength and multiple polarisations) and a high radiometric accuracy which is why an application of radar time series analysis is very suitable for information extraction (Schmullius et al., 2015). Moreover, radar systems record imagery independently from atmospheric conditions, such as cloud coverage (penetration increases with higher wavelength) and provide information about geometric and dielectric properties of the land surface. Depending on the used wavelength, microwaves can also penetrate the land surface or forest cover. This characteristic allows retrieving data on e.g. soil moisture or growing stock volume. With the launch European Remote Sensing 1 (ERS-1) in 1991, SAR imagery became available at a global scale (Schmullius et al., 2015). But there is only a limited number of studies investigating monitoring of the land surface globally using radar

time series (Joshi et al., 2016). Available studies, however, indicate the applicability of radar time series in the context of e.g. land cover classification, grassland monitoring, and biomass estimation (Joshi et al., 2016). Nevertheless, there are also limitations with respect to the use of radar time series. One of them is the availability of speckle noise in all recorded SAR images, which may lead to errors in classification maps. Another aspect is the occurrence of geometric distortions due to topography, limiting the usage in mountainous areas (Joshi et al., 2016).

2.3 Advantages of integration of optical and SAR imagery

With the combination of S-1 and S-2 data, the integration of complementary information is established, resulting from different physical interactions with the land surface, describing primarily different characteristics of the LC/LU objects. The combination of SAR and optical data can improve the differentiation of vegetation classes and therefore increase classification accuracies. This can be achieved by combining S-1-derived information of the plants structure and the seasonal development of these classes (together with the changing situation of water content, both in the plant canopies and the soil) with information, extracted from optical time series (e.g. S-2) along the year, which indicates the change fraction of green (photosynthetically active) vegetation as a main feature.

2.4 Advantages of spatial - temporal fusion of optical imagery

Remote sensing optical sensors must make a trade-off between spatial, temporal and spectral resolutions, but the fusion of optical images offers an interesting way to exploit the full potential of those images by blending their complementary data, thus creating hybrid images at high spectral resolution and high spatial resolution, at the densest available temporal resolution. When the area of interest is experiencing a persistent cloud cover, images created using fusion algorithms are able to tremendously improve the creation of a valuable time series.

This is why another kind of integration can be explored concerning time series of fused images between S-2 and S-3 data. These sensors deliver a corresponding set of spectral bands, sensible for the same biophysical properties with nine overlapping spectral bands in the visible and NIR spectral regions of both sensors, but lower spatial resolution (S-3). The additional data-takes and denser time series derived from S-3 offer high potential generating a fusion product of both satellite sensors using interpolation methods.

On the one hand, the Sentinel-2 multi-spectral instrument (MSI) provides a low temporal resolution time series of high spatial resolution images such as images produced by Landsat, Ikonos or Quickbird. In fact, Sentinel-2 images exhibit a spatial resolution ranging from ten to sixty meters, a low revisit time of five to six days, and twelve spectral bands. On the other hand, Sentinel-3 ocean and land color instrument (OLCI) provides a dense time series of low spatial resolution images with a high spectral resolution and enough spectral overlap with the latter, such as images produced by Sentinel-3, but also by other satellites like PROBA-V, MODIS or MERIS. The low spatial resolution at three hundred meters is compensated by a frequent revisit time, from one to three days, and twenty-one spectral bands.

3 State-of-the Art

To monitor land cover and its changes, Earth observation (EO) data with a high temporal and spatial resolution are required. However, up to recently these data needs could only be satisfied by employing data from more than one EO satellite (Gao et al., 2015). Nevertheless, the available EO sensors differ extensively in terms of spatial resolution, temporal acquisition repetition cycles, and spectral bands (Gao et al., 2015). Therefore, data fusion approaches have been developed to combine the advantages of different sensors and provide higher value of data and/or classification results. In general, fusion approaches integrate data with different spectral and/or spatial resolutions from two or more sensors in order to exploit both their high spectral and temporal resolution properties. Furthermore, fusion approaches target the challenges of missing data in a time series (Chust et al., 2004; Reiche et al., 2015). This way, different fundamental physical principles can be used as synergetic information on land properties and compensate the limitations of using only single datasets (Joshi et al., 2016). In this context, the European Sentinel fleet with different sensors on board provide the great opportunity to achieve more accurate results by fusing their data. The Sentinels with the designed unique acquisition strategies S-1, S-2, and S-3 bring up new opportunities and challenges for optical multi-spectral and SAR (C-band) land cover classification on local, continental and global scale with high spatial and temporal resolution (Ferrant et al., 2017; Molina & Datcu, 2016).

In general, image fusion approaches in remote sensing can be categorised according to their level of integration, namely: i) pixel level fusion, ii) feature level fusion, and iii) decision fusion (Joshi et al., 2016; Pohl & Van Genderen, 1998). The image fusion on pixel level is the computationally most intensive approach because it is referring to the lowest processing level by merging measured physical parameters of two EO datasets at pixel level (Pohl & Van Genderen, 1998). This approach requires a very high geometric accuracy at sub-pixel level to avoid artificial errors being introduced to the fused dataset. Therefore, image data need to be resampled to a common pixel spacing as well as map projection and need to be cut to a minimum area shared by all datasets (Pohl & Van Genderen, 1998).

The feature level fusion uses different features derived from optical and SAR data, which are further used for classification purposes. Therefore, it requires an image segmentation of the used image data and an extraction of the object features, which correspond to initial image characteristics depending on their environment such as extent, shape and neighbourhood (Pohl & Van Genderen, 1998). Advanced fusion approaches use feature extraction from individual sources to selectively induce spatial detail and thus enhance the feature space for better discrimination of objects (Pohl & Van Genderen, 2015; Stefanski et al., 2014).

Decision fusion methods combine results obtained through separate classifications of optical and SAR data (Joshi et al., 2016). This approach has the advantage of being less computationally intensive. Indices and statistics for the classification are calculated for each data set separately and the results of classification are combined by logical AND functions (Pohl & Van Genderen, 1998). The extracted indices and applied classification approaches depend strongly on the thematic focus (i.e., imperviousness, forest, grassland, permanent water bodies, and wetlands).

First, this State-of-the-Art section describes necessary pre-processing steps to enable complementary information integration and fusion (section 3.1). Methods for the fusion of optical and SAR data to improve classification results are described in section 3.2. Section 3.3 focusses on fusion approaches for high spatial/low temporal and high temporal/low spatial resolution data from different optical sensors (e.g., S-2 / S-3) to exploit the advantage of both datasets. Here, spectral, spatial, temporal interpolation and/or fusion approaches (section 3.3.1) as well as spectral and textural time series metrics/variables (section 3.3.2) are described. The identified approaches are mentioned and discussed in detail keeping the main objectives of the ECoLaSS project such as the update of HRL and LC/LU classification by

improvement of the thematic classification in mind. Section 3.4 discusses candidate integration and fusion approaches for benchmarking.

3.1 Pre-processing steps enabling complementary information integration and fusion

Before the actual multi-sensor data fusion, it is of utmost importance to perform all necessary image correction and pre-processing steps (especially dealing with sensor specific effects) to provide the best single data geometry and radiometry as image fusion is generally performed on pixel level (Pohl & Van Genderen, 1998). As multi-sensor data can vary in their spatial and temporal resolution, the pre-processing of the data has to be adjusted with respect to the specific needs and field of application, including sensor specific steps such as calibration, speckle reduction (SAR) or atmospheric correction (optical), and geocoding as well as resampling to a common pixel size (Pohl & Van Genderen, 2015).

A major challenge considering the fusion of optical and SAR imagery is to ensure an accurate co-registration, since errors lead to artefacts and misclassifications (Pohl & Van Genderen, 1998). The objective is to guarantee that measurements of the Earth's surface are accurately aligned in all available images (Pohl & Van Genderen, 1998; M. Schmitt & Zhu, 2016).

3.2 Integration of S-1/S-2 complementary information

The complementary information of optical and SAR EO data provide enhanced information on the LC/LU (Joshi et al., 2016). While optical data are affected by the physical-chemical characteristics of the surface (such as leaf structure, pigmentation or moisture) SAR data represent the geometric and dielectric properties of the surface (Woodhouse, 2006). Through their multi-spectral bands ranging from visible to near infrared wavelengths, optical data provide information on diverse land covers. SAR data on the other hand are usually acquired in a single frequency for each sensor and interact with the structural characteristics of the surface depending on the wavelength, incidence angle of the sensor, as well as roughness and moisture content (Joshi et al., 2016). For the update of specific HRLs or LC/LU products relevant on a global level, additional SAR data can improve the thematic classification of various classes (e.g. urban areas, forest), as they react to physical structures of the scattering elements (Joshi et al., 2016). Balzter et al. (2015) already demonstrated the potential of SAR data to support the assessment of CORINE land cover (CLC) using multi-seasonal S-1 images and derived products from the Shuttle Radar Topographic Mission (SRTM) DEM. S-1 and S-2 data deliver complementary information. Hence, land cover classification tasks can benefit from the fusion of both data types leading generally to higher mapping accuracies.

3.2.1 SAR data as alternative input to close gap from optical imagery

Optical time series have the most suitable spectral information for discriminating different vegetation types and have been applied most among the different sensing systems. However, their main disadvantage is their sensitivity towards weather conditions such as cloud cover, which hampers their suitability in operational applications (Blaes et al., 2005). On the contrary, SAR data are acquired independently from weather and daytime conditions and generally allow a better discrimination of vegetation types due to their diverse response to different polarisation signals (Betbeder et al., 2015; Hill et al., 2000; Schuster et al., 2015; Anne M. Smith & Buckley, 2011). Compared to optical data microwaves are less affected by the physical-chemical characteristics of the surface, but rather by its structure such as geometry and roughness (Woodhouse, 2006). Active energy scattered by vegetation is dependent on the size, density, orientation, and dielectric properties of elements compared to the size of radar wavelength. Therefore, single wavelength bands of radar signal can help to differ between roughness and moisture content of the surface. In case of multiple bands of SAR backscatter (i.e., composition of polarization or intensity) physical structures of scattering elements can be derived. According to Joshi et al. (2016), most studies utilise multi-spectral reflectance values or spectral signatures as well as phenological indices (e.g. NDVI, EVI, LAI), water indices (NDWI, MNDWI), and different band ratios and

band differences from optical data and polarised backscatter coefficients from SAR data. It has to be taken into account whether only one single time step or multi-temporal information is being used as input dataset and what output temporal resolution is required.

3.2.2 SAR data as complementary information to S-2

This subsection presents studies and methods dealing with the synergetic use of optical and SAR imagery to enhance accuracies of classification results. The thematic focus of this section is on applications for the classification of the thematic classes of the HRLs, hence, forest and vegetation monitoring, agriculture and grassland, urban areas, as well as water, wetlands/wetness and soil moisture.

Forest and natural vegetation

In the context of forest and natural vegetation monitoring, several studies are dealing with fusion and/or synergetic use of optical and SAR data. Reiche et al. (2015) presented a pixel based tool called MultiFuse, which is based on time series of Landsat Normalized Difference Vegetation Index (NDVI) and ALOS PALSAR-L-band backscatter data. It exploits the full information content of both optical and SAR time series data for the detection of abrupt human induced deforestation in tropical regions. At this, pre-processing of optical data comprises cloud cover / cloud shadow masking using the FMask algorithm (Z. Zhu et al., 2015), atmospheric correction, and reprojection. The pre-processing of PALSAR data includes multi-looking, radiometric calibration using standard calibration coefficients, topographic normalisation and geocoding. Based on the pre-processed optical data a NDVI time series is calculated. The SAR data is used to compute a time series of HH, VV images and a HHVV ratio. Next, the SAR images are temporally filtered by an adaptive multi-temporal approach to reduce speckle noise. The actual fusion consists of two main steps. First, the relationship between both Landsat NDVI and PALSAR backscatter time series is analysed by means of a correlation analysis. Next, a regression model is applied to estimate a time series based on the available data. Reiche et al. (2015) conclude that the classification results based on NDVI time series only provide decreased spatial and temporal accuracy. On the contrary, the fused dataset indicates significant improvements in deforestation detection compared to monosource observations. Furthermore, the authors note that the multi-temporal speckle filtered HHVV ratio dataset shows the strongest correlation with the NDVI time series. This might be due to reduced sensitivity of the ratio index towards environmental effects such as changing moisture conditions.

Lehmann et al. (2015) analysed the fusion of SAR and optical data in the framework of a large-scale operational forest monitoring system. This study assessed the contribution of complementary information derived from Landsat, L-band PALSAR, and C-band RADARSAT-2 (RS-2) data for forest detection. For this purpose, independent as well as joint SAR/optical classifications have been tested. The authors investigated a “low cost” approach by considering advantages of established and proven monitoring systems. Thereby, they focused on temporal consistency considering time series of remote sensing data instead of single acquisitions. The pre-processing of Landsat data includes reprojection to a common spatial reference, calibration to top-of-atmosphere reflectance, correction of scene-to-scene differences (using bidirectional reflectance distribution functions (BRDF)), calibration to a common spectral reference (using invariant targets), and correction for differential terrain illumination. Additionally, the pre-processing of PALSAR and RS-2 data includes multi-looking, speckle filtering (Lee filter), geocoding, radiometric calibration and normalisation, as well as correction for terrain-induced illumination differences (Lehmann et al., 2015). As mentioned before, also in this study the co-registration of SAR and optical data are essential. The authors applied a digital image correlation (DIC) approach which is based on gradient cross-correlation. Furthermore, the authors tested 18 different texture measures related to the degree of disorder, similarity and central tendency on pixel level. The combination of Landsat and C-band was found to provide highly enhanced results, whereas the texture information and single-date C-band SAR data delivered only limited improvements. The analysis of the used feature space indicates that adding texture features did not automatically correlate with significant improvements of forest classification results. Nevertheless, texture features improved the results in

distinct and more complex areas such as urban regions. In such context, the consideration of texture features depends on the scale of the study area and the spatial resolution.

A study of Vaglio Laurin et al. (2013) presents an approach based on multi-spectral Landsat TM imagery, the Advanced Visible and Near Infrared Radiometer type 2 (AVNIR-2) and PALSAR synergies for forest and land cover mapping in the tropical regions of Africa. The optical data is atmospherically corrected with hemispherical directional reflectance factor (HDRF) using the Fast Line-of-Sight Atmospheric Analysis of Spectral Hypercubes (FLAASH) algorithm of the ENVI software. In addition, a haze removal is performed. Multi-looking, terrain-correction and geocoding is applied to PALSAR images. The texture variables used in this study include the mean, entropy, correlation, variance, and second moment based on Grey-Level Co-Occurrence Matrix (GLCM). However, the calculation of texture features is limited to bands that are sensitive to vegetation. Hence, bands 4, 5, and 7 of Landsat TM, bands 3 and 4 of AVNIR-2, as well as for both PALSAR polarizations are considered, using 64 grayscale quantization levels, 1 pixel shift and 3×3 , 5×5 , 7×7 , 9×9 and 15×15 window sizes. For classification purposes two methods, specifically, the Maximum Likelihood (MLC) and Neural Networks (NN) classifiers are used. The results show that the combination of the abovementioned data sources provides the best results for both classification methods (91.1% and 92.7% for Landsat TM as optical input and 95.6% and 97.5% for AVNIR-2 as optical input, respectively). In this study, texture features improve the classification results significantly by 10.1% and 13.2%, respectively (Vaglio Laurin et al., 2013).

A near real time forest disturbance mapping based on S-1, S-2 and Landsat-8 time series data is conducted by Hirschmugl et al. (2017). They used a sequential approach where an initial forest / non-forest classification is derived from optical data and, afterwards, forest disturbance data are derived by means on the Bayes' theorem using SAR and optical data stacks. Disturbance mapping is performed separately on each input dataset and then fused to one forest disturbance dataset based on specific weighting functions. For optical data the authors apply common pre-processing steps using FMask for Landsat-8 and Sen2Cor for S-2 data. The S-1 data are pre-processed with Joanneum Research software RSG (www.remotesensing.at) including processing to gamma nought based on SRTM and multi-looking to 20m. A modified Frost and a multi-temporal filter with a window size of 3x3 pixels are used to reduce speckle noise. In this study, all available images are reduced to temporal statistics including the metrics mean, minimum, maximum backscatter, standard deviation, coefficient of variation, mean of the first three images, and mean of the last three images. Next, the information on forest disturbance is derived using a threshold-based approach with the assumption that forest cover change is characterised by high backscatter variation similar to agricultural areas (Hirschmugl et al., 2017). At this, positive backscatter values are related to vegetation regrowth and negative backscatter values with vegetation loss. The final combination of individual classified results is based on defined probabilities and weighting factors by the user. The results indicate that when using only S-1 for forest disturbance detection 43.56% of the areas are classified correctly. For the optical data the percentage of detected areas amounts to 79.95%. To sum up, the synergistic use of optical and SAR improves the detected percentage of disturbed areas to 83.67%.

Agriculture and grassland

With regards to agriculture and grassland applications, several studies have been performed over the last two decades using optical and SAR data to achieve higher thematic accuracies. In similar studies, classification results derived by either optical data, SAR data (C-, X-, L-band) or the combination of both were compared to each other. The objective of these studies was to create a dense time series during the growing season of crops, combining regular SAR time series and optical time series with irregular time intervals using derived statistical metrics. A variety of approaches jointly apply multi-sensor imagery from SAR and optical satellites for the classification of vegetation classes, such as crop types (Blaes et al., 2005; Brisco & Brown, 1995; McNairn et al., 2009), and crops combined with more general land-cover classes (Waske & Benediktsson, 2007; Waske & van der Linden, 2008), or for the estimation of herbaceous biomass (Svoray & Shoshany, 2003). Villa et al. (2015) investigated main crop type

identification by SAR and optical time series up to the early growing season (here mid of July), using indicators like the Enhanced Vegetation Index (EVI), Red Green Ratio Index (RGRI) and the Normalized Difference Flood Index (NDFI) in optical data and sigma nought backscatter coefficients from X-Band SAR. Bach et al. (2012) and Dotzler et al. (2013) demonstrated the information potential of TerraSAR-X (TS-X) for certain growing phases of crop types delivering similar results compared to a Leaf Area Index (LAI) retrieval from RapidEye (RE) data, in order to perform yield modelling for wheat and to assess heterogeneous growing patterns within the fields. Jordi Inglaia et al. (2016) presented an approach for early crop type identification especially for the start of growing season when cloud coverage is a major challenge. They assessed the impact of data fusion using SAR image features aiming at temporal gap-filling of optical time series. Polarisation ratio, local mean and VV data with textures described by Haralick et al. (1973) were used and assessed as useful features enhancing the accuracy of the results. This kind of crop detection is essential for yield forecasting and irrigation management, especially for crop types with more than one annual cycle. Le Hegarat-Mascle et al. (2000) investigated the use of ERS data and Landsat TM over a testsite east of Paris dominated by agriculture with ten different land cover types based on unsupervised classification and Dempster-Shafer evidence theory framework. The study shows that using multi-source data as input to the classification leads to more robust and reliable results. A systematic improvement was found by fusing SAR and optical data sources especially for land cover types with minor surface coverage.

Notarnicola et al. (2017) used S-1 and S-2 data for mountain crop monitoring. S-1 backscatter coefficients in VV and VH polarisation were used to monitor the trend over different crop types that are extracted from the existing land cover classification CORINE 2012 (meadows, pasture, orchard, vineyards and forest as additional class). The generated time series from S-1 data was compared with S-2 NDVI time series. According to the preliminary results of this study, the highest dynamics are associated to meadows, which were strongly managed in terms of fertilisation, irrigation, and mowing. The signature of meadows varies between -16dB and -12dB and from -22dB and -17dB for VV and VH polarisation, respectively. This trend is clearly different from natural grassland as well as from other classes. Furthermore, the study indicates that due to the C-band configuration both polarisations (VV and VH) are strongly dominated by vegetation characteristics and may have a limited sensitivity to soil characteristics. Notarnicola et al. (2017) found a high relation between the features VH polarisation and S-2 NDVI with a coefficient of determination of 0.81.

Recently, Veloso et al. (2017) published a study focusing on the temporal behaviour of crops (wheat and barley, rapeseed, maize, soybean and sunflower) based on data comparable to S-1 and S-2. For this, S-1 data are pre-processed with SNAP software to derive the calibrated backscatter coefficient. Additionally, a multi-looking is applied to reduce speckle noise resulting in an output image at a spatial resolution of 20m. Furthermore, terrain correction is applied to generate accurately geocoded images by correcting geometric distortions (foreshortening, layover and shadow) using SRTM data (Veloso et al., 2017). The used optical data are atmospherically corrected using the Multi-sensor Atmospheric Correction and Cloud Screening prototype (MACCS) spectro-temporal processor (Hagolle et al., 2008; Hagolle et al., 2010, 2015). With respect to crop monitoring, the study showed that wheat and rapeseed are better distinguished using VH and VV backscatter between March and July and using NDVI between November and December. Regarding summer crops, Veloso et al. (2017) recommend using VH/VV and VV to separate maize, soybean and sunflower during the heading/flowering phase. Their results also indicate that for the identification of the crop types barley and maize, both NDVI and VH/VV profiles provide reliable results.

Navarro et al. (2016) applied crop monitoring for the estimation of crop water requirements. For this purpose, they used SPOT NDVI and time series of dual (VV + VH) polarisation backscattering based on S-1 to compute the basal crop coefficient curve for four crop types (maize, soybean, bean and pasture) and to estimate the length of each phenological growth stage. The main objective of this study was to assess the potential of multi-temporal and multi-source data for crop parameter estimation and crop type

identification at high spatial (10m) and temporal (5 days) resolution focusing on irrigated agriculture. The authors observed a significant correlation of determination between NDVI and backscatter time series for all considered crop types, pointing that multi-spectral imagery can be replaced by SAR imagery data to fill gaps caused by cloud coverage. Furthermore, the authors assessed the integration of S-1 VV + VH polarised data into the classification process and compared the obtained accuracies between the different configurations. For classification purposes, two supervised methods, specifically the support vector machine (SVM) and neural network (NN) are used. Here, the results indicate that NN delivers slightly better accuracies compared to the SVM classifier. However, the land cover classification could not be improved when using SAR and optical data in combination, which could be seen in the results where the highest overall accuracy was achieved by using SPOT images solely.

The combined use and/or comparisons of classifications by optical and SAR intra-annual time series or multi-seasonal data were also performed for grassland mapping (Dusseux et al., 2014; Hill et al., 2005; Schuster et al., 2015). A. M. Smith et al. (1995) analysed ERS-1 SAR data together with Landsat TM, SPOT VIR, and airborne optical imagery to assess the combination of radar and optical data for monitoring rangeland in the Agriculture and Agri-Food Canada Research Substation at Onefour (Alberta) by means of discriminant function analysis (DFA). The combination allowed obtaining an improved categorisation of the vegetation classes with respect to considering each data type separately. Moreover, while optical data proved to be more suitable to characterise the vegetation status, SAR imagery provided key information about the structure and surface topography. Also Price et al. (2002) used a classification system based on the DFA to study the separability of three tallgrass land management practices in eastern Kansas (USA), where usually cool- and warm-season grass species occur, by means of three multi-seasonal Landsat TM and four multi-seasonal ERS-2 SAR images, as well as their combination. The results showed that by using Landsat TM data alone, performances were better than those obtained with ERS-2 imagery and, when combined, the SAR data did not allow increasing the classification accuracy. Hill et al. (2005) showed the potential of improving the categorisation of heterogeneous herbaceous cover in pastures and grasslands by combining independent classifications obtained by means of mono-temporal Landsat TM and Jet Propulsion Laboratory AirSAR data. Experiments were performed for a test site in the Cervantes area (Australia) using an unsupervised version of the Complex Wishart classifier for the C-, L-, and P-band polarimetric SAR data as well as a principal component analysis on the green, red and near-infrared Landsat bands followed by a centroid distance measure clustering. In particular, they were able to map vegetation types based on the different sensitivity of SAR and multi-spectral sensors to specific vegetation characteristics. Erasmi (2013) assessed the capability of combining optical (six RE scenes) and SAR (four RS-2 and six TS-X scenes) data for the classification of semi-natural habitats over the study site Schorfheide Chorin in eastern Germany and compared the results with single sensor classifications. The object-based classification was performed by means of a classification and regression tree (CART) algorithm. Results showed that single-sensor classifications based on multi-temporal RE data outperformed the ones carried out with TS-X and RS-2 data and demonstrated that bi-sensor combinations of optical and SAR data resulted in classification accuracies between 60.83% and 84.53% (with RS-2 polarimetric data providing higher classification accuracies than TS-X). Furthermore, Talab-Ou-Ali et al. (2017) used S-1, S-2 and SPOT data for monitoring coastal vegetation in France. Also Chang and Shoshany (2016) conducted preliminary research for S-1 and S-2 data focusing on shrubland biomass estimation. Their fusion model showed 14% improvement compared to single sensor models (R^2 increases from 0.72 to 0.86). Their proposed fusion technique is mainly controlled by S-2 data and is supplemented by an active S-1 data supporting vegetation structure/density information.

For all vegetation covered targets, only a limited additional benefit is seen because of the high level of temporal decorrelation (Morishita & Hanssen, 2015; Wei & Sandwell, 2010). In the context of crop area and crop status monitoring, interferometric coherence has the potential to enable the mapping of stable (unvegetated) surface with possibilities of farming practises and crop detection. To date, most common polarimetric decompositions (Freeman & Durden, 1998) can only be computed for fully polarimetric (quad-polarimetric) data. S-1 only contains dual-cross-polarimetric capabilities (HH-HV, or VV-VH) for

which there is a need for further developments. Alternative concepts for the use of dual-polarimetric data have been recently published by A. Schmitt et al. (2015).

Urban

Considering the usage of multi-source data in the framework of land cover and urban applications there is a number of recently published studies. Michelson et al. (2000) successfully applied Landsat TM and ERS SAR data for country-wide land cover classification over Sweden. Balzter et al. (2015) have demonstrated the potential of SAR data, to support the assessment of CORINE LC using multi-seasonal (two coverages) S-1 images and derived products from SRTM DEM. Haas and Ban (2017) used S-1 and S-2 data for ecosystem mapping within urban areas based on image segmentation and classification. The synergy of S-1/S-2 enabled large-scale urban analysis with utilising spatial characteristics and topological relations (e.g. area, contiguity, perimeter-to-area ratio and distance). Another study of Chen et al. (2003) used Intensity–Hue–Saturation (IHS) transformation to integrate the high spectral resolution, provided by hyperspectral data (Airborne Visible Infrared Imaging Spectrometer, AVIRIS), and the surface texture information, derived from radar data (Topographic Synthetic Aperture Radar, TOPSAR), into a single image of an urban area. In this way, several urban land cover types are resolved to a larger degree using the higher spectral and spatial resolutions and the synergistic visual content provided by the fused image. Furthermore, Marconcini et al. (2017) recently presented an approach employing the temporal statistics of different spectral indices derived from Landsat-8 and of the S-1 backscattering to classify urban areas at a 10m spatial resolution on a global scale.

Water and wetlands/wetness

Yesou et al. (2016) used S-1 in the context of flood and wetland mapping and showed that it ensures monitoring of water bodies, whereas optical S-2 imagery provides complementary information on vegetation, floating or growing on sand banks. Furthermore, Taha and Elbeih (2010) concluded that for water/non water separation HIS fused data clearly indicate highest accuracies. Jenerowicz and Siok (2017) conducted tests on mapping water bodies based on S-1 and S-2 data, comparing the results of individual features and thresholds. The results also imply that complex detection of water bodies e.g. quality monitoring of water reservoirs will be improved. Clement et al. (2017) analysed detailed flood mapping using different polarisations of S-1 data.

Q. Gao et al. (2017) presented an approach for soil moisture mapping over agricultural fields at 100m spatial resolution based on the interpretation of S-1 data recorded in the VV polarisation and combining S-1 with S-2 data for the analysis of vegetation effects. The authors present an approach to map soil moisture using S-1 and S-2 data in a synergistic way. The reduction of spatial resolution from 10m to 100m is conducted to decrease uncertainties due to different types of heterogeneities in agricultural fields such as local changes in roughness as well as heterogeneities in vegetation cover. All available S-1 data are pre-processed with respect to noise removal, radiometric calibration, and terrain correction. S-2 data are used to calculate NDVI, but prior to NDVI derivation a cloud mask is generated using the QA60 band. In this study, two methods are proposed to retrieve soil moisture. The first one comprises a change detection technique based on an inversion approach, which was already successfully applied on ERS data and now adjusted to S-1 data. The second one takes into account the difference of the S-1 backscatter coefficient observed over two consecutive acquisitions. By analysing two consecutive observations only a small temporal change of vegetation is expected for a nearly constant value of roughness and thus the difference of the backscatter signals depend mainly on the change in soil moisture. Both methods also take into account the S-2 NDVI. The results of this study indicate that both methods are suited for soil moisture estimation and the necessity to further research with respect to vegetation discrimination and the consideration of a larger time series of S-1 (Gao et al., 2017).

A further study of Poggio and Gimona (2017) compared MODIS, Landsat, S-2 and S-1 data for Digital Soil Mapping (DSM). The authors applied several configurations and concluded that the synergistic use of

optical and radar datasets provided the best estimation models and most accurate results. The findings include that S-1 data is suitable for the analysis of soil properties and texture in particular. Also Baghdadi et al. (2015) worked on soil moisture and LAI retrieval over irrigated grasslands from RS-2 and Landsat-7/-8 data. The main objective was to study the relevance of features extracted from SAR (backscattering coefficient, polarimetric information) and optical images (NDVI, Fraction of Absorbed Photosynthetically Active Radiation (fAPAR) and Fractional Cover (FCover)) for retrieving soil moisture, leaf area index, biomass, and vegetation water content and height. The authors summarised their outcome as follows: i) HH polarisation is the most relevant information among the SAR layers, ii) dual or full polarisation modes do not improve the estimation of soil moisture and vegetation parameters, and iii) the use of polarimetric parameters (Shannon entropy and Pauli components) does not improve the estimation of soil moisture and vegetation parameters.

3.2.3 Preliminary conclusions

As described above, first studies using the combination of S-1/S-2 data show promising results and underline that accuracies of different thematic classifications based on fused image data exceed those based on single source data (Joshi et al., 2016). However, most studies focussed on using optical/SAR fusion for improving mono-temporal classifications to define more enhanced land cover properties rather than for change detection (Joshi et al., 2016). Besides, it is key to select suitable data fusion techniques for different land cover classifications and change detection (Lu et al., 2014).

The above mentioned studies and reports underline the positive synergy between SAR and optical data. Especially, the combination of data of the Sentinel fleet show great potential in terms of geometric consistency and enhancement of thematic classification and change detection. For the update of specific HRLs or LC/LU products relevant on a global level, complementary information derived from S-1 can improve thematic classification based on optical data of various classes (e.g. settlements structures or forest differentiation), as they react mainly on vertical or structures with steep slopes based on double bounce backscatter effects.

In order to maintain the experiences from previous Copernicus HR Layer production, it will be assessed, whether and how parameters derived from dense SAR time series can supplement the available optical time series data for the production of incremental HRLs. For crop area and crop status monitoring, SAR based parameters can provide complementary information to optical based parameters due to their different physical interactions with the land surface. Therefore, different characteristics of LC/LU objects can be described and classification can be improved.

3.3 Integration of S-2/S-3 (fusion)

This subsection focusses on methods for the fusion and integration of S-2 and S-3. Thereby, current state-of-the-art methods for a spectral, spatial as well as temporal interpolation/fusion are being presented (subsection 3.3.1). Furthermore, spectral and textural time series metrics/variables are being identified suitable to describe seasonal dynamics of LC/LU and thus being applicable in a S-2/S-3 fusion/integration approach (subsection 3.3.2)

3.3.1 Spectral, spatial, temporal interpolation and/or fusion approaches

This subsection investigates and describes various spectral, spatial and temporal interpolation and fusion approaches for the integration of Sentinel-2 and Sentinel-3 time series. It assesses in particular the potential of improving Sentinel-2 time series by fusion with Sentinel-3 information to avoid land cover mapping distortions caused by cloud cover. Firstly, an overview of the optical data fusion at the pixel-level is presented. Secondly, advanced and appropriate methods for the Sentinel-2 and Sentinel-3 data fusion are explained in detail.

3.3.1.1 Overview of the optical data fusion at the pixel-level

The pixel-level fusion, mainly focusing on optical data, is the combination of raw data from multiple sources into single resolution data, which are expected to be more informative and synthetic than either of the input data. The purpose is to improve spatial resolution, enhance structural and textural details or retain the spectral fidelity of the original multi-spectral (MS) data simultaneously (Zhang, 2010). There are many ways to address pixel-level image fusion due to its diverse input in terms of multi-modal images and its variability in terms of targeted outcome (Pohl & Van Genderen, 2015). Depending on users' need, a large variety number of pixel-level algorithms have been developed and widely applied for the data fusion of remotely sensed images.

In particular, much attention has been paid on the aspect of increasing the spatial resolution of MS images by introducing spatial detail derived from a higher spatial resolution panchromatic channel (PAN), while preserving the high spectral resolution properties of MS images. This fusion method is commonly called 'pansharpening'. A major reason for its popularity is the accessibility of single platform acquisitions, which avoids the introduction of errors due to temporal changes on the ground as well as geometric problems arising from multiple platform orbits. Thus, pansharpening has become one of the most popular approaches in remote sensing image fusion (Pohl & Van Genderen, 2015; Zhang, 2010).

Although there are many categorizations suggested for remote sensing data fusion approaches, pixel-level pansharpening fusion methods have been categorized by Pohl and Van Genderen (2015) in five groups: (i) component substitution (CS); (ii) numerical and statistical approaches (NSA); (iii) modulation-based approaches (MBA), (iv) multi-resolution approaches (MRA), and (v) hybrid techniques. (i) The CS techniques convert a number of bands of the original image into another data space (e.g. another colour space) where one of the resulting channels is replaced by a new image (e.g. higher spatial resolution image). The reverse transform creates the actual fused image containing information from both input data. Within this category, the intensity hue saturation, principal component substitution (PCS), and the Gram-Schmidt techniques are most frequently exploited. CS methods suffer from spectral distortion due to the significant incompatibility of PAN (or any high spatial resolution image) and substituted component. (ii) The NSA perform multiplicative operations, create subtractive and ratios images. Widely used Bovery transform (BT) resides in spectral modelling intended to reach a normalization of the input bands via addition, subtraction and ratio. The principal component analysis (PCA) is also a very popular algorithm. It implies the replacement of the first PC by a high-resolution (e.g. a PAN or a low spatial MS) image. (iii) The MBA uses a ratio between the PAN and its low-pass filtered image with a further modulation of a lower spatial MS image. (iv) Whereas the previous methods are based on various linear combinations and substitutions of the original bands, the MRA are nonlinear. The MRA-based approaches decompose images into multiple channels depending on their local frequency content, employing wavelets, curvelets, contourlets and similar transforms. They find their application in deriving spatial detail to be imported into finer scales or multi-spectral images. The wavelet methods may suffer from color distortions.

Most of these data fusing approaches are devoted to the case of spatial or spectral enhancement of remotely sensed images only in the case of simultaneous images. However, they may not be suitable for capturing quantitative changes in surface reflectance, e.g. caused by phenology (Gao et al., 2006) or crop growth. In addition to the traditional spatio-spectral data fusion methods (typically pansharpening), pixel-level fusion can also aim at increasing the temporal resolution of a sensor of low temporal resolution but high spatial resolution images through fusion with the data with lower spatial resolution but higher temporal resolution (Dominique Fasbender et al., 2009; F. Gao et al., 2006; Sedano et al., 2014; Xue et al., 2017). For multi-temporal data, the purpose of pixel-level fusion is to highlight the informative changes between different times, using either the same or different sensors.

Some methods interesting for the fusion of Sentinel-2 and Sentinel-3 images are explained in more detail here below. Spatial and spectral enhancement methods are firstly explained. Then, by the temporal

component of the fusion between sensors of high and low temporal resolution is reviewed through several applications. Finally, some cases of fusion at the product level are presented.

3.3.1.2 Spectral and Spatial Fusion

Pansharpening and spatial enhancement in a Bayesian data fusion framework

As previously explained, fusion methods for spatial enhancement, or pansharpening methods, are a set of techniques aiming at improving the spatial resolution of remotely sensed multi-spectral images. Pansharpening is frequently applied to a single optical sensor data containing both PAN and MS data, in order to benefit from both sources of information, but sometimes also applied to multi-source data provided by two independent optical sensors differing in spatial, spectral and temporal resolution. Ideally, the outcome of pansharpening is an artificial image identical to the image that the MS sensor would yield provided it had the spatial resolution of the panchromatic.

In Fasbender et al. (2007), Fasbender et al. (2008) and Fasbender et al. (2008), a novel approach to the pansharpening and spatial enhancement problems is suggested within a Bayesian framework, using IKONOS, SPOT 5, SPOT-VEGETATION and ASTER images. A Bayesian data fusion (BDF) framework has been proposed by Bogaert and Fasbender (2007). Initially developed in a spatial prediction context, it also provides a consistent framework for fusing an arbitrary large number of information sources that are related to the same variable of interest. This BDF method relies on statistical relationships between the various spectral bands and the panchromatic band without suffering from restricting modeling hypotheses.

Furthermore, BDF allows the user to weight the spectral and panchromatic information with respect to either visual or quantitative criteria, which leads to adaptable results according to users' needs and study areas (Fasbender et al., 2008). This ability for balancing spectral and spatial information is one of BDF's most appealing features. For example, photointerpreters may wish to favor image sharpness with a weighting parameter close to one, while automated procedures may require a better color consistency and, thus, a lower weight for panchromatic information. Results showed that BDF yielded the highest spectral consistency, and small details were adequately added to the pansharpened images with little artifact as compared to those created using wavelet-based methods. No particular colour distortions are observed and quantitative quality criteria (i.e. correlation coefficients) attest that the BDF framework provides significant results in the case of pansharpening application.

The BDF approach is also tested for the enhancement of the spatial resolution of coarse images using higher resolution images coming from same or different sensors (Fasbender et al., 2007; Fasbender et al., 2008), showing interesting results. Contrary to the pansharpening application, several higher resolution spectral bands were available. The method can be used to derive high resolution reflectance values based on medium resolution observations by taking advantage of a multivariate approach including covariate information (i.e., spectral information is processed as a whole and not band by band). The high values of the correlation coefficients between original and fused coarse resolution spectral bands indicate that no particular colour distortions are noticed, whereas small details and linear patterns were added.

The BDF has performances similar or higher to the wavelets approach. The main advantage of Bayesian approaches is to set the problem in a proper probabilistic framework. In addition, as it does not have any intrinsic limitations on the type of data to be processed or the number of bands to be merged, it could be used for optical/SAR or hyperspectral image fusion.

Multi-spectral and -spatial data fusion between Sentinel-2 MSI and other sensors

In Korosov et al. (2017), a fusion between Sentinel-2 Multi-Spectral Imager (MSI) and Sentinel-3 Ocean and Land Colour Instrument (OLCI) is simulated by choosing the analogue Aqua-MODIS sensor to the Sentinel-3 OLCI instrument. The OLCI data present a good set of colour wavelengths, but a rather coarse (300m) spatial resolution, while the MSI data on Sentinel-2 have much higher spatial resolution (10-60m) but a rather scarce number of spectral channels in the visible spectrum. The data are fused at pixel-level to get products with values of remote sensing reflectance wavelengths of OLCI and with MSI spatial resolution of 60m using an artificial neural network (ANN).

Many of applications indicated that the ANN-based fusion methods had more advantages than traditional statistical methods, especially when input multiple sensor data were incomplete or with much noises. It is often served as an efficient decision level fusion tool for its self-learning characters, especially in LC/LU classification. In addition, the multiple inputs-outputs framework make it to be a possible approach to fuse high dimension data, such as long-term time-series data or hyper-spectral data. Comparison of reflectance values from MODIS and fused data shows high level of agreement and suggests that the developed algorithm can be successfully applied for fusion of data from Sentinel-2 and Sentinel-3 (Korosov et al., 2017).

Currently, more studies are dedicated to the fusion of Sentinel-2 with Landsat images, the most widely accessible medium-to-high spatial resolution multi-spectral satellite data. The Sentinel-2 and Landsat data have similar wavelengths, which provide an excellent opportunity for synergistic use of these two types of satellite sensor data (Wang et al., 2017). Their combination offers a unique opportunity to observe globally at medium spatial and temporal resolution, and thus creates unprecedented opportunities for timely and accurate observation of Earth status and dynamics. This is particularly valuable for areas that are often covered by clouds, thereby, contaminating some Landsat or Sentinel-2 observations.

In Wang et al. (2017), a new approach (the area-to-point regression kriging (BAP)) is presented for the fusion of Landsat 8 Operational Land Imager (OLI) and Sentinel-2 MSI data to coordinate their spatial resolutions for continuous global monitoring. ATPRK treats the coarse band as the primary variable and the fine spatial resolution band (hereafter, fine band) as a covariate. It is an advanced image fusion approach which has the appealing advantage of precisely preserving the spectral properties of the observed coarse images (i.e., perfectly coherent). It was shown to outperform 13 methods in pan-sharpening. The 30 m spatial resolution Landsat 8 bands are downscaled to 10 m using available 10 m Sentinel-2 bands. To account for the LC/LU changes that may have occurred between the Landsat 8 and Sentinel-2 images, the Landsat 8 PAN band was also incorporated in the fusion process. The experimental results showed that the proposed approach is effective for fusing Landsat 8 with Sentinel-2 data, and the use of the PAN band can decrease the errors introduced by LC/LU changes.

The Harmonized Landsat-Sentinel-2 (HLS) project is a NASA initiative to produce a consistent, harmonized surface reflectance product from Landsat OLI and Sentinel-2 MSI data. The HLS will be beneficial for global agricultural monitoring applications that require medium spatial resolution and weekly or more frequent observations. In this context, a “harmonized” reflectance product means that necessary radiometric, spectral, geometric, and spatial corrections have been applied to create a seamless time series, such that it is transparent to the user which sensor contributed any particular observation. To create a compatible set of radiometric measurements, the HLS product relies on rigorous pre- and post-launch cross-calibration activities. The processing chain includes the following components: atmospheric correction and cloud/shadow masking based on OLI and adapted to the MSI data, nadir BRDF-adjustment given the differing solar and view angles associated with Landsat-8 and Sentinel-2, spectral-adjustment, regridding, and temporal composite to produce the M30 (10-day NBAR 30m Landsat-8 OLI or Sentinel-2 MSI harmonized surface reflectance resampled at 30m over the Sentinel-2 tiling system). The spectral-adjustment, or band pass adjustment, relies on a linear fit

between equivalent spectral bands from the two sensors which present small differences. This band-to-band linear regression has been calibrated and evaluated using synthetic data and surface reflectance processed from a large number of hyperspectral EO-1 Hyperion scenes globally distributed.

3.3.1.3 Temporal fusion between high and medium spatial resolution time series

Sentinel-2 data with improved high spatial resolution and higher revisit frequency will play a fundamental role in monitoring land cover at regular intervals. Nevertheless, technological limitations pose challenges for sensor designs, and trade-offs have to be made to balance spatial details with the spatial extent and revisit frequency (Xue et al., 2017). High spatial resolution images, such as Landsat, and Sentinel-2 with revisit cycles of 16 and 5 days respectively, are indeed limited in their applications due to frequent cloud contamination. Cloud-free high resolution imagery may not be available at the required period, which hinders the time series availability and consequently the continuous land surface monitoring. On the contrary, low spatial resolution sensors, such as MODIS, SPOT-VEGETATION and recently Sentinel-3, have a daily revisit period but a relatively low spatial resolution ranging from 250 m to 1000 m, limiting its effectiveness in the monitoring of ecosystem dynamics in heterogeneous landscapes.

In an attempt to overcome these limitations, the synergistic use of the high spatial resolution images such as Landsat or Sentinel-2 time series with the high temporal frequency of coarse resolution sensors (MODIS, Sentinel-3), while taking explicitly into account the spatial resolution discrepancies between images, is investigated. For instance, monitoring agriculture via remote sensing or detecting rapid surface changes are typical applications where the combination of fine spatial resolution and a frequent temporal revisit time is important.

Pansharpening methods previously described are devoted to the case of spatial and spectral enhancement of remotely sensed images only in the case of simultaneous images. This section presents some examples of temporal fusion models, in addition to spectral and spatial merge.

Kalman filtering

A data assimilation method to produce complete temporal sequences of synthetic medium-resolution images combining moderate- and medium-resolution imagery is presented in Sedano et al. (2014). Within the framework of a Kalman filter recursive algorithm (Kalman, 1960) also known as linear quadratic estimation, the method integrates models, observations and their respective uncertainties, with partly or fully missing variables, in the calculation of the synthetic images at time steps for which medium-resolution imagery is not available. It therefore allows continuous monitoring of land surfaces at higher spatial resolution than moderate-resolution sensors and higher temporal frequency than existing medium-resolution sensors. To demonstrate the approach, time series of 30-m spatial resolution NDVI images at 16-day time steps were generated using Landsat NDVI images and MODIS NDVI products at four sites with different ecosystems and LC/LU dynamics. The results show that the time series of synthetic NDVI images captured seasonal land surface dynamics and maintained the spatial structure of the landscape at higher spatial resolution. The method provided a robust performance for input data of variable qualities and environmental conditions, highlighting the relevance of including uncertainties in the integration of multi-sensor remote sensing data.

This method was applied on PROBA-V time series. Kempeneers et al. (2016) present a data assimilation method to increase the temporal resolution of the nadir-viewing 100-m product with the off-nadir 300-m images, having identical spectral specifications, in order to produce a continuous 100-m time series. Indeed, the swath of the nadir viewing sensor is only half of the swath of a single off-nadir viewing sensor. Due to its limited field of view, a global coverage can only be obtained every five days, which is a serious drawback for a number of applications especially in cloud-affected areas. The method implements the Kalman filter recursive algorithm to generate the assimilated imagery at the fine spatial

detail (100 m). The assimilated product is a cloud-free time series at the temporal resolution of the 300-m data, while preserving the spatial detail of the fine resolution data. Quantitative results show the potential of the method for continuous monitoring of land surfaces compared to a simple data assimilation and the Savitzky–Golay (SG) filter.

One of the strengths of the Kalman filter is its robustness to a relatively large number of gaps in temporal time series. Especially in the context of data acquisition with optical sensors in conditions with frequent cloud cover, this is an important asset. The added value of the improved spatial resolution from 300 to 100 m has also been illustrated for monitoring agriculture via remote sensing in this area. It was shown that the synthetic profile at 100 m based on the Kalman filter was better able to capture the phenological patterns of the crops with respect to the original PROBA-V product at both 100 and 300 m.

Recently, the Kalman filter method was used for the implementation of the dynamic land cover product at 100 m resolution provided in the Copernicus Global Land Service (Buchhorn et al., 2017). In order to overcome the low data density and therefore data gaps in the PROBA-V 100 m MC5 time series product, PROBA-V 300 m data which has a daily revisit time is fused in via a Kalman filtering for the input of the classification.

STARFM and ESTARFM

PROBA-V 100-m and 300-m S-1 products were also fused in Zheng et al. (2016) in order to map the biomass and yield of winter wheat, this time using the Spatial and Temporal Adaptive Reflectance Fusion Model (STARFM) (Gao et al., 2006) and the Enhanced Spatial and Temporal Adaptive Reflectance Fusion Model (ESTARFM) (Zhu et al., 2010) algorithms.

F. Gao et al. (2006) used the STARFM to obtain images high in both spatial and temporal resolutions, predicting daily surface reflectance data at the Landsat ETM+ spatial resolution and the MODIS temporal resolution. It is one of the first fusion algorithms that has been widely used for synthesizing Landsat and MODIS imageries. The Landsat images can be sparse in time, letting the MODIS data capture temporal changes. The STARFM accurately predicts surface reflectance at an effective resolution close to that of the ETM+. However, the performance depends on the characteristic patch size of the landscape and degrades somewhat when used on extremely heterogeneous fine-grained landscapes (Gao et al., 2006). To overcome STARFM's inaccurate predictions of the surface reflectance over heterogeneous landscapes, the ESTARFM was proposed and has proven to be extremely effective (Zhu et al., 2010).

A synthetic daily PROBA-V 100 m land surface reflectance was generated (Zheng et al., 2016). The results indicated that this fusion had excellent abilities because the blended reflectance was closely correlated with the observed reflectance. It shows the strong potential of using PROBA-V 300 m data to enhance the temporal resolution of PROBA-V 100 m data.

STARFM and ESTARFM are shown to be useful in capturing reflectance changes due to changes in vegetation phenology, which is a key element of seasonal patterns of water and carbon exchanges between land surfaces and the atmosphere. However, they may have problems in mapping disturbance events when land-cover changes are transient and not recorded in at least one of the baseline high-resolution (e.g., Landsat) images. In order to detect the spatial and transient changes, the Spatial and Temporal Adaptive Algorithm for mapping Reflectance CHange (STAARCH) was introduced by Hilker et al. (2009) to serve change detection of reflectance values used for Landsat and MODIS. Based on Tasseled Cap transformations of both Landsat and MODIS reflectance data, the algorithm detects vegetation changes and employs each optimal Landsat-MODIS image pair in the fusion process.

Bayesian data fusion

A BDF framework was applied in Fasbender et al. (2009) for the update of scarce high resolution images of a first sensor with time series of coarser images from a second sensor. This BDF framework aims at reconciling various secondary information sources into a unique prediction. Although initially proposed in a spatial prediction context, a generalization of this BDF approach was presented here for space-time predictions. Two methods differing with respect to the amount of information sources at finer resolution were considered for the prediction of the target image. Details are provided by the high resolution image whereas the global fluctuations and seasonal trends are provided by the coarser image. The information relevance of the finer image with respect to the fused one is expected to drop along with the change of seasons. Although they only applied the method to a synthetic case study, generalizations of this BDF method are possible in order to tackle real case applications with images having different spectral bands.

In Fasbender et al. (2009), linear regression is used to reflect the temporal dynamics, which, however, may not hold in a variety of situations. Moreover, there may be no regression-like trends in some cases. Xue et al. (2017) developed a formal and flexible Bayesian framework for the fusion of Landsat and MODIS images to obtain images high in both spatial and temporal resolutions. It provides a formal framework for the spatio-temporal fusion of remotely sensed images with a rigorous statistical basis that enables to efficiently handle uncertainties, it imposes no requirements on the number of input high resolution images, and it is suitable for heterogeneous landscapes. It makes use of the advantage of multivariate arguments in statistics to handle temporal dynamics in a more flexible way rather than just by linear regression. Experimental results demonstrate that the proposed method outperforms STARFM and ESTARFM, especially for heterogeneous landscapes. It produces surface reflectance highly correlated with those of the reference Landsat images.

3.3.1.4 Product-level fusion

To illustrate the fusion at the product-level, three cases of post-classification fusion are presented here.

To update built-up areas of the 2012 European HRL Imperviousness, large choice of images including IRS LISS-3, RE, SPOT-5 and IRS AWIFS time series are available through the ESA Data Warehouse (DWH). These latter are heterogeneous and particularly complex to process all in one as they have different spectral/spatial resolution and they have been acquired at different time, in different conditions. Lefebvre et al. (2013) propose a robust approach able to combine all DWH products. They perform a separate image classification based on these data and then combine of each classification probabilities using a data fusion technique. The classification step is based on a neural network algorithm and the fusion step is performed with the Dempster-Shafer Theory (DST). This technique relies on evidence theory, it combines multiple classifiers dealing with the imprecision and uncertainty. Results bring out the efficiency of the method to process large projects such as GIO HR Layer and to benefit from the large diversity and availability of the ESA DWH products.

A fusion of Landsat data and MODIS active fire detections product is performed by Boschetti et al. (2015) to map systematically burned areas at 30 m resolution. Spectral changes in time series of Landsat 30m data and temporally and spatially near-coincident daily 1 km MODIS active fire detections are used as separate sources of evidence for the occurrence of fire. A multistage mapping approach is used with an initial per-pixel change detection based on spectral rule-based pre-classification of Landsat 30m time series to identify candidate burned areas. The candidate burned area objects are then either retained or discarded by comparison with contemporaneous MODIS active fire detections, and an object-oriented fusion of the candidate with the MODIS product is performed.

It is a common case that several and partially conflicting land cover products are available at the same time over a same area, where each product suffers from specific limitations and lack of accuracy. In order to take advantage of the best features of each product while at the same time attenuating their

respective weaknesses, Gengler and Bogaert (2018) propose a methodology that allows the user to combine these products together based on a general framework involving maximum entropy/minimum divergence principles, BDF and Bayesian updating. First, information brought by each land cover product is coded in terms of inequality constraints so that a first estimation of their quality can be computed based on a maximum entropy/minimum divergence principle. Information from these various land cover products can then be fused afterwards in a Bayesian framework, leading to a single map with an associated measure of uncertainty. Finally, it is shown how the additional information brought by control data can help improving this fused map through a Bayesian updating procedure.

3.3.2 Spectral and textural time series metrics/variables

The detection of changes in land use and the monitoring of seasonal dynamics can be hampered by various physical effects that affect the signal of the sensor.

Several issues can be mentioned, with varying impacts on the time series building. At the level of the sensor itself, saturation and non-linear response can occur during the capture of the digital count. This digital count for each pixel is also known to be permanently affected by the drift of the radiometric calibration – a familiar problem caused by the slow alteration of the sensor spectral capacities, subjected the short-wave radiation, that carries more energy and are prone to damage the material over time.

At the level of the surface, topographical effects, as detailed in the report D10.1a on WP 32, combined with surface reflectance effects and atmospheric distortion, cause false change detection. Those effects reveal themselves in the shape of shadows over relief that fluctuate from one image to the other, of sun glint over water bodies and wetlands, due to the brief matching of the sun zenithal angle and the one of the satellite, or of the presence of aerosols in the lowest layers of the atmosphere that causes light scattering and absorption. Reflectance on the surface can also be modified by the evolving optical properties of the background soil underneath vegetal cover.

All those factors can significantly produce variations in the raw data from one date to the other – even though a RTM has been applied to produce BOA images. Without in-situ data to support such models and provide measured parameters, the output of the model is still subject to small errors and uncertainties. This is why spectral and textural indices, some of them more or less resistant to such variations, can be used as a substitute for raw spectral band images. It should also be mention that multi-sensor approaches, by handling different spectral and spatial properties of various sensors, benefit from the use of such metrics.

3.3.2.1 Spectral variables

Many spectral indices have been defined in the past three decades. Some have been and are still widely used, such as the NDVI, while others have only been proposed as alternatives in the recent years and have not known the same exposure. In the following Table 3-1, main spectral indices are listed focusing on vegetation and built-up discrimination in order to explore their potential contribution to the evolution of Copernicus Land Services products and at the same time, favouring indices used in time series studies.

Table 3-1: List of spectral indices and their use for the creation of time series

Category	Indices	Used in Time Series Study
Vegetation Index	NDVI (Normalized Difference Vegetation Index)	✓
Vegetation Index	DVI (Difference Vegetation Index)	✓
Vegetation Index	RVI (Ratio Vegetation Index)	✓
Vegetation Index	IRECI (Inverted Red Edge Chlorophyll Index)	✓
Spectral Index	BI (Brightness Index)	Not found in time series study
Artificial Areas Index	NDBI (Normalized Difference Built-Up Index)	✓
Artificial Areas Index	UI (Urban Index)	Not found in time series study
Artificial Areas Index	BUI (Built-Up Index)	✓
Artificial Areas Index	IBI (Index-based Built-Up Index)	✓
Artificial Areas Index	NBI (New Built-Up Index)	✓
Artificial Areas Index	EBBI (Enhanced Built-Up and Bareness Index)	Not found in time series study
Artificial Areas Index	NBUI (New Built-Up Index)	✓
Hydric Stress Index	NDWI (Normalized Difference Water Index)	✓
Hydric Stress Index	MNDWI (Modified Normalized Difference Water Index)	✓
Hydric Stress Index	MSI (Moisture Stress Index)	✓
Soil Influence Index	PVI (Perpendicular Vegetation Index)	Not found in time series study
Soil Influence Index	SAVI (Soil-Adjusted Vegetation Index)	✓
Soil Influence Index	TSAVI (Transformed Soil-Adjusted Vegetation Index)	✓
Soil Influence Index	MSAVI (Modified Soil-Adjusted Vegetation Index)	✓

Vegetation Index	NDMIR (Normalized Difference Middle Infrared Index)	✓
Vegetation Index	NDRB (Normalized Difference Red Blue)	✓
Vegetation Index	NDGB (Normalized Difference Green Blue)	✓
Biophysical Index	LAI (Leaf Area Index)	✓
Soil and Atmosphere Effects Index	EVI (Enhanced Vegetation Index)	✓
Atmosphere Effects Index	ARVI (Atmospherically Resistant Vegetation Index)	✓
Atmosphere Effects Index	GEMI (Global Environment Monitoring Index)	✓
Vegetation Index	TDVI (Transformed Difference Vegetation Index or TDVI)	✓
Biophysical Index	FCover	✓
Biophysical Index	fAPAR	✓

Normalized Difference Vegetation Index or NDVI

Healthy plants are mainly green, thus absorbing sun radiation in the visible spectrum region called photosynthetically active radiation (PAR), which contains the perfect amount of energy to induce a photosynthesis reaction. Ultra-violet light carries too much energy, risking to damage DNA bonds. On the other side of the visible spectrum, infra-red light does not bring much energy to the electrons, and cannot be used as a source for photosynthesis. This is why plant reflects most of the IR wavelengths, while appearing dark in those bands - which is known as the 'red edge' effect.

The "Normalized Difference Vegetation Index" (Rouse Jr. et al., 1974; Tucker, 1979) is used as an indicator to monitor vegetation health, and can be used as a proxy for photosynthetic activity and primary production from vegetation biomass. It is calculated as the difference in the reflectance between those two spectral regions, normalized by the sum of the reflectance measurements:

$$NDVI = \frac{\rho_{NIR} - \rho_{Red}}{\rho_{NIR} + \rho_{Red}}$$

It is then expected for the NDVI to vary between -1 and 1, where:

- dense vegetation canopy exhibits values between 0.9 and 0.6;
- shrubs, grasslands or senescent crops give smaller values, between 0.5 and 0.2;
- soils, such as barren rocks, sand or snow, are characterized by small positive values, usually between 0.1 and 0.2;
- deep water and clouds yield negative values.

Since the clouds exhibit NDVI values below zero, the NDVI can be easily used as a cloud screening tool. This index is one of the oldest and most used means to map vegetation (or non-vegetation) presence on the ground.

The first limitation of the NDVI lays in the fact that by mathematical construction, it carries less information than both spectral channels used to compute its value. In particular, this design, with its compression of the high ratio values, is linked to the well-known and problematic saturation of the NDVI for dense canopies, which always leads to an underestimation of the green biomass for strong foliage density (Wang et al., 2005). Several other factors have been pointed as responsible in part for this loss of information, such as the width of the red band. The non-linearity of such a ratio also results in a non-linear relation with other vegetation indices, directly linked to the amount of vegetation present in the area of interest (AOI), among which, the fAPAR or the LAI are found.

The NDVI is also known to be sensitive at various degrees to the atmospheric effects, in particular to the presence of aerosols and water vapour, producing a degradation of contrast between the two spectral channels, but also to the conditions of observation, for example the absorption and the scattering occurring along the atmospheric path. The difference between the spectral response of two sensors yields different values of the NDVI over the same AOI, at the exact same date, making it harder to compare time series. However, the creation of composite images of NDVI is able to improve the resulting time series, with the minimization of anisotropic effects.

Several elements on the ground can degrade the interpretation of the NDVI. The inclination of the leaves modifies the BRDF and thus the ratio – the flatter the leaves, the stronger the signal of the NDVI, while their shadows artificially decrease its value. The soil underneath the foliage, depending on its brightness, its colour and its degree of moisture, or even the distribution of greenness on it (i.e. the same amount of vegetation covering the ground, but disposed in a different fashion) can have a tremendous impact on the NDVI values.

The NDVI is still widely used to qualitatively detect the presence of vegetation; however, the derivation of biophysical parameters can be hampered by those previously listed inter-dependences.

Difference Vegetation Index or DVI

The DVI (Richardson & Wiegand, 1977) was proposed before the NDVI and, as its name indicates, it is only the difference characterizing the red edge, without normalization. It is also known as the Environment Vegetation Index (EVI). It can be calculated with:

$$DVI = \rho_{NIR} - \rho_{Red}$$

Even though the DVI is not a normalized quantity, once directional effects are corrected (using in particular bidirectional anisotropy standard shapes and reflectance correction) and for water vapour absorption, the DVI is more robust than NDVI to atmospheric effects and noise in general (Bacour et al., 2006).

However, the DVI still exhibits similar limitations to the NDVI ones, due to its close mathematical construction. In fact, the DVI remains sensitive to several key parameters, in particular, the presence of aerosol in the atmosphere, and the resulting scattering of the radiation. The geometry of the observation, mainly presenting a solar zenithal angle higher than 60° can lead to disparaging results – this is specifically an issue for old sensors, which are subject to orbital drift effects.

Overall, it should be noted that like the NDVI, the DVI cannot be used as a tool to quantitatively estimate the state of vegetation, as it saturates when the vegetation is dense.

Ratio Vegetation Index or RVI

Also called Simple Ratio (SR), the ratio vegetation index (Jordan, 1969) is defined by:

$$RVI = \frac{\rho_{NIR}}{\rho_{Red}} \text{ or } RVI = \frac{\rho_{NIR}}{\rho_{Vis}}$$

where the red channel is replaced by the visible channel if it is not available. RVI for bare soils are near 1, its value increases as the amount of green vegetation in an AOI. The ratio is not bound and can increase far beyond 1.

By design, the RVI is less sensitive to the topographical and atmospheric effects when the vegetation coverage is dense; it is due to the fact that the equation eliminates irradiance and transmittance values in both channels. Unlike the NDVI and the DVI, a good correlation exists between the plant biomass present in the AOI and the RVI values.

Yet those improvements remain limited. Sensitivity to the spectral contribution of the soil, to the geometry of the observation, in particular the sun illumination angle, cannot be eliminated from the computation of the RVI. When the vegetation is sparse (i.e. covering less than 50% of the observed AOI), the RVI also needs to be atmospherically corrected.

Inverted Red Edge Chlorophyll Index or IRECI

The IRECI was introduced by (Frampton et al., 2013) to evaluate the capability of the Sentinel-2 sensor for the estimation of canopy chlorophyll content. It utilizes the maximum and minimum vegetation reflectances in the RED EDGE 3 (proposed NDVI band adjusted to Sentinel-2 wavelength specifications) and RED bands and the leaf chlorophyll concentration indicative RED EDGE slope. The incorporation of the Red Edge bands also limits the effects of saturation. Although not the initial aim of the development, the IRECI index showed a strong linear correlation with the biophysical Leaf Area Index (LAI) parameter.

$$\frac{\rho_{Red\ Edge\ 3} - \rho_{Red}}{\rho_{Red\ Edge\ 1} / \rho_{Red\ Edge\ 2}}$$

Brightness Index

The brightness Index (BI) can be expressed as (Mathieu et al., 1998):

$$BI = \sqrt{\frac{\rho_{Red} + \rho_{Green} + \rho_{Blue}}{3}}$$

which is a measure of the average reflectance magnitude in the visible bands, used to quantify the soil color effect.

Normalized Difference Built-Up Index or NDBI

The “Normalized Difference Built-Up Index” (Zha et al., 2003) is defined by the equation:

$$NDBI = \frac{\rho_{SWIR} - \rho_{NIR}}{\rho_{SWIR} + \rho_{NIR}}$$

This index highlights urban areas, where the SWIR radiations are more reflected than the NIR ones. It has been originally developed for Landsat TM bands 4 and 5 and it will work with any multi-spectral instrument with a NIR band between 0.76 - 0.9 µm and a SWIR band between 1.55 – 1.75 µm. The NDBI

determination does not rely on seasonality consideration and should not be impacted by the date of the image; however, it remains best to put an emphasis on image acquired at times when the vegetation cover is at its peak, like for any vegetation indices. The use of a different spectral channel, the SWIR band, in the equation of the NDBI makes it independent yet complementary to the NDVI, and they both can be used together.

The NDBI does not distinguish the different parts constituting the urban tissue, for example, residential land cover will exhibit the same NDBI as highly industrial areas. This is why the NDBI is mainly used to map wide urban land cover, requiring few details. It should also be noted that the NDBI confuses barren lands, such as sandy beaches, agricultural areas subjected to drought, due to the loss of moisture in the soil, with urban zones. This confusion between beaches and urban areas can be circumvented by assessing the closeness to water bodies; however, peripheral urban zones mixed with barren soils will be less simply discriminated using this index.

Urban Index or UI

The Urban Index (Kawamura et al., 1996) is defined as:

$$UI = \left(\frac{\rho_{SWIR_2} - \rho_{NIR}}{\rho_{SWIR_2} + \rho_{NIR}} + 1 \right) * 100$$

where ρ_{SWIR_2} is the SWIR band with wavelengths ranging from $2.08 \mu m$ and $2.35 \mu m$, matching the band 7 of Landsat TM. The UI exploits an observed inverse relation between the brightness of built-up lands in the NIR and SWIR bands.

While on one hand, the UI cannot distinguish between barren lands and built-up areas, this can be improved by combining it with an automatic segmentation method.

Built-Up Index or BUI

The Built-Up Index, in order to separate the barren lands from the urban sprawl (Kaimaris & Patias, 2016), is defined by:

$$BUI = \frac{2 * ((\rho_{Red} * \rho_{SWIR_2}) - (\rho_{SWIR_1} * \rho_{SWIR_1}))}{(\rho_{Red} + \rho_{SWIR_1}) * (\rho_{SWIR_1} + \rho_{SWIR_2})}$$

where SWIR_1 matches the band 5 of Landsat TM, which ranges from $1.55 \mu m$ to $1.75 \mu m$, SWIR_2 tallies with the band 7, from $2.09 \mu m$ to $2.35 \mu m$.

In their article, Kaimaris and Patias showed that the built-up index identifies areas without constructions with a better accuracy than NBI, UI, NDBI, IBI and EBBI, due to the fact that the CART does not take into account the contribution of the spectral band in the near infrared, which leads to a reduced overall accuracy to identify constructions. However, the test has only been realised at the scale of a city.

Index-based Built-Up Index or IBI

The Index-based Built-Up Index (Xu, 2008) is the first urban index based on other indices results, rather than the raw data of the images spectral bands. It is defined as:

$$IBI = \frac{(NDBI - (SAVI + MNDWI)/2)}{(NDBI + (SAVI + MNDWI)/2)} = \frac{\frac{2 * \rho_{SWIR}}{(\rho_{SWIR} + \rho_{NIR})} - \left[\frac{\rho_{NIR}}{(\rho_{NIR} + \rho_{Red})} + \frac{\rho_{Green}}{(\rho_{Green} + \rho_{SWIR})} \right]}{\frac{2 * \rho_{SWIR}}{(\rho_{SWIR} + \rho_{NIR})} + \left[\frac{\rho_{NIR}}{(\rho_{NIR} + \rho_{Red})} + \frac{\rho_{Green}}{(\rho_{Green} + \rho_{SWIR})} \right]}$$

then later refined (Ray, 1994) as:

$$IBI = \begin{cases} \frac{(NDBI - (SAVI + MNDWI)/2)}{(NDBI + (SAVI + MNDWI)/2)}, & \text{if the plant cover is } < 30\% \\ \frac{(NDBI - (NDVI + MNDWI)/2)}{(NDBI + (NDVI + MNDWI)/2)}, & \text{if the plant cover is } > 30\% \end{cases}$$

The three indices represent the three main components of urban environments: vegetation, water and built-up land. The values range from -1 to 1, where null or negative values are generated by background noise, such as water and vegetation.

The IBI is constructed to suppress background noises and to clearly separate the diverse land cover or land use classes, in particular to detect asphalt and concrete surfaces. Yet compared to simple indices such as the NDVI, the IBI requires either a complex computation composed of four spectral bands or the computation of four different indices.

New Built-Up Index or NBI

The Built-Up Index (Jieli et al., 2010) is defined by:

$$NBI = \frac{2 * (\rho_{Red} * \rho_{SWIR_1mu})}{\rho_{NIR}}$$

It should be noted that the NBI is only able to highlight built-up areas, not to separate water bodies or forest from mixed agriculture. Moreover, this index is not a dimensionless quantity, and therefore is dependent on the sensor – time series of maps generated with it, but issued from different satellites cannot be compared between each other.

Enhanced Built-Up and Bareness Index or EBBI

The Enhanced Built-Up and Bareness Index (As-Syakur et al., 2012) is defined by:

$$EBBI = \frac{\rho_{SWIR_1mu} - \rho_{NIR}}{10 \sqrt{\rho_{SWIR_1mu} - \rho_{TIR}}}$$

It relies on 3 channels, in order to highlight contrast reflection range and absorption in built-up and bare land areas. The Thermal InfraRed (TIR) wavelengths are used to map high and low levels of albedo in urban areas. The high emissivity in urban areas is caused by the type of material found in those, while the emissivity of bare soil is determined by the degree of moisture and the presence of mineral constituents.

The positive values are associated with built-up and barren land pixels, while the presence of vegetation generates negative values, roughly varying between -1 and 1. The TIR channel is also sensitive to the higher temperature radiation emitted by the urban areas.

The EBBI has been specially constructed to distinguish between barren soils and built-up lands. Based on the work of As-Syakur et al. (2012), it shows an increased accuracy to determine the percentage of surface covered by built-up structures, but its relative accuracy may be lower than other indices, specifically designed to target only one type of land covers, which is to be expected in highly heterogeneous landscapes. This index also has the advantage to eliminate artefacts produced by the shadows or the water bodies' presence.

New Built-Up Index or NBUI

The New Built-Up Index (Sinha et al., 2016) is defined by the combination of 3 other indices:

$$NBUI = EBBI - (SAVI + MNDWI)$$

$$NBUI = \frac{\rho_{SWIR_1mu} - \rho_{NIR}}{10 \sqrt{\rho_{SWIR_1mu} - \rho_{TIR}}} - \left(+ \frac{\rho_{Green} - \rho_{SWIR}}{\rho_{Green} + \rho_{SWIR}} \right)$$

The use of EBBI highlights the contrast reflection between built-up and barren lands, while the second part uses SAVI to signal the presence of vegetation, instead of NDVI, which remains less effective in an area with low plant cover. The final part, the MNDWI, is used to map the presence of water. This leads to positive values for built-up and barren lands, while water and vegetation yield negative values. This index has shown a better accuracy to map urban areas than NDBI or UI, taken alone, as demonstrated in the works of Sinha et al. (2016).

Normalized Difference Water Index or NDWI

The “Normalized Difference Water Index” (Gao, 1996) is defined as the ratio

$$NDWI = \frac{\rho_{NIR} - \rho_{SWIR}}{\rho_{NIR} + \rho_{SWIR}}$$

where ρ is the radiance in reflectance unit. Both wavelengths are localized in the part of the spectrum reflected by vegetation canopies. The NIR channel is linked to a negligible absorption of light by the water content present in the vegetal, while the SWIR channel present a weak liquid absorption. The NDWI is therefore sensitive to slight changes in the liquid water absorbed by vegetation canopies, giving an indication on the vegetation water stress.

The NDWI is the opposite of the NDBI in theory, but other set of bands in the SWIR and NIR are often used. The NDWI is therefore also independent yet complementary to the NDVI. Compared to the latter, the NDWI is less sensitive to the atmospheric effects, in particular to the presence of water vapour in the atmospheric column. While the NDVI is linked to vegetation greenness and the presence of chlorophyll in the plants, it is not directly to the quantity of water in them, contrary to NDWI. The soil background has a non-negligible effect on the values of this index when the vegetal cover at the surface is only partial. Drought and water stress are not the only factors responsible for land cover changes, pest and diseases can alter the vegetal cover; the NDWI should be used with other vegetation indices.

Modified Normalized Difference Water Index or MNDWI

Another derived index is the “Modified Normalized Difference Water Index” (MNDWI) (Xu, 2006) which focuses on extracting water presence from background dominated by built-up land:

$$MNDWI = \frac{\rho_{Green} - \rho_{SWIR}}{\rho_{Green} + \rho_{SWIR}}$$

where ρ_{Green} is the reflectance of a green band between 0.5 - 0.6 μm and ρ_{SWIR} a band between 1.55 – 1.75 μm . The water bodies are expected to be more finely delineated by this index, using a proper thresholding value – thanks to an improved discrimination between open surface water and the noise emerging from the built-up areas, the moisture present in the vegetation and soil.

Moisture Stress Index or MSI

In order to track the amount of water in the vegetation, and in particular the leaves, it is possible to switch the red band for a band in the mid-infrared. Based on the model of the RVI, a new index (Hunt & Rock, 1989) can be defined as:

$$MSI = \frac{\rho_{MIR}}{\rho_{NIR}}$$

This index is used to monitor canopy stress, to predict productivity of crop fields and to study biophysical modeling. The interpretation of the MSI is inverted, compared to the other water indices: the high values indicate a greater water stress in the foliage. The variation ranges from 0 to 3, and common values for a healthy green vegetation is comprised between 0 and 2.

Perpendicular Vegetation Index or PVI

In order to take into account the influence of the soil underneath the vegetation, this index is computed in the feature space between the NIR band and the red one (Richardson & Wiegand, 1977). Each pixel of an image can be placed in a graph called feature space graph using its radiation reflected luminance in the red band and its radiation reflected luminance in the NIR band as coordinates. Using this visualization in the red, NIR 2D space, it is possible to spot isolated groups of pixels that may be related.

The soil line is the line defined by a slash called the soil brighten line, and the PVI is taken equal to the perpendicular distance from this line to the point representing the pixel. Each pixel of equal vegetation density cover is supposed to be found along parallel lines to this soil line, which are called vegetation isolines. The greater the distance to the soil line, the greater the vegetation biomass. The PVI can then be computed from the equation:

$$PVI = \sqrt{(\rho_{soil} - \rho_{veg})_{Red}^2 + (\rho_{soil} - \rho_{veg})_{NIR}^2}$$

where ρ_{soil} is the soil reflectance and ρ_{veg} is the vegetation reflectivity.

The main advantage of the PVI lays in its ability to filter out the undesired influence of the soil background in an effective manner; moreover, it exhibits also less sensitivity to the atmospheric effects. This is why the PVI is often preferred to the NDVI for the inversion of surface vegetation parameter (grass yield, chlorophyll content) or the computation of the LAI.

Nonetheless, the PVI remains sensitive to soil brightness and soil reflectivity, in particular in the presence of sparse vegetation coverage, and therefore needs to be adjusted for each kind of couple (soil type, percentage of vegetation coverage).

Soil-Adjusted Vegetation Index or SAVI

In order to improve even more the way soil is being considered in the PVI, Huete (1988) proposed to include the nature of the background as a parameter, leading to:

$$SAVI = \frac{(\rho_{NIR} - \rho_{Red})(1 + L)}{\rho_{NIR} + \rho_{Red} + L}$$

where L is called the soil conditioning index. The values of L are fixed according to the specific environmental conditions, from 1 to 0. When the vegetation cover is dense, in the case of large canopies mainly, L has a value near 0.25, while for areas devoid of green vegetation, L is set to 1. Under most environmental conditions, L is close to 0.5 and when it is near 0, the value of SAVI nears the one of the NDVI. SAVI values range from -1 to 1: the lower this value, the lower the amount of green vegetation.

One of the most key features of the SAVI lies in its ability to be more robust than the NDVI without requiring atmospheric corrections, and, as a consequence, to be even more accurate with the use of those corrections. On the other hand, this accuracy depends upon the specification of a soil brightness correction factor, which is a function of the kind of land cover present in the image – thus changing for each considered landscape.

Transformed Soil-Adjusted Vegetation Index or TSAVI

An improvement of the SAVI, called TSAVI, has been constructed (Baret et al., 1989) using the determination of the soil line for the considered sensor, modeled by a slope a and an intercept of the soil line b :

$$TSAVI = \frac{a * (\rho_{NIR} - a * \rho_{Red} - b)}{\rho_{NIR} + \rho_{Red} - a * b + 0.08 * (1 + a^2)}$$

where the coefficient value 0.08 has been adjusted to minimize soil effects.

The TSAVI uses the slope a and the intercept of the soil line b instead of an arbitrary parameter like the soil conditioning index L , which is an advantage to better retrieve information, but also a limitation, as it needs a function depending on the kind of land cover present in the image.

Modified Soil-Adjusted Vegetation Index or MSAVI

Another improvement proposed for the SAVI is the MSAVI, based on other local indices (Qi et al., 1994), rendering the parameter L dynamically adjusted using the image data:

$$MSAVI = \frac{(\rho_{NIR} - \rho_{Red})(1+L)}{\rho_{NIR} + \rho_{Red} + L}, \text{ with } L = 1 - 2 * a * NDVI * WDVI$$

where a is the slope of the soil line and $WDVI = \rho_{NIR} - a * \rho_{Red}$ is the Weighted Difference Vegetation of Clevers, functionally equivalent to the PVI. To correct the soil brightness, the MSAVI loses overall sensitivity to changes in vegetation cover, unlike NDVI, which thus remains a more appropriate tool to detect changes. It should also be added that the MSAVI is more sensitive to the atmospheric conditions between different AOI and/or taken at different times.

Normalized Difference Middle Infrared Index or NDMIR

The Normalized Difference Middle Infrared Index (NDMIR) has been originally proposed by Lu et al. (2004) for Landsat TM data and is a normalised difference of both middle infrared bands:

$$NDMIR = \frac{\rho_{MIR1} - \rho_{MIR2}}{\rho_{MIR1} + \rho_{MIR2}}$$

Thus, it is sensitive to vegetation moisture. However, change in forest volume has been identified in many studies of being revealed best by middle infrared wavelengths and also Lu et al. (2004) showed that the NDMIR significantly correlated with forest stand parameters.

Normalized Difference Red Blue or NDRB

The Normalized Difference Red Blue Index (Zhou et al., 2014) has been designed based on the red and blue bands of Landsat-8 OLI data:

$$NDRB = \frac{\rho_{RED} - \rho_{BLUE}}{\rho_{RED} + \rho_{BLUE}}$$

It has been introduced to better discriminate red/grey-roofed built-up from bare land areas (Zhou et al., 2014).

Normalized Difference Green Blue or NDGB

The Normalized Difference Green Blue Index (Zhou et al., 2014) has been designed based on the red and blue bands of Landsat-8 OLI data:

$$NDGB = \frac{\rho_{GREEN} - \rho_{BLUE}}{\rho_{GREEN} + \rho_{BLUE}}$$

Similar to the NDRB, the NDGB has been introduced to better extract the blue-roofed built-up areas and part of the red/grey-roofed built-up areas (Zhou et al., 2014). Combined with the NDRB it was used to discriminate built-up areas and bare soil and achieved better results than with the standard NDBI approach.

Leaf Area Index or LAI

The “Leaf Area Index” (Turner et al., 1999) is used to characterize plant canopies and determine the size of the interface for the exchange of energy (including mainly radiation) and mass between the canopy and the atmosphere. It is defined as the green leaf area per unit of ground surface for broadleaf trees, and concerning conifers, there have been several proposed definitions:

- Either the total needle surface per unit of ground surface area, divided by two;
- Either the projected needle surface per unit of ground surface area;
- Or the total needle surface per unit of ground surface area.

The leaf area index can range from 0 for barren lands to 10, for dense canopies and is used to estimate leaves cover and to forecast crop yield, but also examine relationships between environmental stress factors and forest insect damages. It remains strongly non-linear with reflectance, scale-dependent and not accessible directly from remote sensing observations, which are sensitive to the ‘effective’ LAI, a fraction of the ‘true’ LAI. The LAI can theoretically be retrieved with physical models, but some assumptions on the distribution of leaves have to be made, and cannot be applied for all types of vegetation.

One of the ways to determine the LAI in-situ involves the measurements of a foliage sample – which is a destructive method. The true LAI is difficult to acquire from remote sensing images, for numerous reasons, e.g. the effect of branches and stems blocking the light – and the validation of this product using in-situ data can prove to be difficult.

Enhanced Vegetation Index or EVI

The “Enhanced Vegetation Index” (Liu & Huete, 1995) is defined by the following equation:

$$EVI = Gain * \frac{(\rho_{NIR} - \rho_{Red})}{(\rho_{NIR} + C_1 * \rho_{Red} - C_2 * \rho_{Blue} + L)}$$

where the numerical parameters *Gain*, C_1 , C_2 - both weights related to the aerosol conditions in the blue and red bands - and L - a canopy background adjustment term - need to be adapted for each sensor and each situation. The main feature of the EVI is to incorporate background corrective term as well as atmospheric resistance concepts, therefore ρ is the “apparent” reflectance, at the top of the atmosphere, that requires no further calibration – which means in return that C_1 and C_2 depend on the atmospheric conditions, while L depends on the kind of vegetation present on the image – thus forcing the EVI to require an empirical tuning for each AOI.

Atmospherically Resistant Vegetation Index or ARVI

This index is based on the knowledge that the red band is significantly impacted by the atmospheric effects, more than the NIR band (Kaufman & Tanre, 1992). Thus, the red band value is replaced by a difference between the blue and the red bands value, taking into account the (Rayleigh) molecular scattering and gaseous absorption for ozone corrections. The ARVI is expressed as:

$$ARVI = \frac{\rho_{NIR} - \rho_{RB}}{\rho_{NIR} + \rho_{RB}}, \text{ with } \rho_{RB} = \rho_{Red} - \gamma * (\rho_{Red} - \rho_{Blue})$$

where γ depends on the aerosol type – which can be set to 1 if the aerosol model is unknown, presenting thus no change with the NDVI.

The ARVI is based on a reformulation of the NDVI designed to eliminate the effects of atmospheric aerosols and the ozone absorption, and this improved version of the NDVI, with this atmospheric resistance concept, can be incorporated into other indices, such as SAVI, to form a soil and atmospherically resistant vegetation index or SARVI; however, soil and atmosphere influence are interactive, and the removal of one source of noise increased the presence of the other. The main constraint of the ARVI lays in the fact that it should be computed with an aerosol model, and without one, it remains no better than NDVI. Therefore, one needs in-situ data on the actual atmospheric conditions, varying for each given time of the temporal series and each considered AOI.

Global Environment Monitoring Index or GEMI

In order to minimize the influence of atmosphere on the computation of index, such as the Rayleigh scattering, the GEMI (Pinty & Verstraete, 1992) is a non-linear index, defined as:

$$GEMI = \eta * (1 - 0.25 * \eta) - \frac{\rho_{Red} - 0.25}{1 - \rho_{Red}}, \text{ with } \eta = \frac{2(\rho_{NIR}^2 + \rho_{Red}^2) + 1.5 \rho_{NIR} + 0.5 \rho_{Red}}{\rho_{NIR} + \rho_{Red} + 0.5}$$

which varies from 0 to 1 over continental areas.

The GEMI, like the NDVI, involves only two spectral channels to be computed, and has been designed to be resistant to atmospheric conditions, leading to an almost linear relationship between the GEMI computed without atmospheric corrections, computed at the top of the atmosphere, and the pre-processed GEMI, obtained at the bottom of the atmosphere. On a given AOI, the GEMI has the disadvantage to be highly sensitive to soil noise, and is unable to deal with variations in soil reflectance – therefore being unsuitable for the creation of time series over arid regions.

Transformed Difference Vegetation Index or TDVI

The Transformed Difference Vegetation Index (Bannari et al., 2002) has been theorized to be an improvement of the NDVI and the SAVI, by having a linear function of the vegetal canopy, while being resistant to the optical properties of the bare soil:

$$TDVI = \sqrt{0.5 + NDVI} = \sqrt{0.5 + \frac{\rho_{NIR} - \rho_{Red}}{\rho_{NIR} + \rho_{Red}}}$$

The TDVI does not saturate like NDVI and SAVI for high values and exhibit a linear behaviour as function of the amount of vegetation cover. However, like the NDVI or the SAVI, the TDVI requires calibrated images to perform better than both indices, in particular to avoid the impact of atmospheric effects.

Fractional Cover or FCover

FCover is the estimated fraction of green vegetation that covers the soil, as seen from the nadir (Carlson & Ripley, 1997). It used to quantify the surface occupied by vegetation, giving an indication of the crop growth rate. Several methods can be employed to determine its value for a given image, among which:

- Conventional classification, using supervised or unsupervised algorithms
- Linear modelling, correlating field-measured fractional cover with sensor reflectance bands or vegetation indices
- Physical models, that simulates how the light energy is reflected or absorbed by the different surfaces and can derive an estimation of the FCover, based on the LAI and other structural canopy variables

When the FCover is numerically computed using physical models, its determination requires a precise description and/or group of assumptions on the BRDF: it is mostly done on high-resolution images, over small AOI.

Fraction of Absorbed Photosynthetically Active Radiation or fAPAR

The fAPAR is the fraction of photosynthetically active radiation absorbed by the green parts of the canopy. It depends on the canopy structure, on the vegetation element optical properties and the illumination conditions. The major methods to generate the fAPAR are mainly simulations, such as linear modeling interpolation or physical models.

The fAPAR excludes the fraction of incident PAR that is reflected by the leaves and absorbed by the soil, as well as the fraction directly absorbed by the soil. It remains difficult to measure directly, and is usually computed by numerical radiative transfer models, like the LAI and the FCover, for given assumptions on the canopy structure.

The fAPAR values prove to be relatively linear related to the reflectance values, but depend on the chosen scale, which can be an issue as the fAPAR is routinely used as a key variable to forecast crop yield (Prince & Goward, 1995) and to monitor forest health. Estimations of the fAPAR are excessively sensitive to the presence of snow in the background.

Other indices

Other indices have been defined and used in a less publicized way:

- Green biomass
- Green Atmospherically Resistant Index (GARI)
- Green Difference Vegetation Index (GDVI)
- Green Normalized Difference Vegetation Index (GNDVI)
- Green Ratio Vegetation Index (GRVI)
- Green Vegetation Index (GVI)
- Infrared Percentage Vegetation Index (IPVI)

- Modified Non-Linear Index (MNLI)
- Modified Simple Ratio (MSR)
- Non-Linear Index (NLI)
- Normalized Difference Mud Index (NDMI)
- Normalized Difference Snow Index (NDSI)
- Optimized Soil Adjusted Vegetation Index (OSAVI)
- Renormalized Difference Vegetation Index (RDVI)
- Sum Green Index (SGI)
- Visible Atmospherically Resistant Index (VARI)

The use of those indices may eventually be explored in more detail in the second phase, if the selected indices of the first phase reveal themselves unsuitable for characterizing and quantifying the results of the fusion between Sentinel-2 and Sentinel-3 optical time series.

Preliminary conclusion

Despite presenting some drawbacks, the NDVI is still widely in use, largely because of its computation in well-calibrated enduring time-series, like the NOAA-AVHRR data set or the Landsat one, spanning over several decades, thus easing the analysis of LC/LU evolution. It remains an inescapable quantity in the creation of time series, not only to classify new time series of images, but also to compare the results to other studies. The same can be said for the NDBI and the BI, and it is proposed here to use the first two indices first jointly to characterize the imperviousness layer. Other interesting indices have also been tested to better characterize the LC/LU and in particular the forest and agriculture. The NDMIR complements the NDVI to better distinguish vegetation over low water content, whose spectral response can be mistaken as urban areas while using the NDVI. The MNDWI is of help to better discriminate the water bodies and wetlands, and is used when the NDWI accuracy is deemed not sufficient. The IRECI, specifically designed to take advantage of the red edge bands available in S-2 data, can be used to evaluate the canopy chlorophyll content, while being linked to the LAI. The NDRB and NDGB are used to enhance the discrimination between urban areas and bare soils or bare rocks.

Based on the results of this first phase, tuning and adjustment in those choices will be made in the second phase and further indices will be brought in if need be. The NDVI looks relevant, but depending on the specific layer, it seems that it will always be necessary to complement it with a particular set of other indices to improve the separability of classes and enhance classification results, which are being discussed in the reports for WP33 and 34.

3.3.2.2 Textural techniques

Spectral indices allow the exploration of spectral correlation, but without further analysis, the spatial correlation existing between adjacent pixels is clearly omitted. Several techniques, quantifying either the overall spatial repartition of pixel intensity (the so-called spatial-frequency index) or the special correlation between a distinctive group of pixels (designated as textural indices), can be listed, as seen in the Table 3-2.

Table 3-2: List of textural indices and their use in the creation of time series.

Category	Indices	Used in Time Series Study
Textural Index	GLCM/GLCH	✓
Textural Index	PanTex	✓

Spatial-frequency Index	FT	V
Spatial-frequency Index	WT	V

Co-occurrence matrix

The computation of co-occurrence matrices is a widely used method to extract texture features, where an image texture is defined as an arrangement of intensities (a pattern) that can be repetitively found at various scales in an image. This method is able to capture the similarity in the gray tones of those patterns and the spatial relations between them.

A co-occurrence matrix or distribution (Haralick et al., 1973) is a matrix C defined over an image to be the descriptor of the state of two pixels simultaneously considered, therefore characterized by a distance d and an orientation θ or an offset in each direction, for example $(\Delta x, \Delta y)$. For an image I of N pixels, of size $n * m$, the co-occurrence matrix C can be written as:

$$C = \begin{bmatrix} p(1,1) & p(1,2) & p(1,3) & \dots & p(1,N) \\ p(2,1) & p(2,2) & p(2,3) & \dots & p(2,N) \\ p(i,1) & p(i,2) & p(i,3) & \dots & p(3,N) \\ \vdots & & \ddots & & \vdots \\ p(N,1) & p(N,2) & p(N,3) & \dots & p(N,N) \end{bmatrix}$$

where (i, j) are pixel values and $I(x, y)$ is the value of the pixel at (x, y) . Several texture measures can be derived from this matrix:

- The uniformity or energy:

$$UNI = \sum_{i=0}^{N-1} \sum_{j=0}^{N-1} p^2(i, j)$$

- The contrast:

$$CONT = \sum_{i=0}^{N-1} \sum_{j=0}^{N-1} |i - j|^k * p(i, j)^2$$

- The maximum probability:

$$MAX = \max_{i,j} p(i, j)$$

- The correlation:

$$CORR = \sum_{i=0}^{N-1} \sum_{j=0}^{N-1} \left[\frac{(i - \mu) * (j - \mu) * p(i, j)}{\sigma^2} \right]$$

- The entropy:

$$ENT = \sum_{i=0}^{N-1} \sum_{j=0}^{N-1} p(i, j) * \log(p(i, j))$$

- The inverse difference moment:

$$INV = \sum_{i=0}^{N-1} \sum_{\substack{j=0 \\ j \neq i}}^{N-1} \frac{p(i,j)^2}{|i-j|^k}$$

- The angular second moment:

$$ASM = \sum_{i=0}^{N-1} \sum_{j=0}^{N-1} p(i,j)^2$$

- The homogeneity:

$$HOM = \sum_{i=0}^{N-1} \sum_{j=0}^{N-1} \left[\frac{p(i,j)}{1 + |i-j|} \right]$$

- The dissimilarity:

$$DISS = \sum_{i=0}^{N-1} \sum_{j=0}^{N-1} p(i,j) * |i-j|$$

Co-occurrence matrices are also referred to as gray-level co-occurrence matrices (GLCMs), as gray-level co-occurrence histograms (GLCHs), or as spatial dependencies matrices. The computation can be done in the entire image or in a reduced window for a particular analysis. The co-occurrence matrices are well adapted to describe natural textures, e.g., grassland or cultivated fields. Those matrices are widely used in remote sensing analysis in order to distinguish patterns resulting from anisotropy.

Nonetheless, their handling necessitates the set-up of multiple parameters such as the direction offset, the size of the analysis window or even the choice of one or several metrics described by (Haralick et al., 1973). Depending on the size of the analysis window, bigger or smaller patterns will be detected; the accuracy of the classification procedure thus strongly depending on the values of this particular parameter. Moreover, the temporal evolution of a local texture, based on its size, can be difficult to interpret.

PanTex

The procedure for the calculation of a texture-derived built-up presence index, shortened by PanTex (Pesaresi et al., 2008), is based on fuzzy rule-based composition of anisotropic measures derived from co-occurrence matrix applied to the image. Instead of using spectral signature produced by physical-chemical properties, the PanTex exploits stable structural traits producing local contrast, which can be enhanced by rotation-invariant anisotropic textural analysis based on GLCM measures.

The workflow of the processing chain can be summed up in the following steps:

- Pre-processing, which encompasses ortho-rectification and mosaicking
- Calculation of Built-Up Presence Index (computation of co-occurrence measure, like the contrast, for all the considered directions, integration of different directions in the fuzzy built-up area membership)
- Extraction of built-up areas polygon (calculation of the de-fuzzyfication threshold and polygon extraction)

- Layer production (visual interpretation, cross-checking)

There are numerous advantages in the selection of the PanTex index, compared to the general theory of the co-occurrence matrices, in order to study urban areas, among which can be found:

- A reduction of edge effects on non-built-up features;
- A robustness against seasonal changes, from multi-sensor images, or multi-scenes, i.e. images with various illumination, weather, atmospheric conditions;
- A robustness against image compression based on wavelet transformation;
- A robustness for various landscapes present in the scene;
- The use of panchromatic images instead of multi-spectral datasets;
- No need for calibration of the input data;
- No need for training data.

From the list of parameters needed to use the co-occurrence matrices alone, the PanTex leaves the user only one free parameter to set up, the value of the threshold applied to the built-up index continuum function to generate discrete polygons.

Fourier transforms

The Fourier transform \hat{f} is the representation of a temporal function f in the frequency space

$$\hat{f}(k) = \int_{-\infty}^{\infty} f(t) e^{-ikt} dt$$

where i is the imaginary number and k is the frequency. The transformation is reversible. For an image $I(x, y)$ of size $n * m$, the Fourier transform can be written as:

$$\hat{I}(k, l) = \frac{1}{NM} \sum_{x=0}^{N-1} \sum_{y=0}^{M-1} I(x, y) e^{-i2\pi(\frac{xk}{N} + \frac{yl}{M})}$$

All frequencies are represented, whichever their direction in the image is. A privileged direction for the studies is not needed to determine and isolate a given pattern, contrary to the previously mentioned indices like the GLCMs.

Yet, the Fourier transform is applied on the whole picture, and the frequency spectrum cannot spatially localize the characteristics of the texture; this can be eventually resolved by using a sliding window, but it therefore introduces the size of the window as another parameter to set up.

Wavelet transformation Analysis

The wavelet transform has been theorized by (Morlet et al., 1982a) and (Morlet et al., 1982a, 1982b) to study seismic activities. This approach has been reused in image processing (Mallat, 1989; Meyer, 1990). The continuous wavelet transform of a continuous signal f is written as:

$$\mathcal{F}(a, b) = \int_{-\infty}^{+\infty} f(t) \frac{1}{\sqrt{a}} \varphi^* \left(\frac{t-b}{a} \right) dt$$

where a is the scale factor that cannot be null, b is a real number called the translational value and $\varphi^*(t)$ is the complex conjugate of φ , which is a continuous function in the time domain as well as in the

frequency domain. This function, called a “mother wavelet”, is used to derive “daughter wavelets”, translated and scaled for different a and b parameters.

$\mathcal{F}(a, b)$ is the projection of $f(t)$ on the analysis function $\varphi^*(\frac{t-b}{a})$ which can be chosen among various wavelet types, such as the Morlet wavelet, the Mexican hat wavelet, the Haar wavelet, or the Hermitian wavelet. One can demonstrate that the family of functions defined by $\varphi_{j,m}(k) = 2^{-j/2} \varphi(2^{-j} * k - m)$ forms an orthonormal basis, which can therefore represent the whole signal without loss. An image I is represented in those basis functions as

$$I = \sum_m c_{j_0, m} * \varphi_{j_0, m}(k) + \sum_{j \leq j_0} \sum_m d_{j, m} * \psi_{j, m}$$

where the $c_{j_0, m}$ is the continuous component at the scale j_0 and $d_{j, m}$ are the detailed component (or high frequency component).

Other indices

Other indices have been defined based on those time-frequency analysis techniques:

- Fourier-based Textural Ordination (FOTO)
- Extended Attribute Profiles (EAPs)
- Grey-Level Difference Vector (GLDV)
- Higher-order local autocorrelation (HLAC) and Multi-Channel extension HLAC (MUCHLAC)
- Built-up Areas Saliency Index, based on the PanTex (BASI)

The use of PanTex is planned to be used in the second phase, and those other indices could be explored in further detail during this phase too.

Preliminary conclusion

For the imperviousness layer, in this first phase, the time series is created on change detection as detailed in the report for WP34, without using any textural index. Therefore, only spectral indices for characterizing the various layers are tested in this WP, and yet textural indices, such as the PanTex, which is already known to bring interesting results, will be discussed in the second phase, on imperviousness layer, and eventually on the forest and grassland layers.

3.4 Candidate interpolation and fusion approaches for benchmarking

In the following, the candidate methods for integration and fusion approaches to combine S-1, S-2 and S-3 data with regards to the envisaged evolution of Copernicus Land Services are presented.

3.4.1 Candidate approaches for integration of S-1/S-2 complementary information

Aim of the integration of S-1/S-2 data is to better describe the different physical interactions with the land surface, defining primarily different characteristics of the LC/LU objects, and thus improving the classification result. Optical multispectral data on the one side describe e.g., the leaf structure, pigmentation and moisture of vegetation, while SAR data on the other side describe their size, density and dielectric properties. Two approaches of the three methods mentioned above, are most relevant for this analysis: the feature fusion based on indices derived from each sensor (pre-classification fusion) and the fusion of thematic classification results (post-classification fusion).

For large areas, sets of indicators and metrics derived from time series of SAR and optical data need to be robust, but should deliver complementary information. Various sets of indicators are being used in the literature, which can also be derived from S-1 or S-2 data. The following indicators from optical and SAR data have been identified of being useful and improving the thematic classification results: Backscatter coefficient and polarisation ratio (VH/VV) for SAR data as well as the Normalized Difference Vegetation Index (NDVI), the Normalized Difference Built-up Index (NDBI), the Modified Normalized Difference Water Index (MNDWI), the Normalized Difference Middle Infrared index (NDMIR), the Normalized Difference Red Blue index (NDRB) and the Normalized Difference Green Blue index (NDGB) for optical data. Furthermore, temporal statistics on the derived indices based on defined seasons / time intervals (i.e., $NDVI_{mean}$, $NDVI_{max}$, $NDVI_{min}$, etc.) will be applied as they are useful especially for determining vegetated classes (Esch et al., 2018). The presented candidate indices and bands will be the input for further testing the feature and decision level fusion. (1) For feature level fusion the bands and indices from S-1 and S-2 will be stacked into one dataset, which will then be used for the classification of the specific HRL. (2) For the decision level fusion, the classification will be performed separately based on either S-1 data or S-2 data. The results of both classifications will be fused based on post-classification decision rules.

3.4.2 Candidate approaches for spectral, spatial, temporal interpolation and/or fusion approaches

The synergistic use of the high spatial resolution of Sentinel-2 data with the high temporal frequency of Sentinel-3 time series aims to improve significantly the continuous monitoring of ecosystem dynamics in heterogeneous landscapes and cloud-affected areas. Then, the candidate approaches for spectral, spatial and temporal fusion between Sentinel-2 and Sentinel-3 data have to be able to capture the initial, middle and final states of changes shapes and thus capture phenology, crop growth disturbance and land cover change processes, while taking explicitly into account the spatial and spectral resolution discrepancies between images. The high spatial resolution Sentinel-2 data will act as phenology “transition points” that bracket the temporal interpolation supported by Sentinel-3 time series.

The selected methods for this spatio-spectro-temporal fusion are the following ones: the Bayesian data fusion (Fasbender et al., 2009; Xue et al., 2017), the STARFM and ESTARFM (Gao et al., 2006; Zhu et al., 2010) and the Kalman filtering (Kempeneers, 2016). These methods are justified and described in section 4.1.2. As none of these approaches has been applied to both Sentinel-2 and Sentinel-3 data, they will all have to be adjusted to the specifications of these two sensors.

3.4.3 Candidate approaches for spectral time series metrics/variables

Time series of images provided by sensors such as Sentinel-3 or MODIS cover wide areas on a daily basis, while time series acquired by Sentinel-2 and other similar sensors such as Landsat cover a few hundreds of square kilometres, but with less than a dozen of exploitable acquisitions during the year. To identify grassland covers, for example, at a field scale, this scarce temporal availability of high-resolution images is problematic – and a full season cycle cannot properly be reconstructed based on so few points on the temporal scale.

In this part, candidate approaches that are looked at aim at quantifying the accuracy of the vegetation cycle based on the images acquired by Sentinel-2 and the fused images. To this end, the most widely used indices are looked at, such as the NDVI, the NDBI, and the NDWI, while their statistical properties are computed in order to select the most relevant ones to study seasonal changes in the vegetal cover and as well as other kinds of evolution in the rest of the AOI not covered in greenery, by contrast. Other metrics can be constructed to focus on a particular land cover class or usually in combination with one or several spectral or textural indices reviewed in part 3.3.2. The types of variable can be listed as:

- **Statistical metrics of spectral values over one or several periods**, such as the average, the maximum, the minimum – especially relevant to follow seasonality and phenology, they can be used as descriptive or predictive tools, in particular to identify certain land cover classes or to monitor the evolution of forest cover;
- **Change metrics**, usually derived from a segment of radiometrically calibrated images, called a temporal trajectory, for example, the magnitude and the duration of the change, or the slope of the modelled trend – they are also used to characterize land cover and to map forest, for deforestation and recovery;
- **Stationary or non-stationary shape variables**, corresponding to the modelling of temporal trajectories as continuous functions of time, that can exhibit stationary (for example, periodic) or non-stationary (e.g. transitions from one cover to another) patterns – deviations from those patterns may characterize the disturbance of the land cover, while expected patterns such as seasonal growth can be used to derive biomass estimates;
- **Trend metrics**, among which one can find simple linear trends, seasonal trends and breakpoints to describe and decorrelate simultaneous landscape processes.

Several indices can be used to form those metrics, the NDVI being one of the most used. Here is the listed pro or contra to use the indices reviewed in global time series in the Table 3-3.

Table 3-3: List of potential candidate indices for the creation of time series.

Category	Indices	Adapted for global Time Series Use	Conditions	Remarks
Spectral Index	NDVI	✓	Applied on calibrated images BOA (atmospheric effects corrected)	Composite of images can improve the result
Spectral Index	DVI	X	-	Not normalized, different spectral responses from different sensors would yield different DVI over the same AOI
Spectral Index	RVI	X	-	Sensitivity to the geometry of the observation
Spectral Index	IRECI	X	Used over a specific AOI – not a global scale	-
Spectral Index	NDBI	X	-	Not sensitive to the date, works best at the peak vegetation though Not good with details, can depend on the lithological regimes within the AOI (e.g., volcanic vs non-volcanic soils)
Spectral Index	NBI	X	-	Depends on the sensor
Spectral Index	NDWI	✓	Applied on calibrated images BOA (atmospheric effects corrected)	Not sensitive to the date, works best at the peak vegetation though Not good with details
Spectral Index	PVI	X	-	Needs to be adapted to the AOI, depends on the soil type
Spectral Index	SAVI	X	Used over a specific AOI – not a global scale	Needs to be adapted to the AOI, depends on the soil type
Spectral Index	TSAVI	X	Used over a specific AOI – not a global scale	Needs to be adapted to the AOI, depends on the soil type
Spectral Index	MSAVI	X	Used over a specific AOI – not a global scale	Needs to be adapted to the AOI, depends on the soil type
Biophysical Index	LAI	✓	Products computed from Landsat raw images, available with the Landsat time series	-

Spectral Index	EVI	✓	Can be used with TOA images, needs in-situ measurements (?)	Depends on the sensor, on the AOI, on the atmospheric conditions (aerosol presence)
Spectral Index	ARVI	✓	Can be used with TOA images, needs in-situ measurements (?)	Depends on the atmospheric conditions (aerosol presence)
Spectral Index	GEMI	X	-	Unsuitable for creating time series over arid regions, not normalized
Spectral Index	NBR (Normalized Burn Ratio)	✓	Applied on calibrated images BOA (atmospheric effects corrected)	-
Spectral Index	Unknown suitability for time series: UI, BUI, IBI, EBBI, NBUI, MNDWI, MSI, TDVI			
Biophysical Index	Unknown suitability for time series: fAPAR, FCover			

Furby et al. (2008) studied the Landsat time-series over Australia to monitor change in the land cover, and in particular, forests. For each image of the time series, land cover zones of similar spectral properties were constituted, based on manually selected training samples. Using canonical variate analyses and contrasts between forest and non-forest regions, the spectral separability of the samples led to the creation of new indices, combinations of spectral bands, to characterize the ‘woodiness’ of the land cover, and other masks that would help to split the land covers not exactly distinguished by the first index. Thresholds were then set and applied to label forest and non-forest regions with a certain probability, based on the previous images in the time series. The following multi-temporal classification based on neural networks refined the probability and generates a layer of changes from year to year.

As mentioned in the preliminary conclusion of part 3.3.2.1 and part 3.3.2.2, the focus of this WP for the first phase will be put on widely used spectral indices, the NDVI, the BI and the NDBI. Depending on the results, refined methods will be brought in in the second phase.

4 Testing and benchmarking of candidate methods

This chapter addresses the testing and benchmarking of the candidate methods identified in chapter 3.4. Therefore, first the candidate methods are reported in detail (section 4.1). Section 4.2 describes the criteria for the actual benchmarking, while section 4.3 presents the actual benchmarking for the different integration approaches of S-1/S-2 and S-2/S-3.

4.1 Description of candidate methods

In the following, the candidate approaches for the integration/fusion of S-1/S-2 as well as S-2/S-3 time series data are explained in detail.

4.1.1 Candidate approaches for integration of S-1/S-2 complementary information

For large areas, sets of indicators and metrics derived from time series of SAR and optical data need to be robust, but should deliver complementary information. Various sets of indicators are being used in the literature, which can also be derived from S-1 or S-2 data. The following indicators from optical and SAR data have been identified of being useful and improving the thematic classification results:

Candidate indices from SAR data:

Two types of indices are seen to be relevant for a fusion with optical data, namely the backscatter coefficient in the available polarisations (VH, VV), related to plant biomass and morphology and soil conditions (moisture and roughness) (Villa et al., 2015), and polarisation ratios VH/VV (Bach et al., 2012; Dusseux et al., 2014; A. Schmitt et al., 2015).

Candidate indices from optical data:

According to Esch et al. (2018), six indices are seen to be relevant for a fusion with SAR data, namely the Normalized Difference Vegetation Index, the Normalized Difference Built-up Index, the Modified Normalized Difference Water Index, the Normalized Difference Middle Infrared index, the Normalized Difference Red Blue index (NDRB) and the Normalized Difference Green Blue index (see Table 4-1).

The Normalized Difference Built-Up Index (NDBI) has been proposed by Zha et al. (2003) and applied to extract built-up areas in many studies (Xu, 2008); nevertheless, due to the use of the middle infrared band (i.e., band 6 of the Landsat-8 OLI sensor) this index is also sensitive to vegetation with low water content (Xu, 2006) which exhibits values comparable to those of urban areas. Accordingly, the Normalized Difference Middle Infrared index (NDMIR) and the NDVI are applied to overcome this issue. On the one hand, the NDMIR uses both middle infrared bands, thus being sensitive to vegetation moisture (Lu et al., 2004)). On the other hand, the NDVI was first published by Rouse Jr. et al. (1974) and since then it has been widely employed in a variety of land cover applications. Moreover, the Modified Normalized Difference Water Index (MNDWI) is also employed to discriminate water. This index was proposed by (Xu, 2006) who enhanced the performance of the NDWI by replacing the NIR with the MIR band, which leads to a reduction of noise from built-up areas. In addition to the previous, two additional spectral indices introduced by Zhou et al. (2014) have been also included for improving the discrimination between urban areas and bare soil/bare rocks; specifically, these are the Normalized Difference Red Blue (NDRB) and Normalized Difference Green Blue (NDGB) indices.

Table 4-1: List of proposed spectral indices (source: Esch et al. (2018)).

Spectral index	Equation Landsat	Equation Sentinel-2	Citation
NDVI	(NIR–Red)/(NIR+Red)	(B8A–B4)/(B8A+B4)	Rouse Jr. et al. (1974)
NDBI	(MIR1–NIR)/(MIR1+NIR)	(B11–B8A)/(B11+B8A)	Zha et al. (2003)
MNDWI	(Green–NIR)/(Green+NIR)	(B3–B8A)/(B3+B8A)	Hanqiu Xu (2006)
NDMIR	(MIR1–MIR2)/(MIR1+MIR2)	(B11–B12)/(B11+B12)	Lu et al. (2004)
NDRB	(Red–Blue)/(Red+Blue)	(B4–B2)/(B4+B2)	Zhou et al. (2014)
NDGB	(Green–Blue)/(Green+Blue)	(B3–B2)/(B3+B2)	Zhou et al. (2014)

Furthermore, temporal statistic on the derived indices based on defined seasons/time intervals (i.e., $NDVI_{mean}$, $NDVI_{max}$, $NDVI_{min}$, etc.) will be applied as they are useful especially for determining vegetated classes (Esch et al., 2018).

The presented candidate indices and bands will be the input for further testing the feature and decision level fusion. (1) For feature level fusion the bands and indices from S-1 and S-2 will be stacked into one dataset, which will then be used for the classification of the specific HRL. (2) For the decision level fusion, the classification will be performed separately based on either S-1 data or S-2 data. The results of both classifications will be fused based on post-classification decision rules.

4.1.2 Candidate approaches for spectral, spatial, temporal interpolation and/or fusion approaches

In the following, the candidate approaches for a sprectral, spatial and temporal interpolation/fusion of S-2/S-3 are described in detail. Specifically, those are the Bayesian data fusion (section 4.1.2.1), STARFM and ESTARFM (section 4.1.2.2), as well as the Kalman filtering (section 4.1.2.3).

4.1.2.1 Bayesian data fusion

This BDF framework aims at reconciling various secondary information sources into a unique prediction. The space-time BDF data fusion relies on a general Bayesian Data Fusion approach in the context of spatial data described in Bogaert and Fasbender (2007). The prediction is based on a High-Pass Filtering approach. Details are provided by the high resolution image whereas the global fluctuations and seasonal trends are provided by the coarser image. It relies on the idea that variables of interest cannot be directly observed. Instead, they are linked to the observable variables. Some specific assumptions are chosen in order to tackle the issue of updating high resolution images.

The main advantage of a Bayesian approach is to set the problem of data fusion into a clear probabilistic framework. Another advantage of the BDF framework over other existing multi-sensor data fusion methods is that it proposes a general formulation when accounting for several secondary information sources whatever the nature of these secondary information is. Finally, an appealing feature of the BDF method is that it is freely accessible within the ORFEOTool Box.

4.1.2.2 STARFM and ESTARFM

The Spatial and Temporal Adaptive Reflectance Fusion Model (STARFM) (Gao et al., 2006) and the Enhanced Spatial and Temporal Adaptive Reflectance Fusion Model (ESTARFM) (Zhu et al., 2010) algorithms are used to obtain images high in both spatial and temporal resolutions. They can generate synthetic images based on a pair image of coarse-spatial-resolution and high-spatial-resolution (base images) and the coarse-spatial-resolution data on the prediction date through establishing a linear relationship between the base images of coarse-spatial-resolution and high-spatial-resolution.

The STARFM accurately predicts surface reflectance at an effective resolution close to that of high spatial resolution sensor. However, the performance depends on the characteristic patch size of the landscape

and degrades somewhat when used on extremely heterogeneous fine-grained landscapes (Gao et al., 2006). To overcome STARFM's inaccurate predictions of the surface reflectance over heterogeneous landscapes, the ESTARFM was proposed and has proven to be extremely effective (Zhu et al., 2010). For this reason, ESTARFM will be preferred.

Some applications showed that this fusion had excellent abilities as the blended reflectance was closely correlated with the observed reflectance. STARFM and ESTARFM are both shown to be useful in capturing reflectance changes due to changes in vegetation phenology. However, they may have problems in mapping disturbance events when land-cover changes are transient and not recorded in at least one of the baseline high-resolution (e.g., Landsat) images.

4.1.2.3 Kalman filtering

The data assimilation method is presented in Sedano et al. (2014) and Kempeneers et al. (2016). Within the framework of a Kalman filter recursive algorithm (Kalman, 1960) also known as linear quadratic estimation, the method integrates models, observations and their respective uncertainties, with partly or fully missing variables, in the calculation of the synthetic images at time steps for which medium resolution imagery is not available.

The method provided a robust performance for input data of variable qualities and environmental conditions, highlighting the relevance of including uncertainties in the integration of multi-sensor remote sensing data. One of the strengths of the Kalman filter is its robustness to a relatively large number of gaps in temporal time series. Especially in the context of data acquisition with optical sensors in conditions with frequent cloud cover, this is an important asset. It was also shown that the derived synthetic profile based on the Kalman filter was able to capture the phenological patterns of the crops.

4.1.3 Candidate approaches for spectral time series metrics/variables

The use of spectral or textural indices cannot capture all temporal details of the time series upon which it is built, even less to exploit Sentinel-2 and Sentinel-3 optical properties at their full potential. It is therefore essential to combine the results of spectral indices with metrics aiming at highlighting the temporal correlations.

For each improved or new product, a candidate method has been selected, based on the following detailed literature review:

- For the forest layer and the crop layer, statistical metrics ought to be tested;
- For the new LC/LU products like CLC+, temporal “reduction” of the time series on a monthly basis looks promising;
- For grassland, the decomposition of seasonality in the vegetation indices into trends has proved to improve the results of classification, in particular for all vegetation type classes;
- For the imperviousness layer, the method will be detailed in the WP 34, since it entirely relies on change detection.

4.1.3.1 Statistical metrics

Petitjean et al., (2012) proposed a statistical method in time series analysis based on the global comparison between two annual time series, called Dynamic Time Warping (DTW) – where the cost of alignment between two annual quantities (the reflectance of each spectral band, for a given pixel) is measured individually before being merged – by averaging – in order to determine the possible alignment of those multi-temporal sequences (Petitjean et al., 2012).

In their paper, Ingla et al. (2017) designed an almost operational process to determine the land cover type of a time series of images sensed by Formosat-2. To enforce a time coherence between the monthly updates of the product, a “composite” at a fixed date in the month is created by linear interpolation between the available images. All classification processes, with supervised learning, following this treatment are complemented by existing databases, without the input of external in-situ measurements and features extracted from this composite, such as NDVI, NDWI and brightness index.

For the time series of Landsat images over the US aimed to monitor the forest change, from 2006 to 2010, Hansen et al. (2014) used several spectral indices – the NDVI, the brightness temperature – and then derived temporal metrics based on weekly mosaics from them:

- 5-year percentiles per band, for each spectral band;
- All percentiles from the first and last years of the temporal range of the study;
- The multi-year percentile differences;
- The slope of the linear regression between the band reflectance and the time-sequence observation date;
- And the number of “good” observations.

The training data were extracted in the median NDVI image, which is resistant to the presence of outliers, unlike the mean value.

Regarding the forest layer, it seems relevant to test the statistical metrics used by Hansen et al. (2014) in order to detect the disturbance in the NDVI from year to year. The simple median NDVI over the phenological season, or at a monthly scale, is a good start to measure the relevance of this variable.

At a monthly scale, the temporal option to create a monthly composite at a fixed date based on the interpolation of the previous and following images in the time series. This technique is giving good results for land cover and land use while balancing the volume of data from the time series. It will be explored for the creation of general land cover/land use for products such as CLC+.

Depending on the results of those simple methodologies, it could be interesting to look at the following metrics that one could describe as more refined.

4.1.3.2 Change metrics

In their paper, Franklin et al. (2015) used various metrics to quantify changes in the time series. From the Landsat time series calibrated images, annual best available pixel (BAP) composites were created for each year, from 1990 to 2010, and spectral indices as well as time-series disturbance metrics, assessing the variations of land cover and based on the NBR products, were computed. Those change metrics are:

- the trend type (monotonic trend, single breakpoint or disturbed),
- the NBR root square mean error of the fitted trend regarding to the pixel values,
- the trend magnitude (difference between the first and last values of the fitted trends), the greatest disturbance magnitude, the pre-disturbance magnitude, the post-disturbance magnitude, etc.,
- the greatest disturbance year,
- the greatest disturbance duration, the pre-disturbance duration, the post-disturbance duration,
- the pre-disturbance monotonic trend duration, the post-disturbance monotonic duration, etc..

The use of NBR is justified by the considered AOI, covered with dense boreal forests. This use of time-series metrics as input for the classification of land cover improved overall accuracy by more than 6% compared to the single-date results.

It could be interesting to use the NDVI in place of the NBR if simple statistical metrics mentioned in the previous part were to fail at improving the classification outputs.

However, this method, related to change detection, should be part of the WP 34 – if set up for tests, results will be discussed in the concerned report.

4.1.3.3 Trend metrics: Modeling seasonality

Jia et al. (2014) used the added temporality of the Landsat time series to derive phenological features, based on the NDVI data provided with the raw images. Fusing MODIS and Landsat images with the STARFM algorithm, they obtained a dense time series at the Landsat spatial resolution. The indices extracted were:

- the beginning and ending dates of the growing season;
- the length of the growing season;
- the seasonal amplitude;
- the maximum fitted NDVI value.

The classification based on Maximum Likelihood Classifier (MLC) and Support Vector Machines (SVM) was fed with those indices, improving the land cover identification accuracy by an overall 3%, especially for vegetation type classes. However, they noted that the use of statistical temporal measures related to the NDVI (maximum, minimum, mean, standard deviation values of the time series) did significantly improve the results of classifiers for human-managed vegetation types, compared to the phenological features alone.

In order to establish trend metrics that would be resistant to noises, while still being able to detect changes, it is necessary to process denser time series. With the cloud cover plaguing the Belgian testsite, leading to less than twenty exploitable images for a full year, this method will not be implemented in this phase. However, this difficulty could be overcome if fused data between Sentinel-2 and Sentinel-3 become available. The time series will be updated almost daily, constituting a suitable dense time series.

4.2 Testing criteria

To analyse the usefulness of the described metrics, they can be (1) analysed visually by the operator to qualitatively compare the results, and (2) analysed quantitatively based on a detailed accuracy assessment for the separate HRL classification.

However, a comparative quality assessment of fusion methods can be based on various criteria, none of which is currently considered as standard in the literature. The evaluation of fusion performance can be divided into qualitative and quantitative approaches.

Visual comparison between the merged images given by different fusion methods is the main qualitative approach. The visual inspection will allow observing small added details and linear patterns. This methodology can seem highly subjective, since the interpretation can vary from one observer to the other, due to their knowledge or qualification. However, the “look and feel” method can quickly discern chromatic abnormal effects in the resulting images, using individually each spectral band or using a colored composite in RGB. A simple comparison between other reference images, e.g. VHR images, can help looking into more detail of the overall chromatic coherence of given entities, such as water bodies, vegetation, bare soils or urban areas.

There are several spectral quality criteria for quantitative comparisons of fused data. A large family of criteria is based on correlation coefficients. Here, the correlations between the merged and the original images will be computed and analyzed as it is clear that the fused band has to be close to the original

band. Methods aiming at low color distortion should therefore yield high correlations between the original and fused bands. Correlations have the advantage of always lying in $[-1, 1]$, thus enabling direct comparisons between quality criteria.

Correlation coefficients will be computed between corresponding spectral bands of the different images for (i) an image present in the high resolution time series, and (ii) for a high resolution image previously removed from the time series.

Recently, Alparone et al. (2004) proposed a generalization of the correlation coefficients metric and referred it as Q4 that could also be used in complement. It aims to encapsulate both spectral and radiometric distortion measurements by accounting for local measurements of the following: (i) the correlation coefficient, (ii) the bias and (iii) the change in contrast.

Furthermore, to quantitatively compare those methods however, it seems simpler to look at the results of the classifications based on those metrics. One widely spread measure to estimate the quality of an output of a clustering process is the spectral separability.

The signature separability quantifies the distance between two land cover and/or land use class spectral signatures, for any number of spectral bands that is effectively used in the classification process. It can spot unused spectral bands, and also evaluate the accuracy of a given classification output.

This metric can be calibrated by several distances, among which:

- the Euclidian distance;
- the Jeffries-Matusita distance (Swain et al., 1971).

The Euclidian distance is computed as the spectral distance between the mean vectors of each pair and is written as:

$$d(X, Y) = \sqrt{\sum_{i=1}^n (x_i - y_i)^2}$$

Where x is the first spectral signature vector, y is the second and n is the number of bands considered. It is a very simple measure and can be useful to evaluate the output of a Minimum Distance classification.

The Jeffries-Matusita distance calculates the separability of two probability distributions, the spectral classes, and is expressed as:

$$J_{xy} = 2 * (1 - e^{-B})$$

where:

$$B = \frac{1}{8}(x - y)^T \left(\frac{\Sigma_x + \Sigma_y}{2} \right)^{-1} (x - y) + \frac{1}{2} \ln \left(\frac{\left| \frac{\Sigma_x + \Sigma_y}{2} \right|}{|\Sigma_x|^{\frac{1}{2}} * |\Sigma_y|^{\frac{1}{2}}} \right)$$

Σ_x and Σ_y being the covariance matrix for, respectively, the mean vectors of each signature x and y being compared. The Jeffries-Matusita distance is known to perform better than other distance measures (such as the Euclidian distance or the divergence) but it is costly to fully compute, due to the multiple presence of covariance matrices in its expression - and can become expensive for a high number of classes.

4.3 Implementation of Testing

In the following, the actual benchmarking for the different integration approaches of S-1/S-2 and S-2/S-3 time series data are explained in detail.

4.3.1 Candidate approaches for integration of S-1/S-2 complementary information

The proposed method for the integration of S-1/S-2 imagery can only be assessed qualitatively by visual inspection within this WP. The proposed method needs labelled data to compare the gain brought by the combination of spectral indices and temporal metrics. Therefore, various classification methods that will be explored in much further details in the report of the work package 33 will quantitatively analyse the to-date proposed methods concerning the different thematic classification and will feed the results back into the second issue of this report (D6.2 : D31.1b).

4.3.1.1 Proposed methodology

The following methodology is proposed:

- (I.) For the testing of the integration/fusion methods, the common complete time series of 2017 has been identified.
- (II.) All data has been pre-processed within WP32 and should be checked for co-registration. However, the S-1 and S-2 data experience very good matching with limited to no offset.
- (III.) The spectral indices and temporal metrics for S-1 and S-2, proposed in chapter 4.1.1 have to be computed over the full time series data.
- (IV.) Analyse separability of classes based on above described measures: Euclidian distance and Jeffries-Matusita-distance
- (V.) Classification:
 - a. Analysis of feature level fusion: bands and indices from S-1 and S-2 will be stacked into one dataset, which will be the target of the classification.
 - b. Analysis of decision level fusion: classification of individual land cover classes will be performed based on S-1 data or S-2 data individually and the results will be fused based on decision rules on post-classification level.

4.3.1.2 Preliminary results

In the following, the indices and temporal metrics derived for the FRANCE test site for S-1 and S-2 data from 2017 will be discussed. While Figure 4-1 shows the temporal mean of S-2, Figure 4-2 shows the temporal mean of the backscattering coefficient in the available polarisation VV of the descending acquisition mode of the S-1 data. Figure 4-3 presents a false colour composite of the mean NIR, red and green band over the course of 2017. Figure 4-4 shows a false colour composite of the mean NDBI, NDVI and MNDWI. Here, one can see that mineral extraction sites (see the bright red areas in the small top image on the right) have a similar spectral behaviour as the dense urban areas in the centre of Toulouse (which can be seen on the right sight of the big image and appear in a bright red colour). These areas would be most likely misclassified using only optical imagery from S-2. Figure 4-5 shows a false colour composite of temporal mean of the S-1 backscattering coefficient, the mean MNDWI and mean NDBI and Figure 4-6 shows a false colour composite of temporal mean of the S-1 backscattering coefficient, the mean NDMIR and mean NDBI. In both figures one can see that the before mentioned extraction sites show a different spectral behaviour compared to the dense urban areas and thus, the complementary information derived from S-1 data in addition to optical data are promising in helping to distinguish between urban areas and bare soil. Moreover, in Figure 4-5 one can clearly distinguish between inhabited (in purple colours) and industrial areas (in bright yellow colours). Furthermore, one can better differentiate between forests (in brown colours) and grassland areas (in dark blue colours) in Figure 4-5.

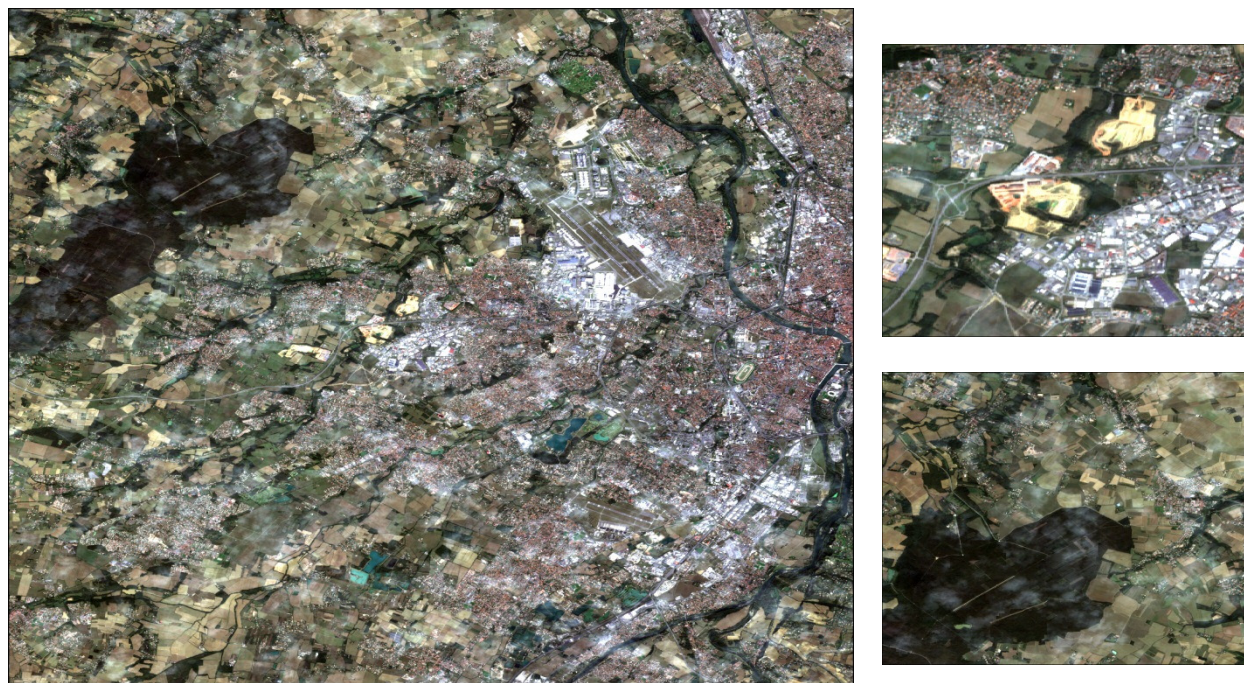


Figure 4-1: S-2 Mean RGB for 2017 for area West of Toulouse.

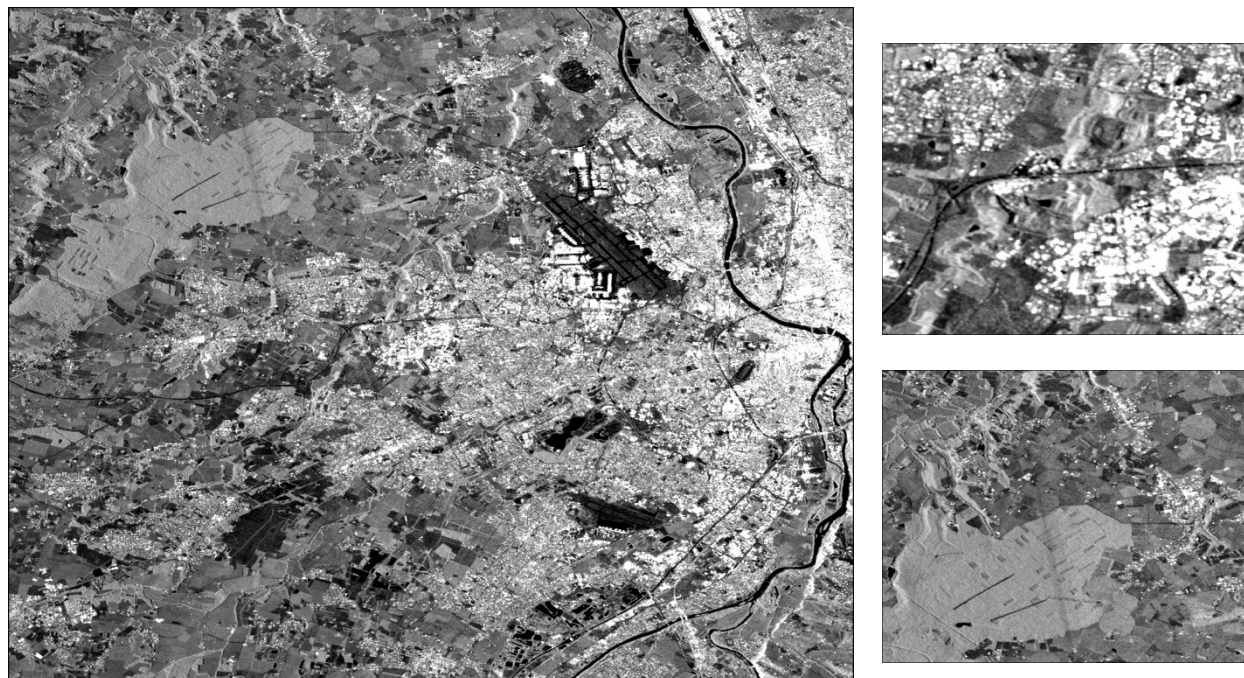


Figure 4-2: S-1 VV Desc Mean for Area West of Toulouse.

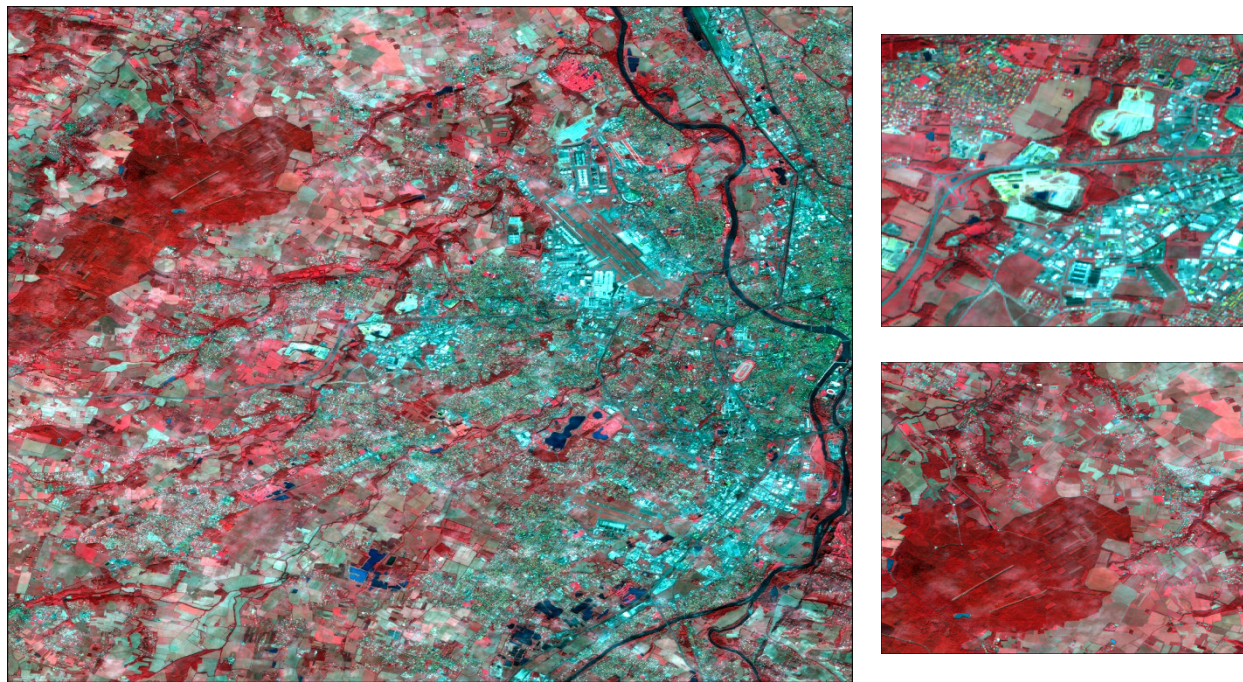


Figure 4-3: S-2 false colour composite of bands R: NIR MEAN, G: RED MEAN and B: GREEN MEAN for Mean of 2017 for area West of Toulouse.

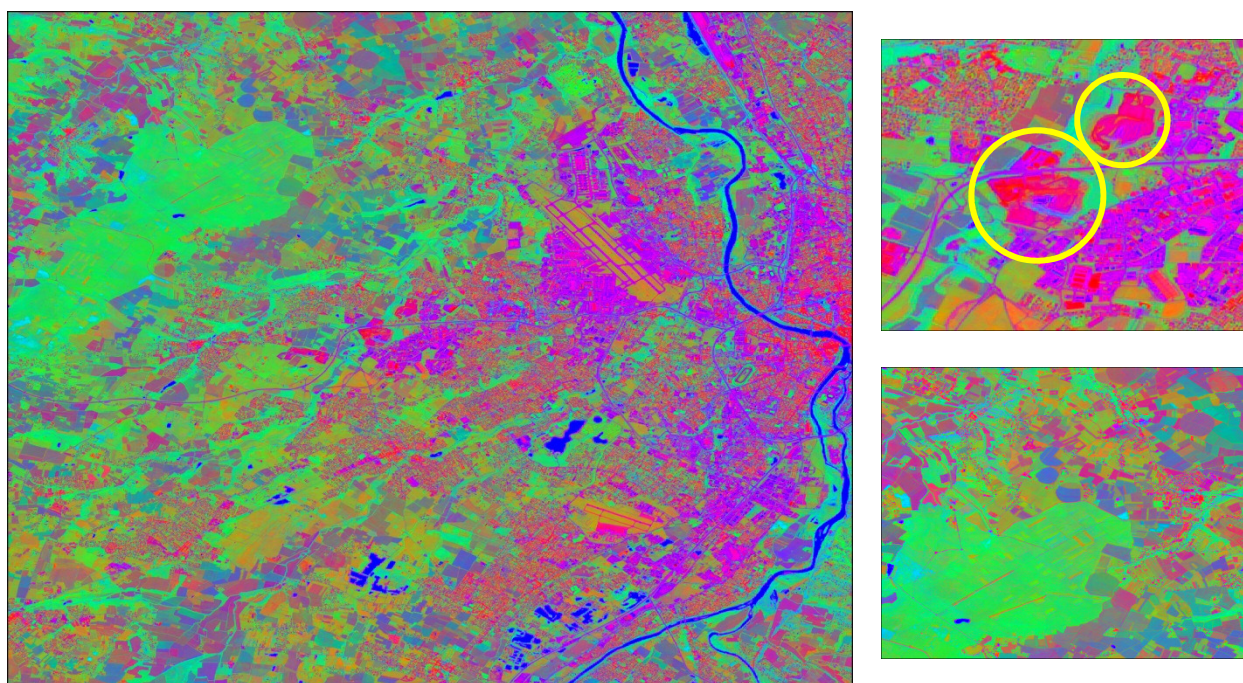


Figure 4-4: S-2 false colour composite of R: NDBI MEAN, G: NDVI MEAN and B: MNDWI MEAN for 2017 for area West of Toulouse.

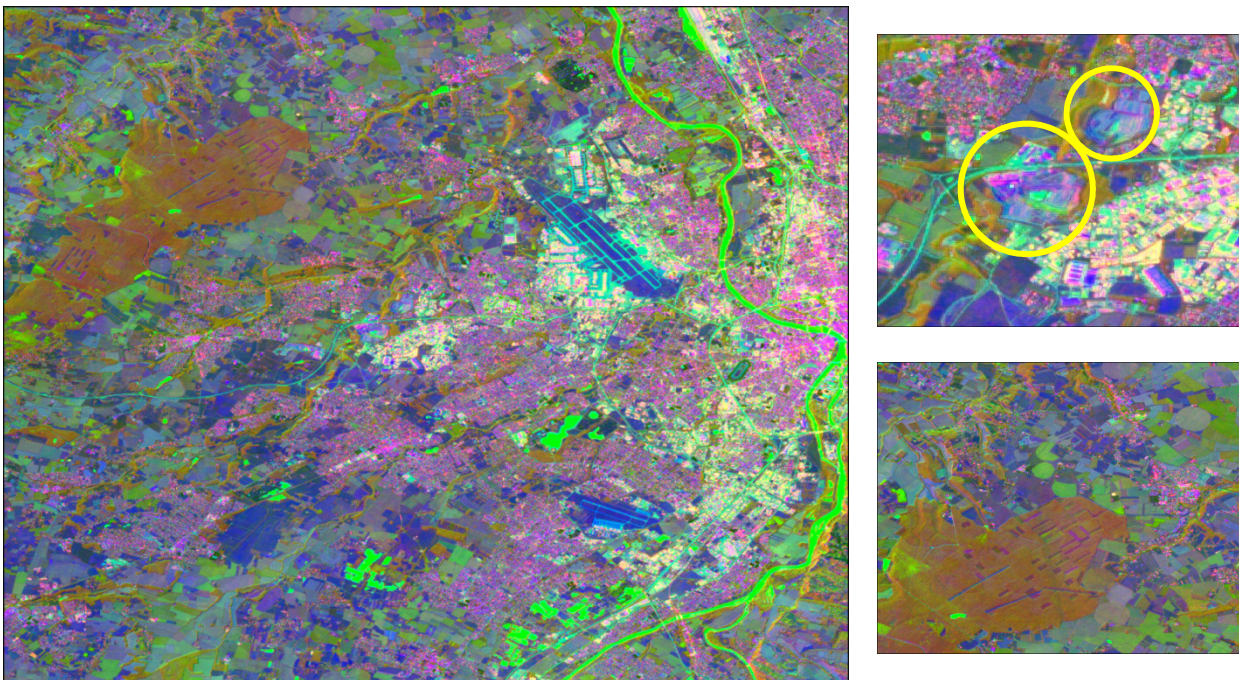


Figure 4-5: False colour composite of bands R: S-1 VV MEAN, G: S-2 MNDWI MEAN and B: S-2 NDBI MEAN for Mean of 2017 for area West of Toulouse.

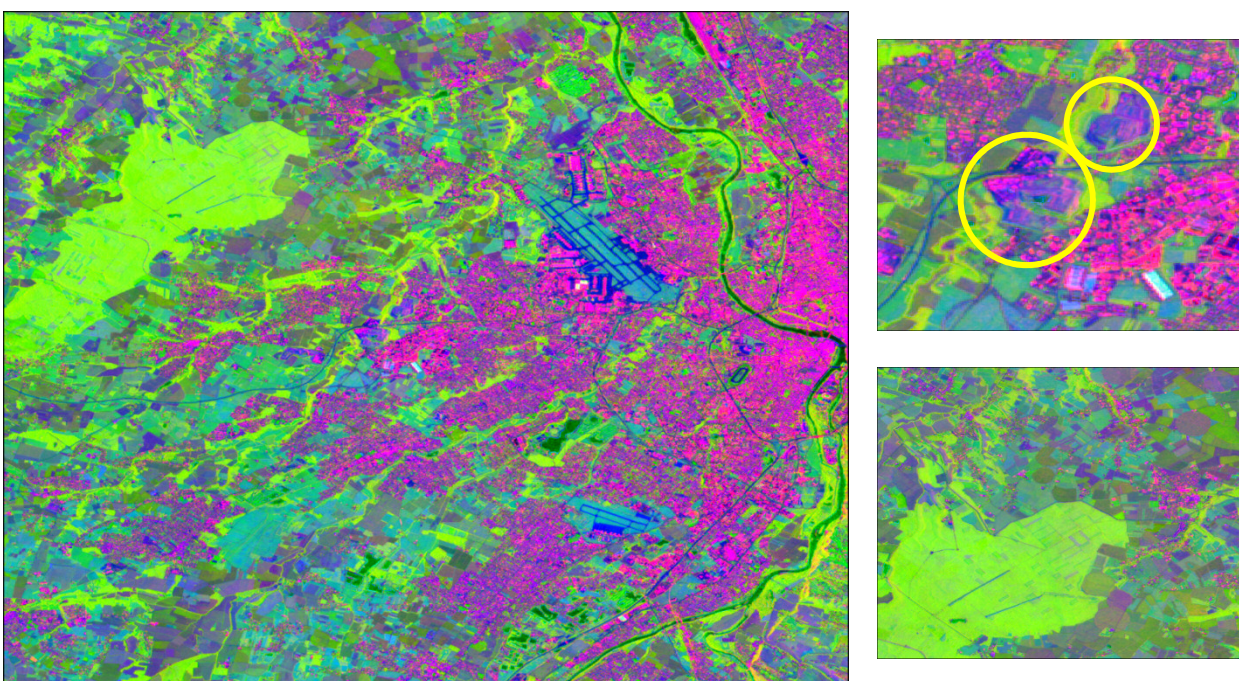


Figure 4-6: False colour composite of bands R: S-1 VV MEAN, G: S-2 NDMIR MEAN and B: S-2 NDBI MEAN for Mean of 2017 for area West of Toulouse.

4.3.1.3 Conclusions

A first qualitative analysis of the integration of S1 and S2 data shows promising results. Especially, the differentiation of specific classes can potentially be improved, e.g. urban areas and base soil or vegetated areas with different roughness as forests and grasslands.

Nevertheless, a detailed analysis has to be performed within WP33 to retrieve quantitatively results.

4.3.2 Candidate approaches for spectral, spatial, temporal interpolation and/or fusion approaches

S-3 daily surface reflectance (S-3 synergy product combining SLSTR and OLCI observations) is required to fill the gaps in S-2 time series. However, since Sentinel-3B are not yet available, Sentinel-3A and B synergy for making daily time-series will not be ready before the end of summer 2018. Consequently, the integration of Sentinel-2 and Sentinel-3 in the project has been postponed.

4.3.3 Candidate approaches for spectral and textural time series metrics/variables

Without the Sentinel-2/Sentinel-3 fused images computed for the time being, as justified in the part 4.3.2 the benchmarking can only be done on Sentinel-2 images, since they offer a high resolution (spectral and spatial) that Sentinel-3 images have not.

However, the proposed method based on spectral signature needs labelled data to compare the gain brought by the combination of spectral indices and temporal metrics. Therefore, this present benchmarking will only be done on the training data used to feed supervised classifications – various classification methods that will be explored in much further details in the report of the work package 33, concerning the thematic classification.

4.3.3.1 Proposed methodology

Here, the following methodology is proposed. First, the 31UFS tile is selected due to its flatter terrain, compared to the 31UFR tile set partly over the Ardennes, and the full year 2016 is used, since the 2017 and 2015 data are only sketchy. Due to a strong cloud cover, the initial count of 63 images is reduced to 19 exploitable images. It should be noted that most of the observations are still exhibiting cloud presence, which reduces the real number of images used in the computation of the temporal metrics. Fused data between Sentinel-2 and Sentinel-3 should provide much denser time series in the future.

Secondly, spectral indices, NDVI, NDBI and BI, are computed for each remaining image which have been pre-processed images by the JR over the Belgium site.

Thirdly, statistical metrics are derived for the yearly time series, for each spectral index. The yearly extrema (minimum and maximum) are computed per pixel as well as the standard deviation. Due to its sensitivity to outliers, the mean is passed over in favour of the median.

Fourthly, the spectral signatures (Euclidian and Jeffries-Matusita) are computed over parts of the images already correctly identified and labelled, which can be used as training data (composed of 108 different polygons), for simple clusters of five classes – cropland (class 1), forest (class 2), grassland (class 3), urban areas (class 4) and water bodies (class 5).

In the following images, Figure 4-7 to Figure 4-10, metrics related to the NDVI have been computed. The Figure 4-8 depicts the computed median NDVI over the entire time series composed of 18 exploitable images for the year 2016 which is less sensible to outliers than the arithmetic mean. The Figure 4-7 displays the maximal NDVI, while the minimal values of the NDVI can be seen on the Figure 4-9 – the darker the green, the denser the vegetal cover is. Finally the standard deviation, which captures the phenologic variations of the NDVI is depicted in the Figure 4-10.

The next set of images, Figure 4-11 to Figure 4-14, the same metrics have been computed based on the NDBI this time. The maximal values of the NDBI, seen on Figure 4-11, highlight the water bodies, whose NDBI can be very high, which is unusual but can be related to the suspended matter in water or the sunglint effect. The minimal values of the NDBI, on Figure 4-13, and the standard deviation, on Figure 4-14, can be used to spot urban areas, whose NDBI stays constant at a positive value. The median NDBI, on Figure 4-12, highlights its undiscriminated sensitivity to bare soils as well as urban areas.

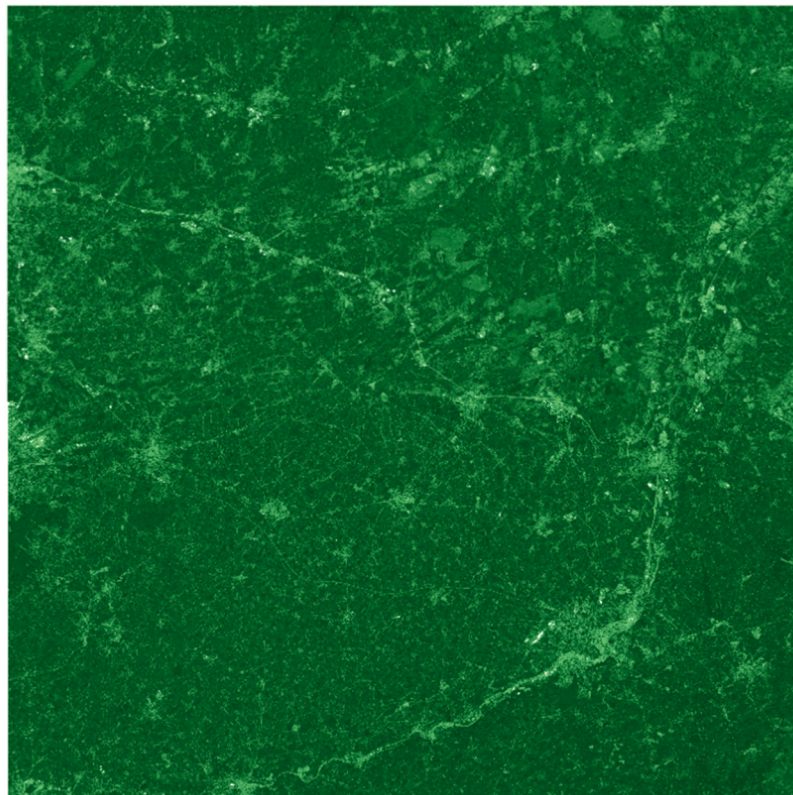


Figure 4-7: Computed maximal NDVI values per pixel: the dark green zones indicate the presence of vegetation, while lighter zones characterize urban areas and water bodies.

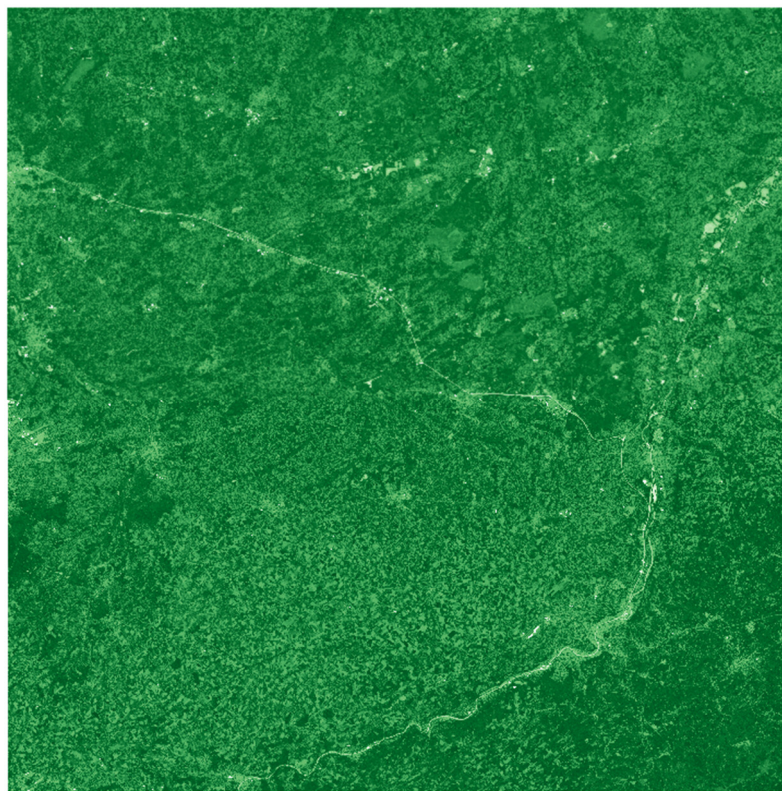


Figure 4-8: Computed NDVI median over 19 images for the year 2016, on the whole 31UFS tile. Negative values (minimum at -1) are represented in white and positive values (maximum at +1) in dark green.

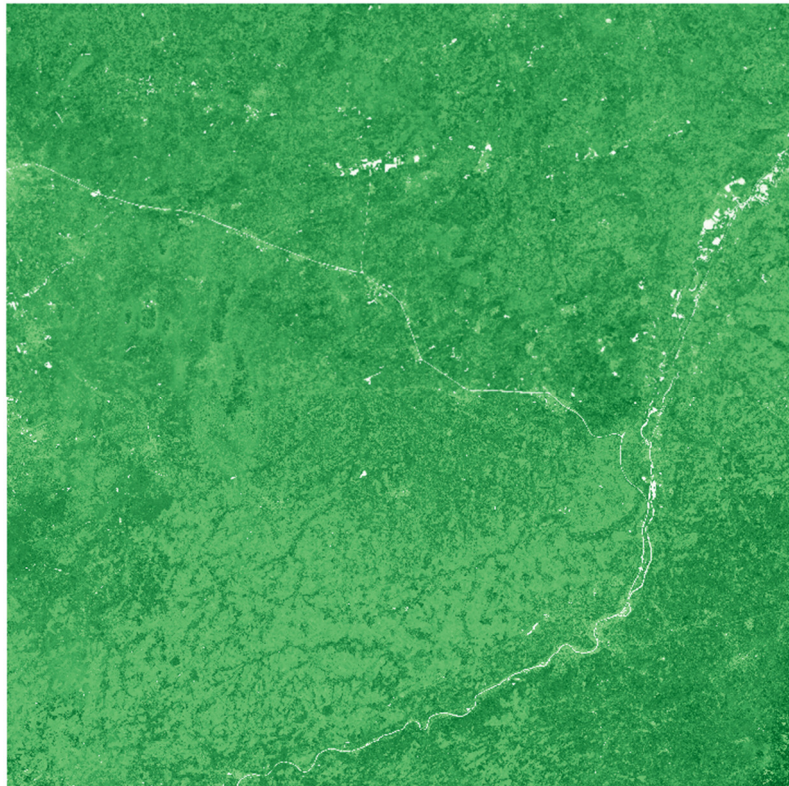


Figure 4-9: Computed minimal NDVI values per pixel: the lowest values highlight the presence of water bodies and urban areas.

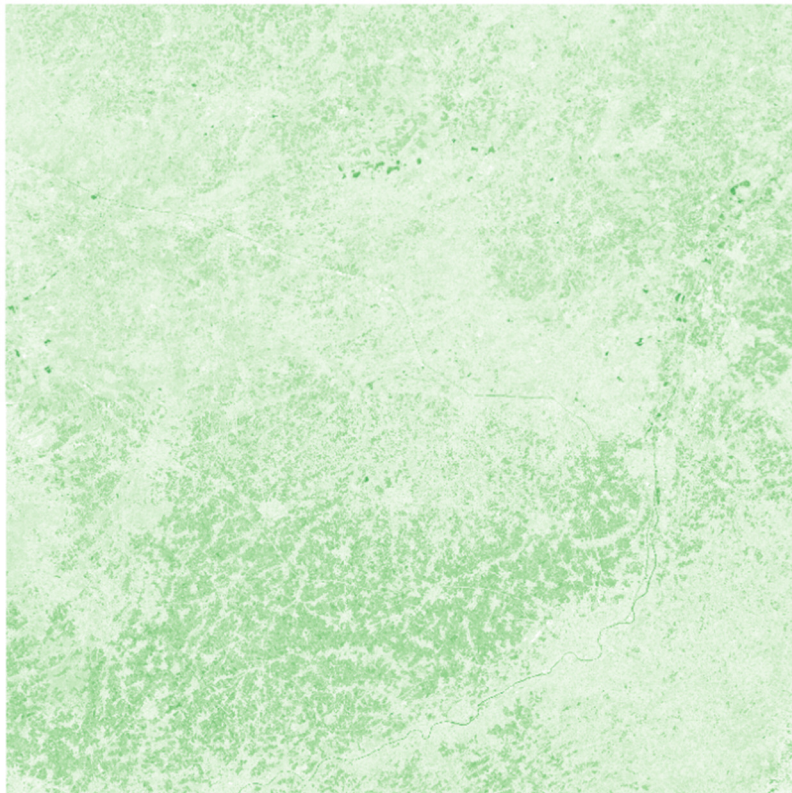


Figure 4-10: Computed standard deviation NDVI values per pixel: the highest values indicate areas where the NDVI varies the most – here, where vegetation is the densest.

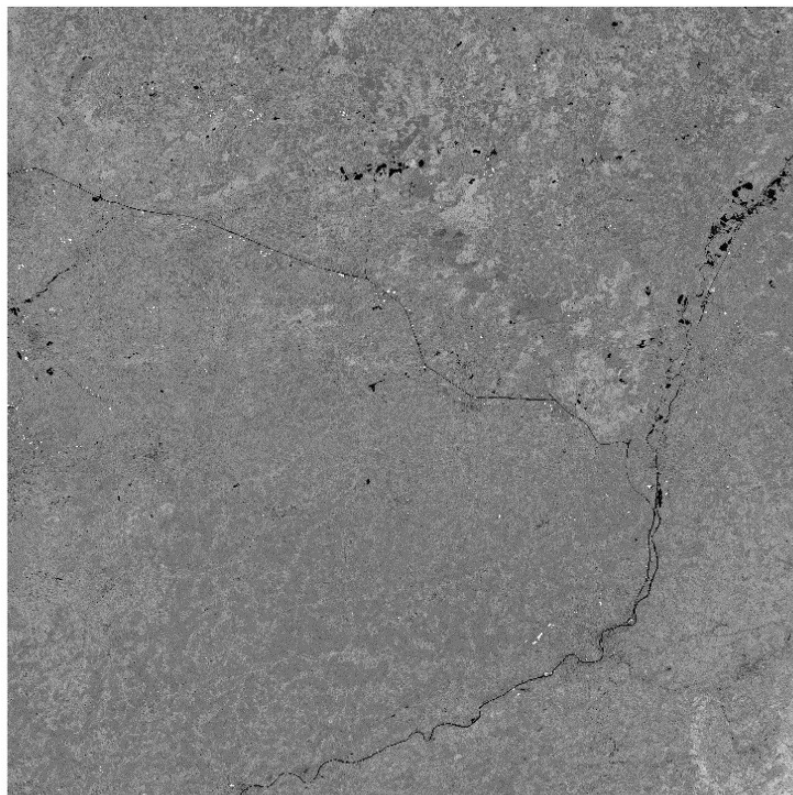


Figure 4-11: Computed maximal NDBI values per pixel: the black (positive values near +1) values delineate the water bodies with high suspended matter that reflects MIR wavelengths stronger than the NIR.

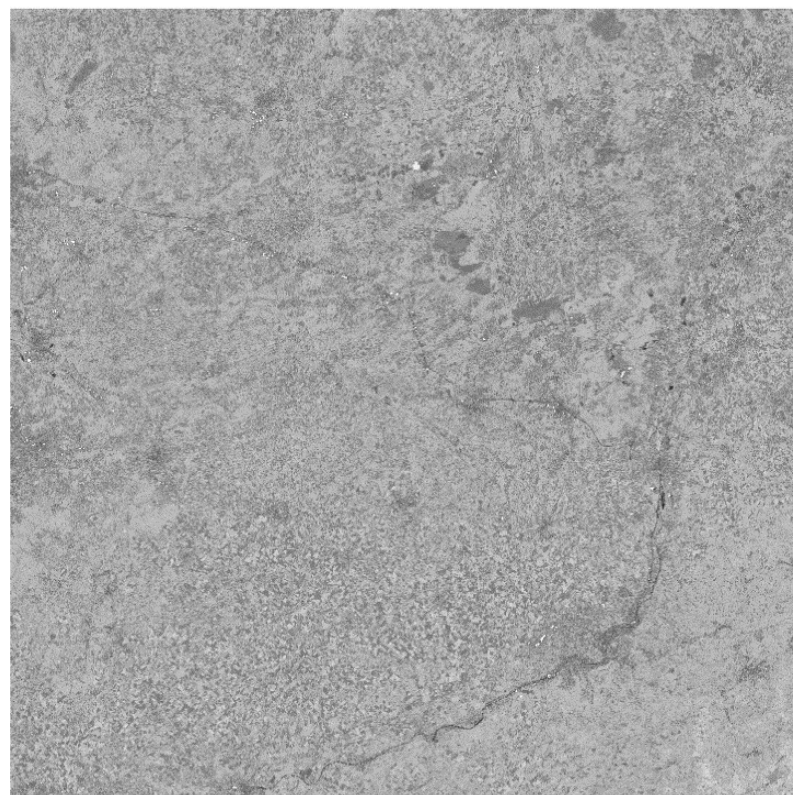


Figure 4-12: Computed median NDBI values per pixel: the highest values (in dark grey) are found over urban areas as expected.

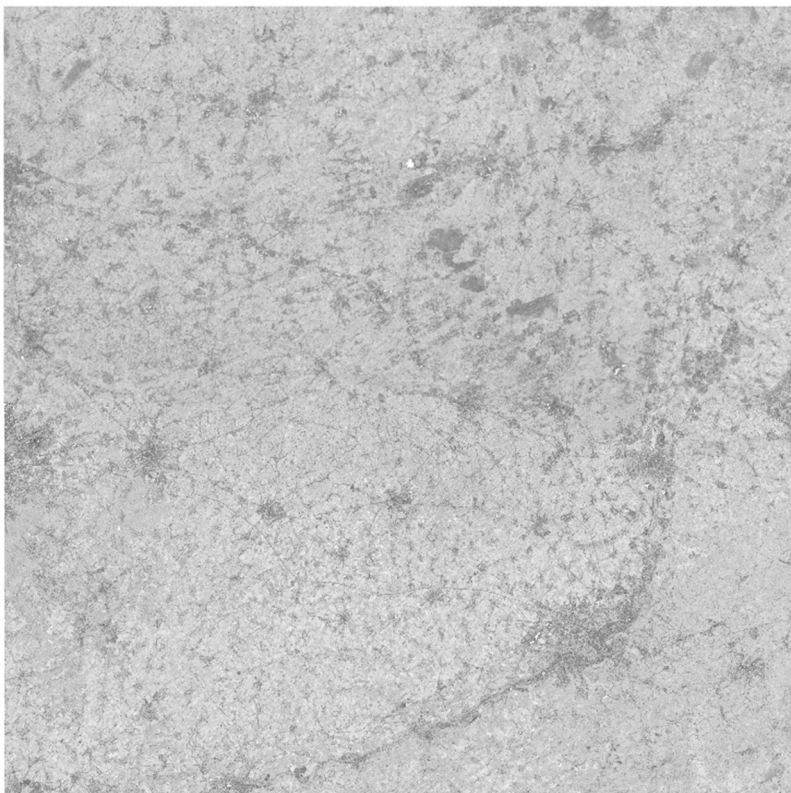


Figure 4-13: Computed minimal NDBI values per pixel: the highest values (in dark grey) over urban areas are even more highlighted than with the maximal values.

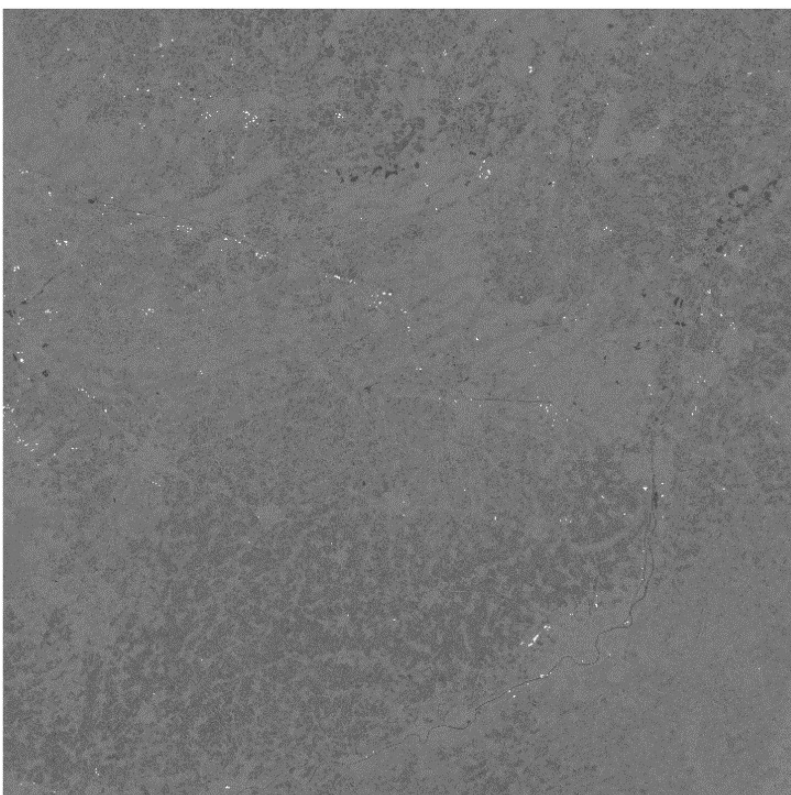


Figure 4-14: Computed standard deviation NDBI values per pixel: areas where the NDBI varies the most are vegetated, as expected due to the seasonality.

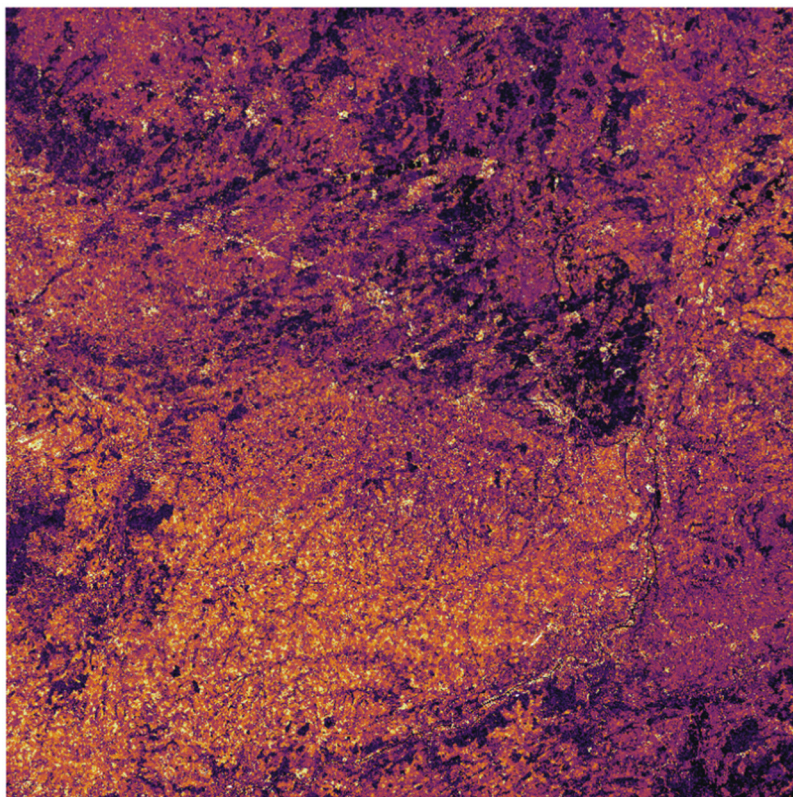


Figure 4-16: Computed median values for the red band (3) per pixel: the blackest values indicate the least reflective zones, while the yellowest are the brightest, as seen in this band.

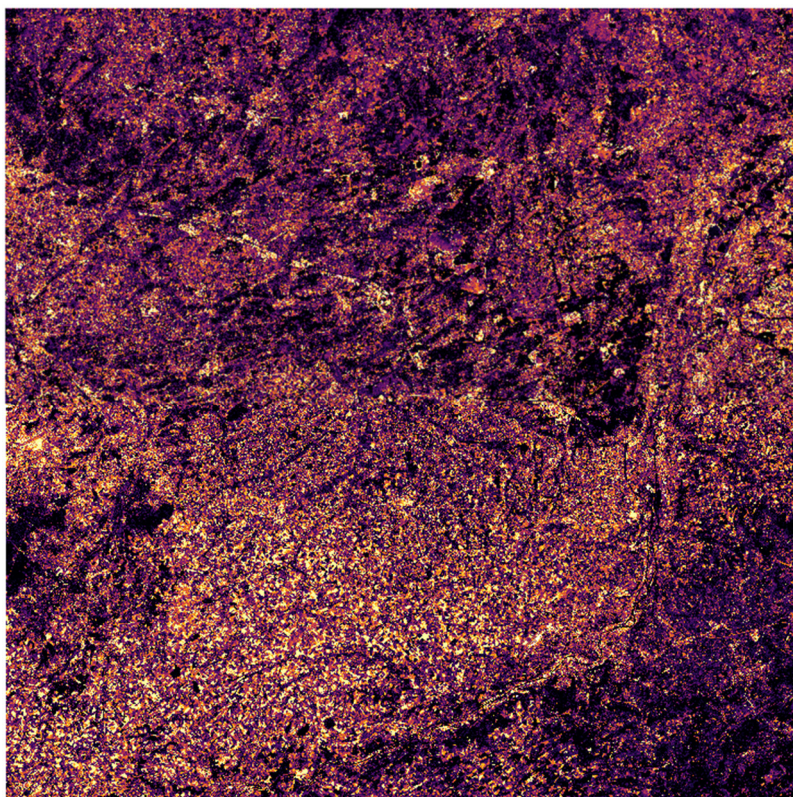


Figure 4-15: Computed median values for the green band (4) per pixel: the blackest values indicate the least reflective zones, while the yellowest are the brightest, as seen in this band.

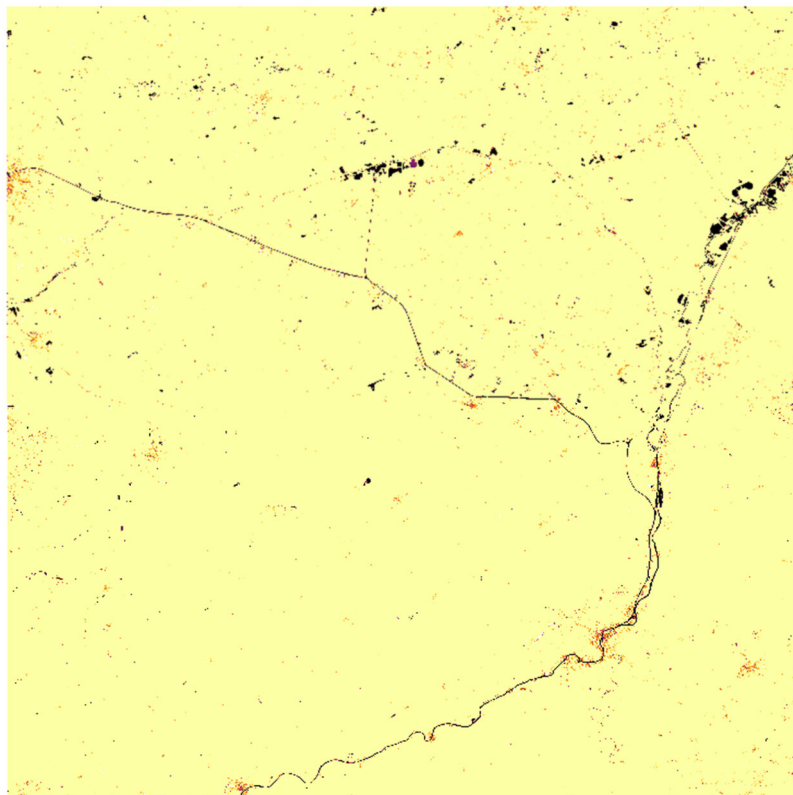


Figure 4-17: Computed median values for the narrow red edge band (7) per pixel: the blackest values indicate the least reflective zones, while the yellowest are the brightest, as seen in this band.

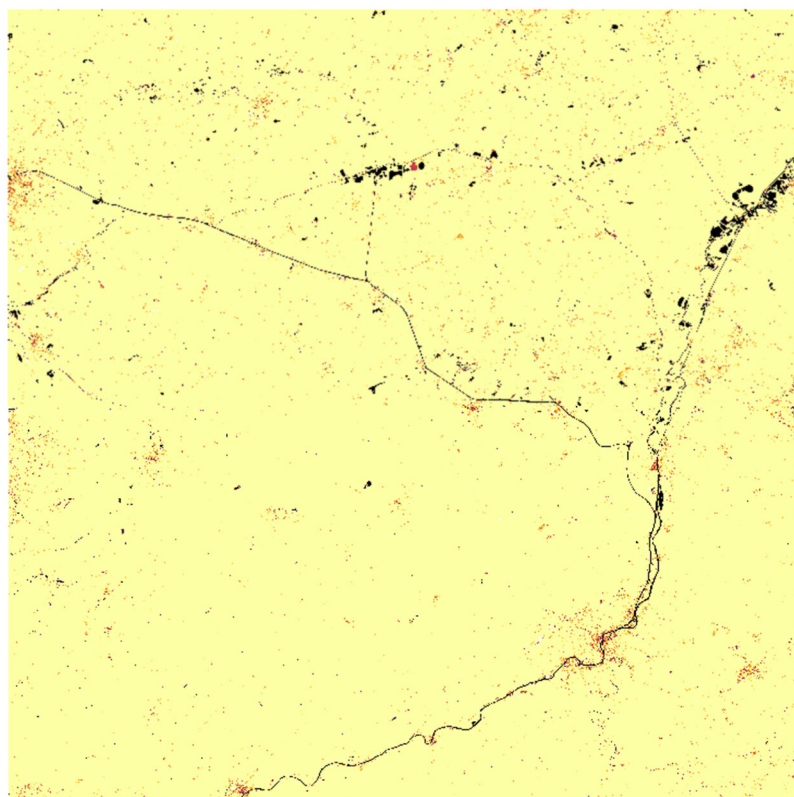


Figure 4-18: Computed median values for the wide red edge band (8) per pixel: the blackest values indicate the least reflective zones, while the yellowest are the brightest, as seen in this band.

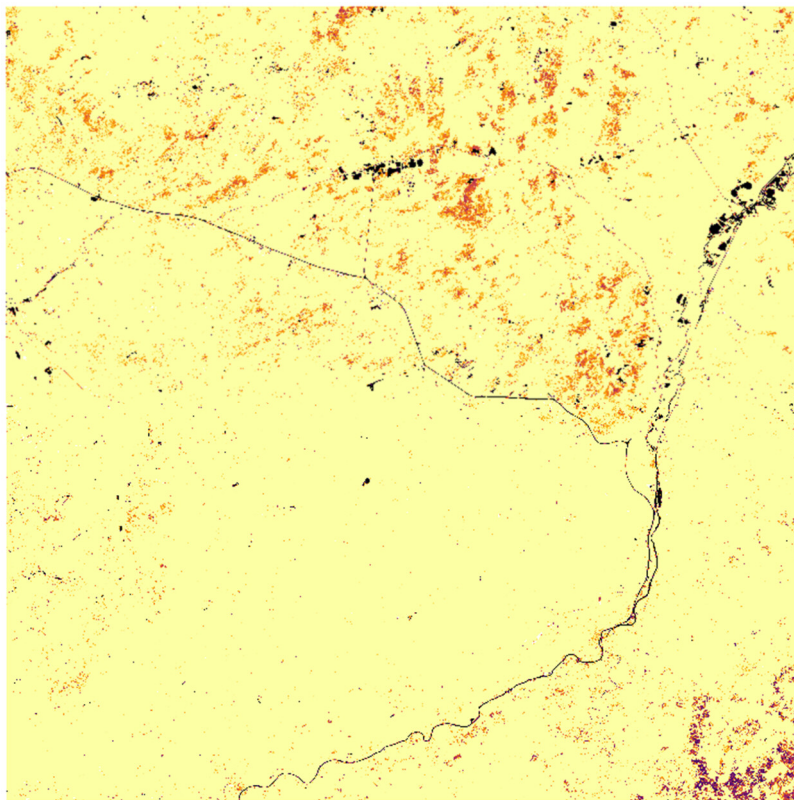


Figure 4-19: Computed median values for the first SWIR band (11) per pixel: the blackest values indicate the least reflective zones, while the yellowest are the brightest, as seen in this band.

As a point of reference, the five most significant band mean values are displayed in Figure 4-15 (for the red band 3), in Figure 4-16 (for the green band 4), in Figure 4-17 (for the narrow red edge band 7), in Figure 4-18 (for the wide red edge band 8) and in Figure 4-19 (for the first SWIR band 11). Some features can be easily identified, such as water bodies and some part of urban areas, but the discrimination brought by the spectral indices is clearly stronger.

4.3.3.2 Results and conclusion for the Statistical metrics

The Euclidian distance is not confined – unlike the Jeffries-Matusita distance which is limited by the value $1000 * \sqrt{2}$. This means for the Jeffries-Matusita a compression of the lowest or highest values; the two distances are thus complementary. Whichever distance is used, the higher the distance value is, the more separated the two considered classes are.

NDBI statistical metrics and their spectral signatures

Using only the NDBI and its statistical metrics leads to a good discrimination between the water bodies and the other type of land cover, but urban areas and grassland zones are not well separated, as seen in Table 4-2 and Table 4-3. The index cannot be used alone without further spectral or spatial information.

Table 4-2: Euclidian distance of LC discrimination using NDBI statistical signatures.

NDBI (maximum, median, minimum, standard deviation)						
		1	2	3	4	5
CROPLAND	1	0	0,261423	0,273529	0,404682	0,883717
FOREST	2	0,261423	0	0,329866	0,373776	1,07611
GRASSLAND	3	0,273529	0,329866	0	0,148652	0,774307
URBAN	4	0,404682	0,373776	0,148652	0	0,836243
WATER	5	0,883717	1,07611	0,774307	0,836243	0

Table 4-3: Jeffries-Matusita distance of LC discrimination using NDBI statistical signatures.

NDBI (maximum, median, minimum, standard deviation)						
		1	2	3	4	5
CROPLAND	1	0	1320,19	1110,06	1351,08	1409,13
FOREST	2	1320,19	0	1173,81	1141,91	1412,2
GRASSLAND	3	1110,06	1173,81	0	886,304	1350,65
URBAN	4	1351,08	1141,91	886,304	0	1384,25
WATER	5	1409,13	1412,2	1350,65	1384,25	0

NDVI statistical metrics and their spectral signatures

The NDVI signatures outperform the NDBI ones to separate the five classes, as seen in Table 4-4 and Table 4-5. However, as expected, small vegetation classes (cropland and grassland) exhibit the weakest score. This may be resolved by using a different temporality for the statistical metrics, based not on the year, but on the phenological seasonality.

Table 4-4: Euclidian distance of LC discrimination using NDVI statistical signatures.

NDVI (maximum, median, minimum, standard deviation)						
		1	2	3	4	5
CROPLAND	1	0	0,313721	0,172668	0,556771	1,42984
FOREST	2	0,313721	0	0,257861	0,677895	1,70272
GRASSLAND	3	0,172668	0,257861	0	0,449657	1,45135
URBAN	4	0,556771	0,677895	0,449657	0	1,15253
WATER	5	1,42984	1,70272	1,45135	1,15253	0

Table 4-5: Jeffries-Matusita distance of LC discrimination using NDVI statistical signatures.

NDVI (maximum, median, minimum, standard deviation)						
		1	2	3	4	5
CROPLAND	1	0	1318,78	1064,58	1385,77	1413,66
FOREST	2	1318,78	0	1223,86	1323,15	1414,21
GRASSLAND	3	1064,58	1223,86	0	1152,05	1412,17
URBAN	4	1385,77	1323,15	1152,05	0	1403,54
WATER	5	1413,66	1414,21	1412,17	1403,54	0

Combined NDBI and NDVI statistical metrics and their spectral signature

The best results are achieved when all spectral information condensed in both indices are used to separate LC/LU classes, as shown in Table 4-6 and Table 4-7. Compared to the NDVI results, it should be noted that the cropland and grassland weak discrimination is greatly improved.

Table 4-6: Euclidian distance of LC discrimination using NDBI/NDVI statistical signatures.

NDBI and NDVI combined (maximum, median, minimum, standard deviation)						
		1	2	3	4	5
CROPLAND	1	0	0,408366	0,323469	0,688303	1,6809
FOREST	2	0,408366	0	0,418693	0,774113	2,01427
GRASSLAND	3	0,323469	0,418693	0	0,473592	1,64498
URBAN	4	0,688303	0,774113	0,473592	0	1,42395
WATER	5	1,6809	2,01427	1,64498	1,42395	0

Table 4-7: Jeffries-Matusita distance of LC discrimination using NDBI/NDVI statistical signatures.

NDBI and NDVI combined (maximum, median, minimum, standard deviation)						
		1	2	3	4	5
CROPLAND	1	0	1394,49	1257,52	1405,64	1414,19
FOREST	2	1394,49	0	1317,1	1351,04	1414,21
GRASSLAND	3	1257,52	1317,1	0	1297,18	1413,72
URBAN	4	1405,64	1351,04	1297,18	0	1412,5
WATER	5	1414,19	1414,21	1413,72	1412,5	0

“Reference data”: the spectral signature of 5 of the most significant bands for Sentinel-2

As a point of comparison, reflectance in five bands (the red band, the green band, one of the red edge narrow bands, the wide red edge band and the first SWIR band) among the most significant (at 10 and 20m resolution) have been used to generate statistical metrics for the year 2016. Using those five independent sources of spectral information leads to what can be considered as the best separability achievable by our selection of indices, as shown in Table 4-8 and Table 4-9.

Table 4-8: Euclidian distance of LC discrimination using bands 3-4-8-7-11 statistical signatures.

Bands 3-4-8-7-11 (maximum, median, minimum, standard deviation)						
		1	2	3	4	5
CROPLAND	1	0	4553,08	2540,89	4200,23	8763,16
FOREST	2	4553,08	0	2345,96	1752,29	4518,3
GRASSLAND	3	2540,89	2345,96	0	1980,18	6557,42
URBAN	4	4200,23	1752,29	1980,18	0	4960,12
WATER	5	8763,16	4518,3	6557,42	4960,12	0

Table 4-9: Jeffries-Matusita distance of LC discrimination using bands 3-4-8-7-11 statistical signatures.

Bands 3-4-8-7-11 (maximum, median, minimum, standard deviation)						
		1	2	3	4	5
CROPLAND	1	0	1414,19	1379,59	1413,71	1414,21
FOREST	2	1414,19	0	1409,72	1408,83	1414,21
GRASSLAND	3	1379,59	1409,72	0	1404,24	1414,21
URBAN	4	1413,71	1408,83	1404,24	0	1414,21
WATER	5	1414,21	1414,21	1414,21	1414,21	0

Conclusion

The statistical metrics (extrema, standard deviation and median) derived from the five most significant bands contain the most complete information, therefore lead to the best results regarding the spectral separability of targeted classes, as assessed over the training data. The combination of two classical spectral indices, the NDBI and NDVI and their statistical metrics, gives the next best results compared to the statistical metrics directly derived from a selection of the most meaningful bands. The spectral separability of the five test classes is still achieved, despite a clear reduction of the spectral information.

The use of those combinations of statistical metrics and spectral indices to feed various kind of classification are explored in more detail in WP33 and 34 reports.

With this method, a time series of 19 images with ten spectral bands each, totalling 190 bands, can be reduced to a concatenation of four statistical metrics for the NDBI and as many for the NDVI, totalling only eight bands, while still achieving comparable results in term of spectral separability.

5 Conclusions and Outlook

The aim of this report is to develop and test integration strategies for S-1, S-2 and S-3 data allowing benefiting from their complementary multi-resolution, multi-temporal and multi-sensor characteristics based on state-of-the-art methods of investigated Sentinel-1/-2/-3 integration strategies. Therefore, the objective of WP 31 is to investigate the possibilities of combining S-1, S-2 and S-3 data with regards to the envisaged evolution of Copernicus Land Services addressed in ECoLaSS.

The first issue of this report mainly focussed on the analysis of State-of-the-Art methods and strategies for the integration of S-1, S-2 and S-3 data and gave first concepts for possible strategies for the integration and/or fusion for the different HRL classifications.

Regarding the integration of S-1/S-2, the information gained from both sensors is used in parallel for the classification as they record complementary characteristics of the land surface. While optical data are affected by the physical-chemical characteristics of the surface (such as leaf structure or pigmentation) SAR data represent the geometric and dielectric properties of the surface (Woodhouse, 2006). Through their multi-spectral bands ranging from visible to near infrared wavelengths, optical data provide information on diverse land covers. SAR data on the other hand are usually acquired in a single frequency for each sensor and interact with the structural characteristics of the surface depending on the wavelength, incidence angle of the sensor, as well as roughness and moisture content (Joshi et al., 2016). Here, two different methods are proposed for the integration of the S-1/S-2 data: (a) the fusion on feature level: bands and indices from S-1 and S-2 will be stacked into one dataset, which will be the target of the classification; and (b) the fusion on decision level: classification of individual land cover classes will be performed based on S-1 data or S-2 data individually and the results will be fused based on decision rules on post-classification level. Therefore, sets of indicators and metrics derived from time series of SAR and optical data are currently being used in the literature, which can also be derived from S-1 or S-2 data. The following indicators from optical and SAR data have been identified based on the state-of-the-art analysis of being useful and improving the thematic classification results: NDVI, NDBI, MNDWI, NDMIR, NDRB, as well as NDGB derived from S-2 data and the backscattering coefficient in the available polarisations (VH, VV) and polarisation ratios VH/VV derived from S-1 data. The first qualitatively assessment showed that the complementary information derived from S-1 data in addition to those from the optical data of S-2 are promising in helping to distinguish between urban areas and bare soil. Moreover, also a sub-classification of urban areas seems possible as one can clearly distinguish between inhabited and industrial areas. Also, forests and grassland areas can be visually distinguished better by using the fused data sets.

The major drawback of optical observations is the impossibility for any sensor to permeate opaque clouds, whose presence can greatly vary from one AOI to the other. The fusion of S-2 and S-3 data is expected to bring down the revisit time from five days (for S-2) to one day, helping to densify the time series (Sylla et al., 2014). However, as noticed in current HRL projects, supplemental observations (from other sensors or on an extended span of several years) often have to be required in order to fill the gaps left by clouds. To monitor slow changes, such as the urban growth, temporal metrics derived from spectral indices, such as extrema, standard deviation and median of the NDBI and NDVI, computed over a year, seem to be qualitatively as satisfactory as full datasets of raw images to characterize the land cover image by image, before proceeding to fusion on decision level. Nonetheless, to follow crop and grassland evolution in the landscape, future research will investigate in further details temporal techniques, such as temporal interpolation, to create composites based on the previous and following cloudless images in the time series, or trend modelling, that fill gaps as well as discriminate outliers, or diminish the effect of random noise.

The second issue of this report will incorporate the results gained during the prototype development in WP33, WP34, and WP35. Here, a more detailed analysis on the usefulness of the integration/fusion methods shall be performed for the single HRL classification.

6 References

- Alparone, L., Baronti, S., Garzelli, A., & Nencini, F. (2004). A global quality measurement of pan-sharpened multispectral imagery. *IEEE Geoscience and Remote Sensing Letters*, 1(4), 313-317. doi:<https://doi.org/10.1109/LGRS.2004.836784>
- As-Syakur, A. R., Adnyana, I. W. S., Arthana, I. W., & Nuarsa, I. W. (2012). Enhanced Built-Up and Bareness Index (EBBI) for Mapping Built-Up and Bare Land in an Urban Area. *Remote Sensing*, 4(10), 2957. doi:<https://doi.org/10.3390/rs4102957>
- Bach, H., Friese, M., Spannraft, K., Migdall, S., Dotzler, S., Hank, T., Frank, T., & Mauser, W. (2012, 22-27 July 2012). *Integrative use of multitemporal RapidEye and TerraSAR-X data for agricultural monitoring*. Paper presented at the 2012 IEEE International Geoscience and Remote Sensing Symposium.
- Bacour, C., Bréon, F.-M., & Maignan, F. (2006). Normalization of the directional effects in NOAA–AVHRR reflectance measurements for an improved monitoring of vegetation cycles. *Remote Sensing of Environment*, 102(3), 402-413. doi:<https://doi.org/10.1016/j.rse.2006.03.006>
- Baghdadi, N., El Hajj, M., Fayad, I., & Zribi, M. (2015). *Coupling SAR C-Band and Optical Data for Soil Moisture and Leaf Area Index Retrieval Over Irrigated Grasslands* (Vol. 9).
- Balzter, H., Cole, B., Thiel, C., & Schmullius, C. (2015). Mapping CORINE Land Cover from Sentinel-1A SAR and SRTM Digital Elevation Model Data using Random Forests. *Remote Sensing*, 7(11), 14876. doi:<https://doi.org/10.3390/rs71114876>
- Bannari, A., Asalhi, H., & Teillet, P. M. (2002). *Transformed Difference Vegetation Index (TDVI) for vegetation cover mapping*. New York: IEEE.
- Baret, F., Guyot, G., & Major, D. J. (1989, 10-14 July 1989). *TSAVI: A Vegetation Index Which Minimizes Soil Brightness Effects On LAI And APAR Estimation*. Paper presented at the Geoscience and Remote Sensing Symposium, 1989. IGARSS'89. 12th Canadian Symposium on Remote Sensing., 1989 International.
- Betbeder, J., Rapinel, S., Corgne, S., Pottier, E., & Hubert-Moy, L. (2015). TerraSAR-X dual-pol time-series for mapping of wetland vegetation. *Isprs Journal of Photogrammetry and Remote Sensing*, 107, 90-98. doi:<https://doi.org/10.1016/j.isprsjprs.2015.05.001>
- Blaes, X., Vanhalle, L., & Defourny, P. (2005). *Efficiency of crop identification based on optical and SAR image time series* (Vol. 96).
- Bogaert, P., & Fasbender, D. (2007). Bayesian data fusion in a spatial prediction context: a general formulation. *Stochastic Environmental Research and Risk Assessment*, 21(6), 695-709. doi:<https://doi.org/10.1007/s00477-006-0080-3>
- Boschetti, L., Roy, D. P., Justice, C. O., & Humber, M. L. (2015). MODIS–Landsat fusion for large area 30m burned area mapping. *Remote Sensing of Environment*, 161, 27-42. doi:<https://doi.org/10.1016/j.rse.2015.01.022>
- Brisco, B., & Brown, R. J. (1995). Multidate SAR/TM Synergism for Crop Classification in Western Canada. *Photogrammetric Engineering and Remote Sensing*, 61(8), 1009-1014.
- Buchhorn, M., Bertels, L., Smets, B., Lesiv, M., & Tsendsazar, N. (2017). Copernicus Global Land Operations “Vegetation and Energy” (CGLOPS-1): Algorithm Theoretical Basis Document. (I1.00).
- Carlson, T. N., & Ripley, D. A. (1997). On the relation between NDVI, fractional vegetation cover, and leaf area index. *Remote Sensing of Environment*, 62(3), 241-252. doi:[https://doi.org/10.1016/S0034-4257\(97\)00104-1](https://doi.org/10.1016/S0034-4257(97)00104-1)
- Chang, J., & Shoshany, M. (2016, 10-15 July 2016). *Mediterranean shrublands biomass estimation using Sentinel-1 and Sentinel-2*. Paper presented at the 2016 IEEE International Geoscience and Remote Sensing Symposium (IGARSS).
- Chen, C. M., Hepner, G. F., & Forster, R. R. (2003). Fusion of hyperspectral and radar data using the IHS transformation to enhance urban surface features. *Isprs Journal of Photogrammetry and Remote Sensing*, 58(1-2), 19-30. doi:[https://doi.org/10.1016/S0924-2716\(03\)00014-5](https://doi.org/10.1016/S0924-2716(03)00014-5)
- Chust, G., Ducrot, D., & Pretus, J. L. L. (2004). Land cover discrimination potential of radar multitemporal series and optical multispectral images in a Mediterranean cultural landscape. *International*

- Journal of Remote Sensing, 25(17), 3513-3528.
doi:<https://doi.org/10.1080/0143116032000160480>
- Clement, M. A., Kilsby, C. G., & Moore, P. (2017). Multi-temporal synthetic aperture radar flood mapping using change detection. *Journal of Flood Risk Management*. doi:<https://doi.org/10.1111/jfr3.12303>
- Dotzler, S., Bach, H., Spannraft, K., Migdall, S., Hank, T., Frank, T., & Mauser, W. (2013). Leaf area index retrieval and yield modeling for winter wheat with TerraSAR-X data compared to using optical data. Paper presented at the ESA Living Planet Symposium 2013, Edinburgh, UK.
- Dusseux, P., Corpetti, T., Hubert-Moy, L., & Corgne, S. (2014). Combined Use of Multi-Temporal Optical and Radar Satellite Images for Grassland Monitoring. *Remote Sensing*, 6(7), 6163-6182. doi:<https://doi.org/10.3390/rs6076163>
- Erasmi, S. (2013). Habitat Mapping from Optical and SAR Satellite Data: Implications of Synergy and Uncertainty for Landscape Analysis. *Photogrammetrie Fernerkundung Geoinformation*(3), 139-148. doi:<https://doi.org/10.1127/1432-8364/2013/0165>
- Esch, T., Üreyen, S., Zeidler, J., Metz-Marconcini, A., Hirner, A., Asamer, H., Tum, M., Böttcher, M., Kuchar, S., Svaton, V., & Marconcini, M. (2018). Exploiting big earth data from space – first experiences with the timescan processing chain. *Big Earth Data*, 1-20. doi:<https://doi.org/10.1080/20964471.2018.1433790>
- Fasbender, D., Obsomer, V., Bogaert, P., & Defourny, P. (2009). Updating Scarce High Resolution Images with Time Series of Coarser Images: a Bayesian Data Fusion Solution. In N. Milisavljevic (Ed.), *Sensor and Data Fusion* (pp. 245-262). https://www.intechopen.com/books/sensor_and_data_fusion/updating_scarce_high_resolution_images_with_time_series_of_coarser_images_a_bayesian_data_fusion_so: InTech.
- Fasbender, D., Obsomer, V., Radoux, J., Bogaert, P., & Defourny, P. (2007, 18-20 July 2007). *Bayesian Data Fusion: Spatial and Temporal Applications*. Paper presented at the 2007 International Workshop on the Analysis of Multi-temporal Remote Sensing Images.
- Fasbender, D., Radoux, J., & Bogaert, P. (2008). Bayesian Data Fusion for Adaptable Image Pansharpening. *IEEE Transactions on Geoscience and Remote Sensing*, 46(6), 1847-1857. doi:<https://doi.org/10.1109/TGRS.2008.917131>
- Fasbender, D., Tuia, D., Bogaert, P., & Kanevski, M. (2008). Support-Based Implementation of Bayesian Data Fusion for Spatial Enhancement: Applications to ASTER Thermal Images. *IEEE Geoscience and Remote Sensing Letters*, 5(4), 598-602. doi:<https://doi.org/10.1109/LGRS.2008.2000739>
- Ferrant, S., Selles, A., Le Page, M., Herrault, P.-A., Pelletier, C., Al-Bitar, A., Mermoz, S., Gascoin, S., Bouvet, A., Saqalli, M., Dewandel, B., Caballero, Y., Ahmed, S., Maréchal, J.-C., & Kerr, Y. (2017). Detection of Irrigated Crops from Sentinel-1 and Sentinel-2 Data to Estimate Seasonal Groundwater Use in South India. *Remote Sensing*, 9(11), 1119. doi:<https://doi.org/10.3390/rs9111119>
- Frampton, W. J., Dash, J., Watmough, G., & Milton, E. J. (2013). Evaluating the capabilities of Sentinel-2 for quantitative estimation of biophysical variables in vegetation. *ISPRS Journal of Photogrammetry and Remote Sensing*, 82, 83-92. doi:<https://doi.org/10.1016/j.isprsjprs.2013.04.007>
- Franklin, S. E., Ahmed, O. S., Wulder, M. A., White, J. C., Hermosilla, T., & Coops, N. C. (2015). Large Area Mapping of Annual Land Cover Dynamics Using Multitemporal Change Detection and Classification of Landsat Time Series Data. *Canadian Journal of Remote Sensing*, 41(4), 293-314. doi:<https://doi.org/10.1080/07038992.2015.1089401>
- Freeman, A., & Durden, S. L. (1998). A three-component scattering model for polarimetric SAR data. *IEEE Transactions on Geoscience and Remote Sensing*, 36(3), 963-973. doi:<https://doi.org/10.1109/36.673687>
- Furby, S., Caccetta, P., Wu, X., & Chia, J. (2008). *Continental scale land cover change monitoring in Australia using Landsat imagery*. Paper presented at the International Earth Conference: Studying, Modeling and Sense Making of Planet Earth, Mytilene, Lesvos, Greece.

- Gao, B.-C. (1996). NDWI—A normalized difference water index for remote sensing of vegetation liquid water from space. *Remote Sensing of Environment*, 58(3), 257-266. doi:[https://doi.org/10.1016/S0034-4257\(96\)00067-3](https://doi.org/10.1016/S0034-4257(96)00067-3)
- Gao, F., Hilker, T., Zhu, X. L., Anderson, M. C., Masek, J. G., Wang, P. J., & Yang, Y. (2015). Fusing Landsat and MODIS Data for Vegetation Monitoring. *Ieee Geoscience and Remote Sensing Magazine*, 3(3), 47-60. doi:<https://doi.org/10.1109/Mgrs.2015.2434351>
- Gao, F., Masek, J., Schwaller, M., & Hall, F. (2006). On the blending of the Landsat and MODIS surface reflectance: Predicting daily Landsat surface reflectance. *Ieee Transactions on Geoscience and Remote Sensing*, 44(8), 2207-2218. doi:<https://doi.org/10.1109/Tgrs.2006.872081>
- Gao, Q., Zribi, M., Escorihuela, M. J., & Baghdadi, N. (2017). Synergetic Use of Sentinel-1 and Sentinel-2 Data for Soil Moisture Mapping at 100 m Resolution. *Sensors*, 17(9). doi:<https://doi.org/10.3390/s17091966>
- Gengler, S., & Bogaert, P. (2018). Combining land cover products using a minimum divergence and a Bayesian data fusion approach. *International Journal of Geographical Information Science*, 32(4), 806-826. doi:10.1080/13658816.2017.1413577
- Haas, J., & Ban, Y. (2017). Sentinel-1A SAR and sentinel-2A MSI data fusion for urban ecosystem service mapping. *Remote Sensing Applications: Society and Environment*, 8, 41-53. doi:<https://doi.org/10.1016/j.rsase.2017.07.006>
- Hagolle, O., Dedieu, G., Mougenot, B., Debaecker, V., Duchemin, B., & Meygret, A. (2008). Correction of aerosol effects on multi-temporal images acquired with constant viewing angles: Application to Formosat-2 images. *Remote Sensing of Environment*, 112(4), 1689-1701. doi:<https://doi.org/10.1016/j.rse.2007.08.016>
- Hagolle, O., Huc, M., Pascual, D. V., & Dedieu, G. (2010). A multi-temporal method for cloud detection, applied to FORMOSAT-2, VEN mu S, LANDSAT and SENTINEL-2 images. *Remote Sensing of Environment*, 114(8), 1747-1755. doi:<https://doi.org/10.1016/j.rse.2010.03.002>
- Hagolle, O., Huc, M., Pascual, D. V., & Dedieu, G. (2015). A Multi-Temporal and Multi-Spectral Method to Estimate Aerosol Optical Thickness over Land, for the Atmospheric Correction of FormoSat-2, LandSat, VEN mu S and Sentinel-2 Images. *Remote Sensing*, 7(3), 2668-2691. doi:<https://doi.org/10.3390/rs70302668>
- Hansen, M. C., Egorov, A., Potapov, P. V., Stehman, S. V., Tyukavina, A., Turubanova, S. A., Roy, D. P., Goetz, S. J., Loveland, T. R., Ju, J., Kommareddy, A., Kovalskyy, V., Forsyth, C., & Bents, T. (2014). Monitoring conterminous United States (CONUS) land cover change with Web-Enabled Landsat Data (WELD). *Remote Sensing of Environment*, 140, 466-484. doi:<https://doi.org/10.1016/j.rse.2013.08.014>
- Haralick, R. M., Shanmugam, K., & Dinstein, I. (1973). Textural Features for Image Classification. *IEEE Transactions on Systems, Man, and Cybernetics*, SMC-3(6), 610-621. doi:<https://doi.org/10.1109/TSMC.1973.4309314>
- Hilker, T., Wulder, M. A., Coops, N. C., Linke, J., McDermid, G., Masek, J. G., Gao, F., & White, J. C. (2009). A new data fusion model for high spatial- and temporal-resolution mapping of forest disturbance based on Landsat and MODIS. *Remote Sensing of Environment*, 113(8), 1613-1627. doi:<https://doi.org/10.1016/j.rse.2009.03.007>
- Hill, M. J., Smith, A. M., & Foster, T. C. (2000). Remote Sensing of Grassland with RADARSAT; Case Studies from Australia and Canada. *Canadian Journal of Remote Sensing*, 26(4), 285-296. doi:<https://doi.org/10.1080/07038992.2000.10874779>
- Hill, M. J., Ticehurst, C. J., Lee, J. S., Grunes, M. R., Donald, G. E., & Henry, D. (2005). Integration of optical and radar classifications for mapping pasture type in western Australia. *Ieee Transactions on Geoscience and Remote Sensing*, 43(7), 1665-1681. doi:<https://doi.org/10.1109/Tgrs.2005.846868>
- Hirschmugl, M., Deutscher, J., Gutjahr, K. H., Sobe, C., & Schardt, M. (2017). Combined use of SAR and optical time series data for near real-time forest disturbance mapping. Paper presented at the 2017 9th International Workshop on the Analysis of Multitemporal Remote Sensing Images (MultiTemp).

- Huete, A. R. (1988). A Soil-Adjusted Vegetation Index (Savi). *Remote Sensing of Environment*, 25(3), 295-309. doi:[https://doi.org/10.1016/0034-4257\(88\)90106-X](https://doi.org/10.1016/0034-4257(88)90106-X)
- Hunt, E. R., & Rock, B. N. (1989). Detection of Changes in Leaf Water-Content Using Near-Infrared and Middle-Infrared Reflectances. *Remote Sensing of Environment*, 30(1), 43-54. doi:[https://doi.org/10.1016/0034-4257\(89\)90046-1](https://doi.org/10.1016/0034-4257(89)90046-1)
- Inglaña, J., Vincent, A., Arias, M., & Marais-Sicre, C. (2016). Improved Early Crop Type Identification By Joint Use of High Temporal Resolution SAR And Optical Image Time Series. *Remote Sensing*, 8(5), 362.
- Inglaña, J., Vincent, A., Arias, M., Tardy, B., Morin, D., & Rodes, I. (2017). Operational High Resolution Land Cover Map Production at the Country Scale Using Satellite Image Time Series. *Remote Sensing*, 9(1). doi:<https://doi.org/10.3390/rs9010095>
- Jenerowicz, A., & Siok, K. (2017). *Fusion of radar and optical data for mapping and monitoring of water bodies*. Paper presented at the SPIE Remote Sensing.
- Jia, K., Liang, S., Wei, X., Yao, Y., Su, Y., Jiang, B., & Wang, X. (2014). Land Cover Classification of Landsat Data with Phenological Features Extracted from Time Series MODIS NDVI Data. *Remote Sensing*, 6(11), 11518. doi:<https://doi.org/10.3390/rs61111518>
- Jieli, C., Manchun, L., Yongxue, L., Chenglei, S., & Wei, H. (2010, 18-20 June 2010). *Extract residential areas automatically by New Built-up Index*. Paper presented at the 2010 18th International Conference on Geoinformatics.
- Jordan, C. F. (1969). Derivation of Leaf-Area Index from Quality of Light on the Forest Floor. *Ecology*, 50(4), 663-666. doi:<https://doi.org/10.2307/1936256>
- Joshi, N., Baumann, M., Ehammer, A., Fensholt, R., Grogan, K., Hostert, P., Jepsen, M. R., Kuemmerle, T., Meyfroidt, P., Mitchard, E. T. A., Reiche, J., Ryan, C. M., & Waske, B. (2016). A Review of the Application of Optical and Radar Remote Sensing Data Fusion to Land Use Mapping and Monitoring. *Remote Sensing*, 8(1). doi:<https://doi.org/10.3390/rs8010070>
- Kaimaris, D., & Patias, P. (2016). Identification and Area Measurement of the Built-up Area with the Built-up Index (BUI). *International Journal of Advanced Remote Sensing and GIS*(1), 1844-1858%V 1845. doi:<https://doi.org/10.23953/cloud.ijarsg.64>
- Kalman, R. E. (1960). A New Approach to Linear Filtering and Prediction Problems. *Journal of Basic Engineering*, 82(1), 35-45. doi:<https://doi.org/10.1115/1.3662552>
- Kaufman, Y. J., & Tanre, D. (1992). Atmospherically resistant vegetation index (ARVI) for EOS-MODIS. *IEEE Transactions on Geoscience and Remote Sensing*, 30(2), 261-270. doi:<https://doi.org/10.1109/36.134076>
- Kawamura, M., Jayamana, S., & Tsujiko, Y. (1996). Relation between Social and Environmental Conditions in Colombo Sri Lanka and the Urban Index Estimated by Satellite Remote Sessing Data. *International Archives of Photogrammetry Remote Sensing*, XXXI, Part B7, Vienna, 321-326.
- Kempeneers, P., Sedano, F., Piccard, I., & Eerens, H. (2016). Data Assimilation of PROBA-V 100 and 300 m. *IEEE Journal of Selected Topics in Applied Earth Observations and Remote Sensing*, 9(7), 3314-3325. doi:<https://doi.org/10.1109/JSTARS.2016.2527922>
- Korosov, A., Moiseev, A., Shuchman, R., & Podzdyakov, D. (2017). MODIS-AQUA and Sentinel-2 data fusion: application to optically shallow waters of lake Michigan. *Transactions of Karelian Research Center of Russian Academy of Sciences*. doi:<https://doi.org/10.17076/lm692>
- Le Hegarat-Mascle, S., Quesney, A., Vidal-Madjar, D., Taconet, O., Normand, M., & Loumagne, C. (2000). Land cover discrimination from multitemporal ERS images and multispectral Landsat images: A study case in an agricultural area in France. *International Journal of Remote Sensing*, 21(3), 435-456. doi:<https://doi.org/10.1080/014311600210678>
- Lefebvre, A., Beaugendre, N., Pennec, A., Sannier, C., & Corpelli, T. (2013). *Using data fusion to update built-up areas of the 2012 European High-Resolution Layer Imperviousness*. Paper presented at the 33rd EARSeL Symposium Conference - Towards Horizon 2020: Earth Observation and Social Perspectives, Matera, Italy.
- Lehmann, E. A., Caccetta, P., Lowell, K., Mitchell, A., Zhou, Z. S., Held, A., Milne, T., & Tapley, I. (2015). SAR and optical remote sensing: Assessment of complementarity and interoperability in the

- context of a large-scale operational forest monitoring system. *Remote Sensing of Environment*, 156, 335-348. doi:<https://doi.org/10.1016/j.rse.2014.09.034>
- Liu, H., & Huete, A. (1995). A feedback based modification of the NDVI to minimize canopy background and atmospheric noise. *Ieee Transactions on Geoscience and Remote Sensing*, 33(2), 457-465. doi:<https://doi.org/10.1109/36.377946>
- Lu, D. S., Mausel, P., Brondizio, E., & Moran, E. (2004). Relationships between forest stand parameters and Landsat TM spectral responses in the Brazilian Amazon Basin. *Forest Ecology and Management*, 198(1-3), 149-167. doi:<https://doi.org/10.1016/j.foreco.2004.03.048>
- Mallat, S. G. (1989). Multiresolution Approximations and Wavelet Orthonormal Bases of L₂(R). *Transactions of the American Mathematical Society*, 315(1), 69-87. doi:<https://doi.org/10.2307/2001373>
- Marconcini, M., Üreyen, S., Esch, T., Metz, A., & Zeidler, J. (2017). *Mapping urban areas globally by jointly exploiting optical and radar imagery - the GUF+ 2015 layer*. Paper presented at the WorldCover 2017, ESA-ESRIN, Frascati (Rome), Italy.
- Mathieu, R., Pouget, M., Cervelle, B., & Escadafal, R. (1998). Relationships between satellite-based radiometric indices simulated using laboratory reflectance data and typic soil color of an arid environment. *Remote Sensing of Environment*, 66(1), 17-28. doi:[https://doi.org/10.1016/S0034-4257\(98\)00030-3](https://doi.org/10.1016/S0034-4257(98)00030-3)
- McNairn, H., Champagne, C., Shang, J., Holmstrom, D., & Reichert, G. (2009). Integration of optical and Synthetic Aperture Radar (SAR) imagery for delivering operational annual crop inventories. *Isprs Journal of Photogrammetry and Remote Sensing*, 64(5), 434-449. doi:<https://doi.org/10.1016/j.isprsjprs.2008.07.006>
- Meyer, Y. (1990). *Wavelets and operators*: Cambridge University Press.
- Michelson, D. B., Liljeberg, B. M., & Pilesjo, P. (2000). Comparison of algorithms for classifying Swedish landcover using Landsat TM and ERS-1 SAR data. *Remote Sensing of Environment*, 71(1), 1-15. doi:[https://doi.org/10.1016/S0034-4257\(99\)00024-3](https://doi.org/10.1016/S0034-4257(99)00024-3)
- Molina, D. E., & Datcu, M. (2016). Data mining tools for Sentinel 1 and Sentinel 2 data exploitation. *Image and Signal Processing for Remote Sensing Xxii*, 10004. doi:<https://doi.org/10.1117/12.2241542>
- Morishita, Y., & Hanssen, R. F. (2015). Temporal Decorrelation in L-, C-, and X-band Satellite Radar Interferometry for Pasture on Drained Peat Soils. *Ieee Transactions on Geoscience and Remote Sensing*, 53(2), 1096-1104. doi:<https://doi.org/10.1109/TGRS.2014.2333814>
- Morlet, J., Arens, G., Fourgeau, E., & Giard, D. (1982a). Wave-Propagation and Sampling Theory .1. Complex Signal and Scattering in Multilayered Media. *Geophysics*, 47(2), 203-221. doi:Doi 10.1190/1.1441328
- Morlet, J., Arens, G., Fourgeau, E., & Giard, D. (1982b). Wave-Propagation and Sampling Theory .2. Sampling Theory and Complex Waves. *Geophysics*, 47(2), 222-236. doi:Doi 10.1190/1.1441329
- Navarro, A., Rolim, J., Miguel, I., Catalao, J., Silva, J., Painho, M., & Vekerdy, Z. (2016). Crop Monitoring Based on SPOT-5 Take-5 and Sentinel-1A Data for the Estimation of Crop Water Requirements. *Remote Sensing*, 8(6). doi:<https://doi.org/10.3390/rs8060525>
- Notarnicola, C., Asam, S., Jacob, A., Marin, C., Rossi, M., & Stendardi, L. (2017). *Mountain crop monitoring with multitemporal Sentinel-1 and Sentinel-2 imagery*. Paper presented at the 2017 9th International Workshop on the Analysis of Multitemporal Remote Sensing Images (MultiTemp).
- Pesaresi, M., Gerhardinger, A., & Kayitakire, F. (2008). A Robust Built-Up Area Presence Index by Anisotropic Rotation-Invariant Textural Measure. *IEEE Journal of Selected Topics in Applied Earth Observations and Remote Sensing*, 1(3), 180-192. doi:<https://doi.org/10.1109/Jstars.2008.2002869>
- Petitjean, F., Inglada, J., & Gancarski, P. (2012). Satellite Image Time Series Analysis Under Time Warping. *Ieee Transactions on Geoscience and Remote Sensing*, 50(8), 3081-3095. doi:<https://doi.org/10.1109/TGRS.2011.2179050>

- Pinty, B., & Verstraete, M. M. (1992). GEMI: a non-linear index to monitor global vegetation from satellites. *Vegetatio*, 101(1), 15-20. doi:<https://doi.org/10.1007/bf00031911>
- Poggio, L., & Gimona, A. (2017). Assimilation of optical and radar remote sensing data in 3D mapping of soil properties over large areas. *Sci Total Environ*, 579, 1094-1110. doi:<https://doi.org/10.1016/j.scitotenv.2016.11.078>
- Pohl, C., & Van Genderen, J. L. (1998). Review article Multisensor image fusion in remote sensing: Concepts, methods and applications. *International Journal of Remote Sensing*, 19(5), 823-854. doi:<https://doi.org/10.1080/014311698215748>
- Pohl, C., & Van Genderen, J. L. (2015). Structuring contemporary remote sensing image fusion. *International Journal of Image and Data Fusion*, 6(1), 3-21. doi:<https://doi.org/10.1080/19479832.2014.998727>
- Price, K. P., Guo, X., & Stiles, J. M. (2002). Comparison of Landsat TM and ERS-2 SAR data for discriminating among grassland types and treatments in eastern Kansas. *Computers and Electronics in Agriculture*, 37(1), 157-171. doi:[https://doi.org/10.1016/S0168-1699\(02\)00110-2](https://doi.org/10.1016/S0168-1699(02)00110-2)
- Prince, S. D., & Goward, S. N. (1995). Global primary production: A remote sensing approach. *Journal of Biogeography*, 22(4-5), 815-835. doi:<https://doi.org/10.2307/2845983>
- Qi, J., Chehbouni, A., Huete, A. R., Kerr, Y. H., & Sorooshian, S. (1994). A modified soil adjusted vegetation index. *Remote Sensing of Environment*, 48(2), 119-126. doi:[https://doi.org/10.1016/0034-4257\(94\)90134-1](https://doi.org/10.1016/0034-4257(94)90134-1)
- Ray, T. W. (1994). A FAQ on Vegetation in Remote Sensing.
- Reiche, J., Verbesselt, J., Hoekman, D., & Herold, M. (2015). Fusing Landsat and SAR time series to detect deforestation in the tropics. *Remote Sensing of Environment*, 156, 276-293. doi:<https://doi.org/10.1016/j.rse.2014.10.001>
- Richardson, A. J., & Wiegand, C. L. (1977). Distinguishing Vegetation from Soil Background Information. *Photogrammetric Engineering and Remote Sensing*, 43(12), 1541-1552.
- Rouse Jr., J. W., Haas, R. H., Schell, J. A., & Deering, D. W. (1974). *Monitoring vegetation systems in the great plains with ERTS*. Paper presented at the 3d Earth Resources Technology Satellite-1 Symposium.
- Schmitt, A., Wendleder, A., & Hinz, S. (2015). The Kennaugh element framework for multi-scale, multi-polarized, multi-temporal and multi-frequency SAR image preparation. *Isprs Journal of Photogrammetry and Remote Sensing*, 102, 122-139. doi:<https://doi.org/10.1016/j.isprsjprs.2015.01.007>
- Schmitt, M., & Zhu, X. X. (2016). Data Fusion and Remote Sensing: An ever-growing relationship. *Ieee Geoscience and Remote Sensing Magazine*, 4(4), 6-23. doi:<https://doi.org/10.1109/MGRS.2016.2561021>
- Schmullius, C., Thiel, C., Pathe, C., & Santoro, M. (2015). Radar Time Series for Land Cover and Forest Mapping. In C. Kuenzer, S. Dech, & W. Wagner (Eds.), *Remote Sensing Time Series: Revealing Land Surface Dynamics* (pp. 323-356). Cham: Springer International Publishing.
- Schuster, C., Schmidt, T., Conrad, C., Kleinschmit, B., & Forster, M. (2015). Grassland habitat mapping by intra-annual time series analysis - Comparison of RapidEye and TerraSAR-X satellite data. *International Journal of Applied Earth Observation and Geoinformation*, 34, 25-34. doi:<https://doi.org/10.1016/j.jag.2014.06.004>
- Sedano, F., Kempeneers, P., & Hurt, G. (2014). A Kalman Filter-Based Method to Generate Continuous Time Series of Medium-Resolution NDVI Images. *Remote Sensing*, 6(12), 12381-12408. doi:<https://doi.org/10.3390/rs61212381>
- Sinha, P., Kiran Verma, N., & Ayele, E. (2016). *Urban Built-up Area Extraction and Change Detection of Adama Municipal Area using Time-Series Landsat Images*.
- Smith, A. M., & Buckley, J. R. (2011). Investigating RADARSAT-2 as a tool for monitoring grassland in western Canada. *Canadian Journal of Remote Sensing*, 37(1), 93-102. doi:<https://doi.org/10.5589/m11-027>

- Smith, A. M., Major, D. J., McNeil, R. L., Willms, W. D., Brisco, B., & Brown, R. J. (1995). Complementarity of radar and visible-infrared sensors in assessing rangeland condition. *Remote Sensing of Environment*, 52(3), 173-180. doi:[https://doi.org/10.1016/0034-4257\(95\)00033-W](https://doi.org/10.1016/0034-4257(95)00033-W)
- Stefanski, J., Kuemmerle, T., Chaskovskyy, O., Griffiths, P., Havryluk, V., Knorn, J., Korol, N., Sieber, A., & Waske, B. (2014). Mapping Land Management Regimes in Western Ukraine Using Optical and SAR Data. *Remote Sensing*, 6(6), 5279-5305. doi:<https://doi.org/10.3390/rs6065279>
- Svoray, T., & Shoshany, M. (2003). Herbaceous biomass retrieval in habitats of complex composition: A model merging SAR images with unmixed landsat TM data. *Ieee Transactions on Geoscience and Remote Sensing*, 41(7), 1592-1601. doi:<https://doi.org/10.1109/Tgrs.2003.813351>
- Swain, P. H., Robertson, T. V., & Wacker, A. G. (1971). Comparison of the Divergence and B-Distance in Feature Selection. *LARS Information Note 020871*.
- Sylla, D., Minghelli-Roman, A., Blanc, P., Mangin, A., & d'Andon, O. H. F. (2014). Fusion of Multispectral Images by Extension of the Pan-Sharpening ARSIS Method. *IEEE Journal of Selected Topics in Applied Earth Observations and Remote Sensing*, 7(5), 1781-1791. doi:10.1109/JSTARS.2013.2271911
- Taha, L. G. E.-d., & Elbeih, S. F. (2010). Investigation of fusion of SAR and Landsat data for shoreline super resolution mapping: the northeastern Mediterranean Sea coast in Egypt. *Applied Geomatics*, 2(4), 177-186. doi:<https://doi.org/10.1007/s12518-010-0033-x>
- Talab-Ou-Ali, H., Niculescu, S., Sellin, V., & Bougault, C. (2017). Contribution of the new satellites (Sentinel-1, Sentinel-2 and SPOT-6) to the coastal vegetation monitoring in the Pays de Brest (France). Paper presented at the SPIE Remote Sensing.
- Tucker, C. J. (1979). Red and Photographic Infrared Linear Combinations for Monitoring Vegetation. *Remote Sensing of Environment*, 8(2), 127-150. doi:[https://doi.org/10.1016/0034-4257\(79\)90013-0](https://doi.org/10.1016/0034-4257(79)90013-0)
- Turner, D. P., Cohen, W. B., Kennedy, R. E., Fassnacht, K. S., & Briggs, J. M. (1999). Relationships between leaf area index and Landsat TM spectral vegetation indices across three temperate zone sites. *Remote Sensing of Environment*, 70(1), 52-68. doi:Doi 10.1016/S0034-4257(99)00057-7
- Vaglio Laurin, G., Liesenberg, V., Chen, Q., Guerriero, L., Del Frate, F., Bartolini, A., Coomes, D., Wilebore, B., Lindsell, J., & Valentini, R. (2013). Optical and SAR sensor synergies for forest and land cover mapping in a tropical site in West Africa. *International Journal of Applied Earth Observation and Geoinformation*, 21, 7-16. doi:<https://doi.org/10.1016/j.jag.2012.08.002>
- Veloso, A., Mermoz, S., Bouvet, A., Le Toan, T., Planells, M., Dejoux, J.-F., & Ceschia, E. (2017). Understanding the temporal behavior of crops using Sentinel-1 and Sentinel-2-like data for agricultural applications. *Remote Sensing of Environment*, 199, 415-426. doi:<https://doi.org/10.1016/j.rse.2017.07.015>
- Villa, P., Stroppiana, D., Fontanelli, G., Azar, R., & Brivio, P. (2015). In-Season Mapping of Crop Type with Optical and X-Band SAR Data: A Classification Tree Approach Using Synoptic Seasonal Features. *Remote Sensing*, 7(10), 12859. doi:<https://doi.org/10.3390/rs71012859>
- Wang, Q., Adiku, S., Tenhunen, J., & Granier, A. (2005). On the relationship of NDVI with leaf area index in a deciduous forest site. *Remote Sensing of Environment*, 94(2), 244-255. doi:10.1016/j.rse.2004.10.006
- Wang, Q. M., Blackburn, G. A., Onojeghuo, A. O., Dash, J., Zhou, L. Q., Zhang, Y. H., & Atkinson, P. M. (2017). Fusion of Landsat 8 OLI and Sentinel-2 MSI Data. *Ieee Transactions on Geoscience and Remote Sensing*, 55(7), 3885-3899. doi:<https://doi.org/10.1109/Tgrs.2017.2683444>
- Waske, B., & Benediktsson, J. A. (2007). Fusion of Support Vector Machines for Classification of Multisensor Data. *Ieee Transactions on Geoscience and Remote Sensing*, 45(12), 3858-3866. doi:<https://doi.org/10.1109/TGRS.2007.898446>
- Waske, B., & van der Linden, S. (2008). Classifying Multilevel Imagery From SAR and Optical Sensors by Decision Fusion. *Ieee Transactions on Geoscience and Remote Sensing*, 46(5), 1457-1466. doi:<https://doi.org/10.1109/TGRS.2008.916089>

- Wei, M., & Sandwell, D. T. (2010). Decorrelation of L-Band and C-Band Interferometry Over Vegetated Areas in California. *IEEE Transactions on Geoscience and Remote Sensing*, 48(7), 2942-2952. doi:<https://doi.org/10.1109/TGRS.2010.2043442>
- Woodhouse, I. H. (2006). *Introduction to Microwave Remote Sensing*: CRC Press, Boca Raton, FL.
- Xu, H. (2006). Modification of normalised difference water index (NDWI) to enhance open water features in remotely sensed imagery. *International Journal of Remote Sensing*, 27(14), 3025-3033. doi:<https://doi.org/10.1080/01431160600589179>
- Xu, H. (2008). A new index for delineating built-up land features in satellite imagery. *International Journal of Remote Sensing*, 29(14), 4269-4276. doi:<https://doi.org/10.1080/01431160802039957>
- Xue, J., Leung, Y., & Fung, T. (2017). A Bayesian Data Fusion Approach to Spatio-Temporal Fusion of Remotely Sensed Images. *Remote Sensing*, 9(12). doi:<https://doi.org/10.3390/rs9121310>
- Yesou, H., Pottier, E., Mercier, G., Grizonnet, M., Haouet, S., Giros, A., Faivre, R., Huber, C., & Michel, J. (2016, 10-15 July 2016). *Synergy of Sentinel-1 and Sentinel-2 imagery for wetland monitoring information extraction from continuous flow of sentinel images applied to water bodies and vegetation mapping and monitoring*. Paper presented at the 2016 IEEE International Geoscience and Remote Sensing Symposium (IGARSS).
- Zha, Y., Gao, J., & Ni, S. (2003). Use of normalized difference built-up index in automatically mapping urban areas from TM imagery. *International Journal of Remote Sensing*, 24(3), 583-594. doi:<https://doi.org/10.1080/01431160304987>
- Zhang, J. (2010). Multi-source remote sensing data fusion: status and trends. *International Journal of Image and Data Fusion*, 1(1), 5-24. doi:<https://doi.org/10.1080/19479830903561035>
- Zheng, Y., Zhang, M., Zhang, X., Zeng, H. W., & Wu, B. F. (2016). Mapping Winter Wheat Biomass and Yield Using Time Series Data Blended from PROBA-V 100-and 300-m S1 Products. *Remote Sensing*, 8(10). doi:<https://doi.org/10.3390/rs8100824>
- Zhou, Y., Yang, G., Wang, S. X., Wang, L. T., Wang, F. T., & Liu, X. F. (2014). A new index for mapping built-up and bare land areas from Landsat-8 OLI data. *Remote Sensing Letters*, 5(10), 862-871. doi:<https://doi.org/10.1080/2150704x.2014.973996>
- Zhu, X., Chen, J., Gao, F., Chen, X., & Masek, J. G. (2010). An enhanced spatial and temporal adaptive reflectance fusion model for complex heterogeneous regions. *Remote Sensing of Environment*, 114(11), 2610-2623. doi:<https://doi.org/10.1016/j.rse.2010.05.032>
- Zhu, Z., Wang, S., & Woodcock, C. E. (2015). Improvement and expansion of the Fmask algorithm: cloud, cloud shadow, and snow detection for Landsats 4–7, 8, and Sentinel 2 images. *Remote Sensing of Environment*, 159, 269-277. doi:<https://doi.org/10.1016/j.rse.2014.12.014>